Thermoelectric Properties of Higher Manganese Silicides

by

Dao Y Nhi Truong

A thesis
presented to the University of Waterloo
in fulfillment of the
thesis requirement for the degree of
Doctor of Philosophy
in
Chemistry (Nanotechnology)

Waterloo, Ontario, Canada, 2015

© Dao Y Nhi Truong, 2015

AUTHOR'S DECLARATION

I hereby declare that I am the sole author of this thesis. This is a true copy of the thesis, including any required final revisions, as accepted by my examiners.

I understand that my thesis may be made electronically available to the public.

Abstract

This work aims to cover a variety of aspects relating to the Higher Manganese Silicide (HMS) system, e.g. composites, substitutions, synthesis methods, and structural evolutions.

The composites made of HMS-based compounds and nano-inclusions have been prepared via two different procedures, i.e. (i) solid state reaction, manually mixing, and hot pressing, or (ii) soft ball milling and reactive spark plasma sintering. The later approach has proved its effectiveness in preparing the multi-walled carbon nanotube (MWCNT)/HMS-based material composites mainly containing the HMS phases with a homogeneous distribution of MWCNTs. It was demonstrated that a fine distribution of the nano-inclusions played a crucial role in reducing thermal conductivity through enhancing phonon scattering in HMS-based materials, resulting in an improvement by about 20% for the maximum efficiency for the MWCNT/HMS-based material composite with 1.0 wt.-% MWCNTs.

The substitution of molybdenum, tungsten, or silver at the Mn sites, and of germanium or aluminium at the Si sites has been studied for the HMS-based materials. The best thermoelectric efficiency among different Ge contents was achieved for the phase mixture of the non-stoichiometric composition $MnSi_{1.75}Ge_{0.02}$, which was then chosen to be the base material for further substitutions. No crucial modification of the electrical properties of the base material was observed, but large decreases of lattice thermal conductivity were achieved because of enhanced phonon scattering, with the highest reduction up to 25% for molybdenum substitution. The maximum figure of merit, *ZT*, value was approximately 0.40 for the material with 2 at.-% molybdenum substitution at the Mn sites.

The maximum *ZT* values ranging from 0.31 to 0.42 have been achieved for various compositions prepared by mechanical alloying, mechanical milling and heat treating in conventional furnace, as well as by solid state reaction, which could possibly be improved by completely eliminating the side products. Subsequently, a simple and effective process was

used to synthesize undoped HMS, involving ball milling in *n*-hexane under soft conditions to obtain homogeneous mixtures of constituting elements, and subsequent spark plasma sintering for a direct solid state reaction. The obtained fine particles after the milling process in *n*-hexane helped to improve the reaction rate later on, resulting in pure HMS materials. As a consequence, the maximum thermoelectric figure of merit obtained was 0.55 at 850 K, a high value for undoped HMS. Moreover, single crystals of HMS have been prepared using chemical vapor transport with very low yield, but their poor qualities resulted in low resolution in single crystal XRD.

HMS-based materials including the ones with different Si/Mn atomic ratios and various dopants, e.g. Ge, Al, Cr, and Mo, have been prepared for the investigation of structural evolution upon heating up from room temperature to high temperature. The average structural formula at room temperature and its temperature dependence were strongly impacted by the phase compositions of the starting materials as well as the nature of dopants. Physical property measurements on the $MnSi_{1.75}$ compound revealed that a correlation between the thermoelectric properties and the average structural formula of bulk HMS-based materials could be expected.

Acknowledgements

First, I would like to show my gratitude to my supervisors, Franck Gascoin and Holger Kleinke, for their guidance throughout my PhD journey. I am deeply grateful to Franck for all the opportunities and travels that he gave me. His supports and considerations helped me to deal with all the troubles that I encountered during the last four years. I am heartily thankful to Holger for his instructions and invaluable advices throughout the time I am in his research group. All his patient explanations and discussions enabled me to develop an understanding of the subject. I truly appreciate my supervisors for their times and attempts to correct all my manuscripts and this thesis. All the drinks that we had together were really enjoyable and memorable to me.

Second, I would like to thank all the helpful comments my advisory committees, Prof. Linda Nazar and Prof Richard Oakley, gave me during my seminar and annual meetings, which helped me to progress my works. I am very grateful for being able to have Dr. Yurij Mozharivskyj, Dr. Dmitriy Soldatov, and Dr. James R. Salvador as my juries.

Third, I would like to thank the IDS-FunMat Consortium for holding this cotutelle doctoral program. I am so thankful for the chance to meet and hang out with all the IDS-FunMaters, especially the students in Caen and Waterloo. I truly believe that all of us will be very successful in our future career.

For Crismat, I would like to thank for all the technical supports provided by the lab staffs, Stéphanie, Jéjé, Fanfan, Dimitri, Marie, Sophie, Laurence, Xavier, Muriel, Guillaume, Emmanuel, Eric, Karim, and Fabien (Veillon). I was so fortune to be in the same office with David and Quentin for my first year, and I am deeply grateful for all their helps. I really appreciate all the assistances and friendship that Raghu gave me for my first year in Caen, and I truly enjoyed all the times spending with Robinou during my third year. I would like to say thank you so much for all the people I have met thorough my time in Caen, Clément,

Thibault, Fabien (Lainé), Antoine, Alex, Mateja, Suresh, Etienne, Kamil, Pablo, Patrick, Marion, Aline, Yohann, and many others.

For Waterloo, I would like to thank all the former and current group members for all their assistances. I specially thank Nader for all his helps since the first day I came to Canada. I deeply appreciate all the scientific and technical supports from Katja, Jalil, Raj, Quansheng, Susan, and Natasha, and I am really thankful for the chance to colaborate with XY. I wish Rafay, Mohamed, and Chris all the bests for whatever they will be doing, and I believe that all of you will finish your studies successfully, Mathew, Parisa, Yixuan, Bin, and Nagaraj.

Next, I would like to thank my beloved family and friends from Vietnam, Caen, and Waterloo for their invaluable supports during the last four years. Although they could not be always beside me, their encouragements are the most important things to help me overcome all the difficulties. I am indebted to all the nice people whom I have met for their presences and assistances during my daily life and my study.

Last but not least, I would like to thank the Region Basse Normandie and the Natural Sciences and Engineering Research Council of Canada for the financial supports. I could not achieve my PhD degree without these aids.

For my dad …

Table of Contents

List of Figures

List of Tables

Chapter 1

Backgrounds on Thermoelectrics

Abstract

In this chapter, an introduction to thermoelectric phenomena will be given in section 1.1, which includes the three thermoelectric effects, the formula to evaluate the thermoelectric efficiency, and the thermoelectric modules. Subsequently, the optimization of the thermoelectric performance will be discussed in section 1.2 for the related parameters. Finally, a brief review of current state-of-the-art materials will be presented in section 1.3.

1.1 Thermoelectric phenomena

1.1.1 Thermoelectric effects

It was in 1821 when the Estonian-German physicist Thomas Johann Seebeck noticed the deflection of a compass needle, which was placed close to a circuit made from two dissimilar conductors when the junctions were kept at different temperatures.[1] Seebeck mistook the magnetic interaction for the driving force, and even made an effort to relate the earth's magnetic field to the temperature gradient between the equator and the poles. Later, Hans Christian Oersted, who has previously proved that an electrical current generates a magnetic field encircling it, identified this observation as a thermoelectric effect, which was named after Seebeck and became the basics of all researches in the areas (Figure 1.1).[2] The magnitude of the deflection, or the induced voltage (ΔV), was proportional to the temperature difference between the two junctions (ΔT), which was defined as Seebeck coefficient or thermopower (S) (Eq. 1.1).

$$S = \frac{\Delta V}{\Delta T} \qquad \text{(Eq. 1.1)}$$

Thirteen years later, the French physicist Jean Charles Athanase Peltier discovered the temperature at the junction of two dissimilar materials changed when an electrical current passed through (Figure 1.1).[3] Peltier, then, interpreted that the Joule's laws, which stated that

heat is generate by a current flowing through a conductor, were invalid for a weak current. The true explanations were given by Lenz in 1838, concluded that heat is either absorbed or generated at the junction depending on the direction of the current flow. The Peltier coefficient (π) was defined as the ratio between the heat carried by charges (Q) and the current across the junction (I) (Eq. 1.2).

$$\pi = \frac{Q}{I} \qquad \text{(Eq. 1.2)}$$

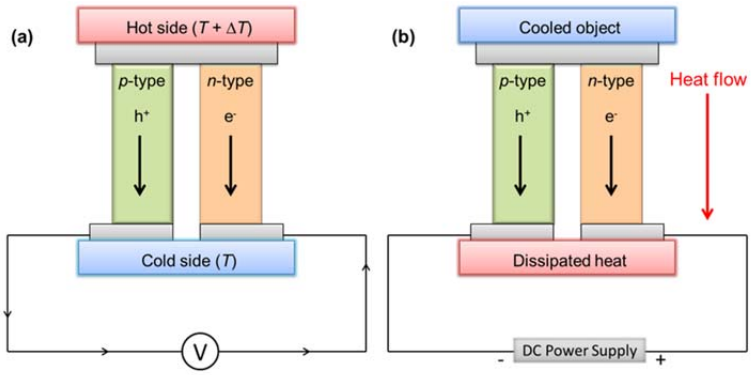

Figure 1.1 (a) Seebeck effect (Power generation mode) – When the junctions are held at different temperatures, a voltage difference is generated; (b) Peltier effect (Refrigeration mode) – When an electrical current is passed through the junction, heat is transported by the charge carriers.

In 1851, William Thomson (later Lord Kelvin) described the relationship between Seebeck and Peltier effects in the Kelvin relation (Eq. 1.3). This thermodynamic relation led him to predict the existence of the third thermoelectric effect, which was named as Thomson effect.[4] He observed that heat is either absorbed or produced when an electrical current passes through any homogeneous conductor placed in a temperature gradient (Figure 1.2).

$$S = \frac{\pi}{T} \qquad \text{(Eq. 1.3)}$$

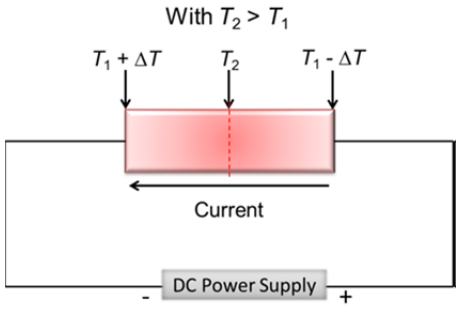

Figure 1.2 Thomson effect – When an electrical current is passed through a *p*-type conductor placed in a temperature gradient, the positive charge carriers flowing in the same (opposite) directions to the thermal gradient from T_2 to T_1 will evolve (absorb) heat to reduce (increase) their potential energy.

1.1.2 Thermoelectric efficiency

The performance of thermoelectric devices strongly depends on the efficiency of the materials of which they are made. This efficiency is evaluated by the thermoelectric figure of merit (Z), which expresses the combination between Seebeck coefficient (S), electrical resistivity (ρ), and thermal conductivity (κ) (Eq. 1.4), while the conventional dimensionless figure of merit (ZT) is used for the comparison between different thermoelectric materials (Eq. 1.5), where T is the absolute temperature.[5]

$$Z = \frac{S^2}{\rho\kappa} \qquad \text{(Eq. 1.4)}$$

$$ZT = \frac{S^2 T}{\rho\kappa} \qquad \text{(Eq. 1.5)}$$

The efficiency of thermoelectric devices is calculated from the temperature difference between the hot and cold side, and the figure of merit of materials, which is limited by the

Carnot efficiency (Eq. 1.6), where T_H and T_C are the hot and cold side temperature, respectively, and $\overline{T}$, equal to $(T_H + T_C)/2$, is the mean temperature (Figure 1.3).

$$\eta = \frac{T_H - T_C}{T_H} \times \frac{\sqrt{1 + Z_{p,n}\overline{T}} - 1}{\sqrt{1 + Z_{p,n}\overline{T}} + \frac{T_C}{T_H}} \qquad \text{(Eq. 1.6)}$$

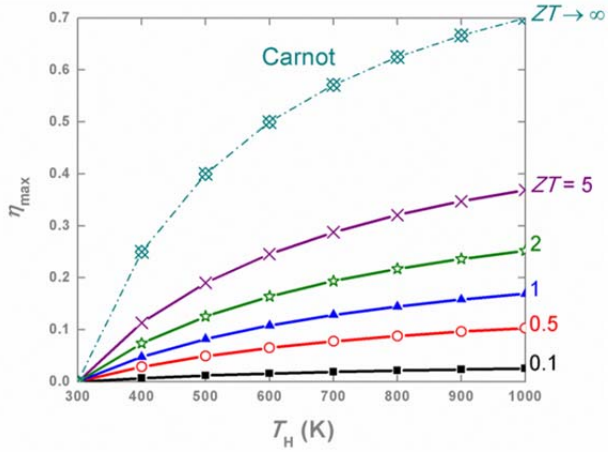

Figure 1.3 The efficiency of thermoelectric devices as a function of hot-side temperature for different materials with the cold side is kept at 300 K.

1.1.3 Thermoelectric modules

The thermoelectric devices contain thermoelectric modules, comprised of many thermoelectric couples of *p*-type and *n*-type materials, connected electrically in series and thermally in parallel (Figure 1.4). The compact blocks of materials are cut into equal rectangular bars, glued to appropriate electrodes at the top and bottom ends. The electrodes are joined to two substrates made of electrically insulating and thermally conductive materials, i.e. Al_2O_3. During operational processes, one of the substrates will be touching the hot source, while the other one is in contact with the cold source. The induced current is led out through an external electrical connection.

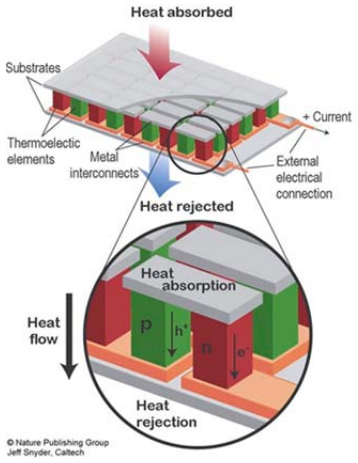

Figure 1.4 Schematic illustration of a thermoelectric module showing the heat and charge flow directions;[6] reprinted with permission from Macmillan Publishers Ltd: [Nature Materials] (http://dx.doi.org/10.1038/nmat2090), copyright (2008).

An application of thermoelectric devices may be in the automotive industry. The internal combustion engines of gasoline-powered vehicles have low efficiency with only about 25-30% of available energy being actually used to move the car or run the accessories, 40% of the energy is released as waste heat, and the rest is lost to engine friction and air conditioning process. Many research groups have been working on thermoelectric-based waste heat recovery to utilize the available heat from the exhaust gas for power generation. The world's largest auto companies, such as BMW, Ford, and GM, have been conducting the tests of thermoelectric devices on real cars.

1.2 *ZT* optimization

According to (Eq. 1.5), a good thermoelectric material should possess high Seebeck coefficient, low electrical resistivity, and low thermal conductivity. At a specific temperature gradient, the higher the Seebeck coefficient is, the higher the voltage is produced. Moreover,

the low electrical resistivity helps to reduce the heat losses by Joule heating, and the low thermal conductivity will keep the thermal gradient alive.

The Seebeck coefficient is negative if the majority charge carriers are electrons, and it is positive if the majority charge carriers are holes. For materials with parabolic band and energy-independent scattering approximation, the Seebeck coefficient is proportional to the effective mass of the charge carriers, m^*, and inversely proportional to the carrier concentration, n.[7] The relation is given in (Eq. 1.7), where k_B is the Boltzmann constant, T is the absolute temperature, e is the elementary charge, and h is the Planck constant.

$$S = \frac{\pi^2 k_B^2 T}{3e} \times \frac{8m^*}{h^2} \times \left(\frac{\pi}{3n}\right)^{2/3} \quad \text{(Eq. 1.7)}$$

It is also noticeable that an important factor does not explicitly appear in this equation, which is the carrier mobility (μ). The interdependence between the carrier mobility and the effective mass is shown in (Eq. 1.8), where τ is the relaxation time or the average duration between subsequent collisions of charge carriers. Therefore, the materials with low carrier concentration and high effective mass or low carrier mobility, such as insulators or wide bandgap semiconductors, will possess high Seebeck coefficient.

$$\mu = \frac{e\tau}{m^*} \quad \text{(Eq. 1.8)}$$

Electrical resistivity, ρ, is an intrinsic property of a material, which measures its ability to oppose the flow of the electrical current. Consequently, the electrical resistivity is defined as the ratio of the electric field inside a material (E) to the current density (J) that it generated (Eq. 1.9).

$$\rho = \frac{E}{J} \quad \text{(Eq. 1.9)}$$

Since $J = ne\mu E$, the relation between the carrier mobility (μ), carrier concentration (n), and the electrical resistivity can be expressed as in (Eq. 1.10). As a consequence, the higher the carrier mobility and carrier concentration of a material are, such as metals and

semimetals, the lower its electrical resistivity will be. Here, a conflict between high Seebeck coefficient and low electrical resistivity is raised, which will need a compromise in the carrier concentration and carrier mobility to achieve an optimum thermoelectric performance. The optimum carrier concentration, which is usually achievable through doping with donor or accepter dopants, is usually in the range from 10^{19} to 10^{20} cm^{-3} (Figure 1.5), which is typical for heavily doped semiconductors.

$$\rho = \frac{1}{ne\mu} \qquad \text{(Eq. 1.10)}$$

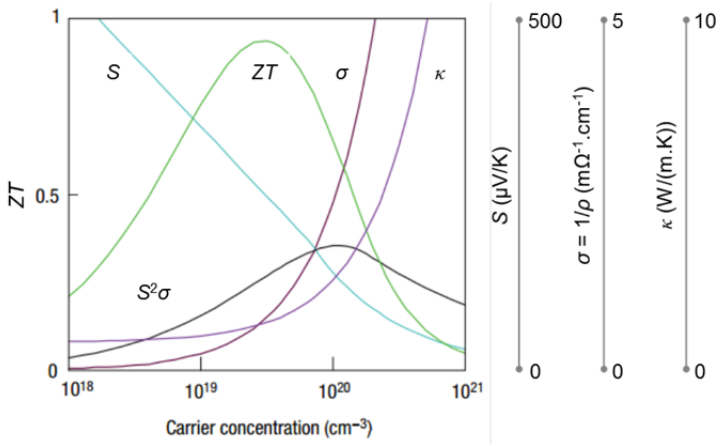

Figure 1.5 Optimizing figure of merit of Bi_2Te_3 through tuning carrier concentration; the maximum thermoelectric performance is attained with a carrier concentration in the range from 10^{19} to 10^{21} cm^{-3}, which is typical for heavily doped semiconductors;[6] reprinted with permission from Macmillan Publishers Ltd: [Nature Materials] (http://dx.doi.org/10.1038/nmat2090), copyright (2008).

According to Mott's equation, the Seebeck coefficient is proportional to the derivative of the logarithmic electrical conductivity, $\sigma = \rho^{-1}$, with respect to the energy, E, at the Fermi level (Eq. 1.11).[8]

$$S = \frac{\pi^2}{3} \cdot \frac{k_B^2 T}{e} \cdot \left. \frac{d \ln \sigma(E)}{dE} \right|_{E=E_F} \quad \text{(Eq. 1.11)}$$

Since the electrical conductivity directly relates to the density of states, *DOS*, (Eq. 1.12), the Seebeck coefficient can be deduced from the first derivative of the *DOS*, with respect to the energy, *E*, at the Fermi level (Eq. 1.13).[9]

$$\sigma \propto DOS(E)\big|_{E=E_F} \quad \text{(Eq. 1.12)}$$

$$S \propto \frac{1}{DOS(E)} \cdot \left. \frac{dDOS(E)}{dE} \right|_{E=E_F} \quad \text{(Eq. 1.13)}$$

As a consequence, band engineering through alloying is an important strategy to improve the *ZT*, including tuning the bandgap, adjusting the position of the Fermi level, or distorting the *DOS* close to the Fermi level by resonant impurities.[10] Generally, a flat band, or high effective mass will result in a high Seebeck coefficient, but low carrier mobility and thus high electrical resistivity.

Thermal conductivity is the property of a material, which concerns its ability to conduct heat. When a material is subjected to a temperature gradient, there are three principal mechanisms underlying the heat transport. Therefore, the total thermal conductivity is the sum of three terms (Eq. 1.14), where κ_e is the electronic thermal conductivity due to the charge transport, κ_l is the lattice thermal conductivity due to atom vibrations, and κ_{bp} is the bipolar thermal conductivity due to the formation and recombination of electron-hole pairs.

$$\kappa = \kappa_e + \kappa_l + \kappa_{bp} \quad \text{(Eq. 1.14)}$$

The electronic thermal conductivity relates to the electrical resistivity via Wiedemann-Franz law (Eq. 1.15), where *L* is the proportional constant, named Lorenz number.

$$\kappa_e = \frac{LT}{\rho} \quad \text{(Eq. 1.15)}$$

Using Fermi-Dirac statistics for a classical free electron model, Sommerfeld calculated the theoretical Lorenz number (Eq. 1.16). Experiments have shown that L is not universal for all the materials, but depends on material types, temperatures, and certain system parameters, such as doping concentrations, dimensionality, and Fermi level.[11] For doped semiconductors, L usually ranges from 1.5×10^{-8} $V^2 \cdot K^{-2}$ to 2.5×10^{-8} $V^2 \cdot K^{-2}$.

$$L = \frac{\pi^2}{3}\left(\frac{k_B}{e}\right)^2 = 2.44 \times 10^{-8} V^2 \cdot K^{-2} \qquad \text{(Eq. 1.16)}$$

The lattice thermal conductivity arises from the lattice vibration; therefore, its value strongly depends on the vibration mode. Atomic vibrations exist in all crystalline systems at above 0 K. The concept of phonon is considered as the quantized energy of lattice vibrations, related to both vibration frequency and temperature. As the temperature is raised, the amplitude of atomic agitations is increased, which means the number of phonons in the systems increases. For a simple crystalline solid, the lattice thermal conductivity is based on Debye's equation (Eq. 1.17), treating lattice vibrations as a phonon gas, where C_V is the volume heat capacity, v is the average phonon group velocity, and λ is the phonon mean free path.

$$\kappa_l = \frac{1}{3} C_V v \lambda \qquad \text{(Eq. 1.17)}$$

There are several strategies to reduce lattice thermal conductivity for improving thermoelectric performance, such as using materials with complex crystal structures, forming solid solutions to create mass fluctuation scattering, introducing impurities or large and heavy atoms into the material matrix (according to the concept of PGEC, i.e. "a phonon glass and an electron single crystal"),[12] such as Sn, Sb, Te, Tl, Pb, or Bi, cooperating rattling atoms or ions into caged structures, creating structural defects, or reducing grain sizes to increase grain boundaries. Moreover, the PLEC concept, which stands for "a phonon liquid and an electron single crystal", describes a strategy to lower the lattice thermal conductivity by that of a glass through both reducing phonon mean free path and eliminate completely some vibrational modes.[13] The only families of materials found to follow this concept are the

super-ionic copper chalcogenides $Cu_{2-x}Q$, where Q is S, Se, or Te, and possibly its higher variants such as $BaCu_{6-x}STe_6$ and $BaCu_{6-x}SeTe_6$.[14] The Se atoms in $Cu_{2-x}Se$ form rigid crystalline structure, while the copper ions are highly disordered with liquid-like mobility, which results in an intrinsically low lattice thermal conductivity.

The bipolar thermal conductivity exists in the temperature range of intrinsic excitations, in which both electrons and holes contribute to the heat conduction. For thermoelectric materials in operation, this conduction happens because a larger number of electron-hole pairs are generated at the hot side more than the cold side when the material is subjected to a temperature gradient. Additionally, the recombination happening at the cold side releases a certain amount of energy, corresponding to the materials' bandgap, which contributes to the total thermal conduction. The bipolar thermal conductivity is calculated according to (Eq. 1.18), where *e* and *h* indicate the contribution of electrons and holes, respectively.

$$\kappa_{bp} = \left(\frac{k_B}{e}\right)^2 \frac{1}{\rho_e + \rho_h}\left(S_e - S_h\right)^2 T \qquad \text{(Eq. 1.18)}$$

1.3 State-of-the-art materials

Bismuth telluride (Bi_2Te_3) and its alloys are widely used to construct thermoelectric modules for applications at near room temperature, i.e. from 300 K to 400 K. Since H. Julian Goldsmid and his coworker demonstrated the first cooling experiments below zero degrees Celsius using Bi_2Te_3 and bismuth for the thermocouples in 1954,[15] Bi_2Te_3-based compounds had always been the research focus of various groups in the thermoelectric society, resulting in more than 1500 scientific publications in 2014. Bismuth telluride is commonly alloyed with either bismuth selenide (Bi_2Se_3) or antimony telluride (Sb_2Te_3) with identical structure type to improve its thermoelectric performance.[16,17] An important advantage of these compounds is the existence of both *n*-type and *p*-type materials whose thermoelectric performances are substantially high for practical applications.

For intermediate temperature applications, i.e. from 400 K to 800, the prospective thermoelectric materials with the maximum *ZT* exceeding 1 include the lead telluride (PbTe) compound and its related materials, the Tellurium-Antimony-Germanium-Silver system (TAGS), the silver antimony telluride $AgSbTe_2$, the LAST (Lead-Antimony-Silver-Telluride), LASTT (Lead-Antimony-Silver-Tellurium-Tin), and SALT (Sodium-Antimony-Lead-Tellurium) materials, the skutterudites, β-Zn_4Sb_3, and the Thallium-containing compounds. Above 800 K, the silicon germanium ($Si_{1-x}Ge_x$) alloys, the clathrates, the half-Heusler compounds, $Yb_{14}MnSb_{11}$, the super-ionic compounds $Cu_{2-x}Q$, where Q is S, Se, or Te, Mo_3Sb_7, and lanthanum telluride $La_{3-x}Te_4$, all have been extensively investigated.

For future materials, the BiCuSeO oxyselenides, the tetrahedrite ($Cu_{12-x}M_xSb_4S_{13}$) and tennantite ($Cu_{12-x}M_xAs_4S_{13}$) systems, where M is a transition metal, and the silicides, have recently attract a lot of attentions from material researchers. Here, a summary of the current materials with high thermoelectric performance is given in Table 1.1.

Table 1.1 A summary of currently high performance thermoelectric materials.

Material	Type	$(ZT)_{max}$ at T	Reference
$Bi_{0.48}Sb_{1.52}Te_3$ and $Bi_{0.6}Sb_{1.4}Te_3$	*p*	1.5 at 390 K	[18]
Flower-like nanosheets Bi_2Te_3	*n*	1.2 at 423 K	[19]
$AgSbSe_{0.02}Te_{1.98}$	*p*	1.4 at 565 K	[20]
$Ag_{1-x}Pb_{18}SbTe_{20}$ (LAST-18)	*n*	2.1 at 800 K	[21]
$Ag_{0.5}Pb_6Sn_2Sb_{0.2}Te_{10}$ (LASTT)	*p*	1.5 at 627 K	[22]
$Na_{0.95}Pb_{20}SbTe_{22}$ (SALT)	*p*	1.7 at 650 K	[23]
$CeFe_{4-x}Co_xSb_{12}$	*p*	1.4 at 873 K	[24]
$Ba_{0.08}La_{0.05}Yb_{0.04}Co_4Sb_{12}$	*n*	1.7 at 850 K	[25]
β-Zn_4Sb_3	*p*	1.3 at 670 K	[26]
$Tl_9Bi_{0.98}Te_6$	*p*	1.1 at 500 K	[27]
$Tl_{8.10}Pb_{1.90}Te_6$	*p*	1.5 at 680 K	[28]
P-doped $Si_{0.8}Ge_{0.2}$	*n*	1.0 at 900 K	[29]

B-doped $Si_{0.8}Ge_{0.2}$	*p*	0.6 at 900 K	[29]
$PbTe_{0.9988}I_{0.0012}$	*n*	1.4 at 750 K	[30]
$Na_xPb_{1-x}Te$ containing 9.0×10^{19} holes/cm^3	*p*	1.4 at 750 K	[31]
TAGS-80	*p*	1.8 at 773 K	[32]
TAGS-85 + 1% and 2% Dy for Ge	*p*	> 1.5 at 730 K	[33]
$Yb_{14}MnSb_{11}$	*p*	> 1.0 at 1200K	[34]
α-Cu_2Se	*p*	2.3 at 400 K	[35]
β-Cu_2Se	*p*	1.5 at 1000 K	[13]
$Ni_{0.06}Mo_3Sb_{5.4}Te_{1.6}$	*p*	0.9 at 1023 K	[36]
$La_3Te_{3.35}Sb_{0.65}$	*n*	1.1 at 1200 K	[37]
In_4Se_{3-x}	*n*	1.48 at 705 K	[38]
$Ba_8Ga_{16}Ge_{30}$	*n*	1.35 at 900 K	[39]
$Ti_{0.5}(Zr_{0.5}Hf_{0.5})_{0.5}NiSn_{0.998}Sb_{0.002}$	*n*	1.5 at 700 K	[40]
Textured $Bi_{0.875}Ba_{0.125}CuSeO$	*p*	1.4 at 923 K	[41]
$(Cu_{9.7}Zn_{1.9}Fe_{0.4}As_4S_{13})_{0.5}(Cu_{12}Sb_4S_3)_{0.5}$	*p*	1 at 723 K	[42]
$Mg_2Si_{0.53}Sn_{0.4}Ge_{0.05}Bi_{0.02}$	*n*	1.4 at 800 K	[43]
$MnSi_{1.84}$	*p*	0.83 at 818 K	[44]
$Re_{0.98}Mo_{0.02}Si_{1.75}$	*n*	0.8 at 1073 K	[45]
$(Ru_{0.96}Rh_{0.04})_2Si_3$	*n*	0.8 at 1073 K	[46]
$Ca_{2.97}Na_{0.03}AlSb_3/Ca_{2.94}Na_{0.06}AlSb_3$	*p*	0.8 at 1050 K	[47]
$Pb_{0.975}Na_{0.025}S$ + 3.0 at.-% SrS	*p*	1.22 at 923 K	[48]
SnSe (measured along the *b*-axis)	*p*	2.6 at 923 K	[49]
$AgSb_{0.99}Sn_{0.01}Se_2$	*p*	1.21 at 660 K	[50]
PbTe-SrTe (4 mol.%) doped with 2 mol.% Na	*p*	2.2 at 915 K	[51]

Chapter 2

Higher Manganese Silicides

Abstract

In this chapter, an overview on Mn-Si binary phase diagram will be introduced in section 2.1. Afterward, the crystal structure and properties of MnSi will be briefly given in section 2.2 because this phase is commonly formed during the synthesis of the incongruent melting Higher Manganese Silicides. Subsequently, a summary on Higher Manganese Silicides will be focused in section 2.3 aiming to cover most of the related aspects i.e. crystalline and electronic structure, phase transformation, single crystal growth, synthesis problems, thermoelectric properties, and thermoelectric applications. Finally, a short conclusion will be given in section 2.4 regarding the remaining challenges for this system.

2.1 Mn-Si binary phase diagram

The Mn-Si binary system has been extensively studied,[52,53] and it exhibits different compounds with various Si contents (Figure 2.1).

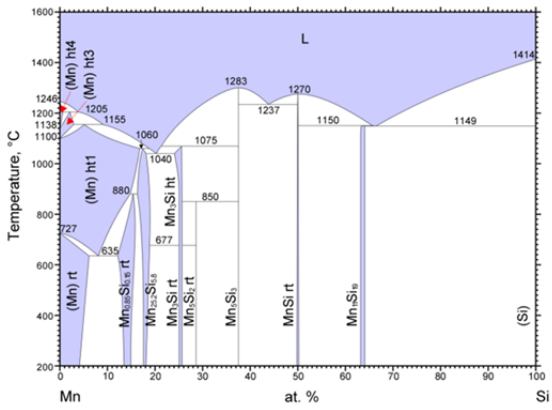

Figure 2.1 Mn-Si binary phase diagram.[53]

If the Si/Mn atomic ratio in manganese silicides is less than 1, the Mn-Mn bonds will possibly be formed, resulting in metallic behavior, which is unfavorable for thermoelectric applications. Therefore, only manganese monosilicide (MnSi) compound and the Si-rich ones are considered for thermoelectric materials.

2.2 Manganese monosilicide (MnSi)

MnSi is a magnetic intermetallic material, crystallizing in B20 structure with the cubic $P2_13$ space group,[54] considered as a distorted NaCl structure, where the atoms are displaced from their original positions in the rocksalt structure along the [111] direction (Figure 2.2).[55] Each unit cell contains four Mn and four Si atoms, where Mn is coordinated to one adjacent Si neighbor along the [111] direction, three second nearest and three next closest Si neighbors.

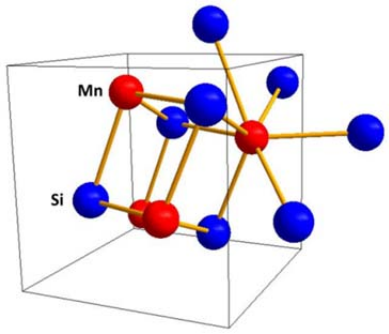

Figure 2.2 The B20 structure of MnSi.[54]

The interest in MnSi has been revived in the last few years owing to its peculiar magnetic properties.[56–58] Several theoretical and experimental studies have focused on epitaxial growth of MnSi on Si substrate for future spin injection into silicon.[59–61] The magnetic properties of some MnSi-based solid solutions, such as $Co_{1-x}Mn_xSi$ and $Fe_{1-x}Mn_xSi$, have been investigated since 1972.[62]

As it can be seen from its calculated DOS, MnSi exhibits a metallic behavior with a narrow gap of approximately 0.2 eV above the Fermi level and a high hole concentration in the order of 10^{22} cm^{-3}, leading to a good electrical and thermal conductor.[59] Sakurai *et al*.[63] have performed a measurement of the thermoelectric power of MnSi from liquid helium temperature to room temperature. The electrical resistivity and Seebeck coefficient of MnSi increased with increasing temperature, confirming its metallic characteristic. A low resistivity of about 0.2 mΩ·cm in combination with a low thermoelectric power of approximately 40 μV/K led to a low power factor of 8×10^{-4} $W \cdot m^{-1} \cdot K^{-2}$ at room temperature. Later, it has been shown that the MnSi material synthesized by induction melting possesses a low *ZT* value of 0.039 at 450 K.[64] The large carrier concentration, low Seebeck coefficient, and high thermal conductivity all verify that MnSi is not a promising material for thermoelectric studies.

However, thermodynamic studies have indicated that the enthalpies and Gibbs energy of mixing for the Mn-Si alloys attain the minima when the composition is close to MnSi, suggesting its thermodynamic stability in the Mn-Si system.[65,66] Therefore, MnSi was commonly formed during the phase transformations between different Higher Manganese Silicides phases, affecting their transport properties.

2.3 Higher Manganese Silicides (HMS)

The compositional formula of HMS was mistakenly believed to be $MnSi_2$ in the early days. In 1968, a process of making crack-free Mn_4Si_7 with improved thermoelectric performance compared to MnSi and $MnSi_2$ was patented, which included melting the mixture, solidifying the melt, crushing the solid melt, and hot pressing the finely divided particles.[64] Since then, HMS have attracted a lot of attention from material researchers all over the world as potential candidates for thermoelectric applications.

Higher Manganese Silicides (HMS) are the only known compounds in which the Si amounts (63-64 at.-%) exceeds that of Mn. The first glimpse at the phase diagram gives an impression that HMS are the solid solutions with continuous compositions (Figure 2.1).

Actually, distinct compounds with different structural formulas exist, including Mn_7Si_{12}, $Mn_{11}Si_{19}$, $Mn_{26}Si_{45}$, $Mn_{15}Si_{26}$, $Mn_{19}Si_{33}$, $Mn_{27}Si_{47}$, $Mn_{39}Si_{68}$, and Mn_4Si_7 (Figure 2.3).

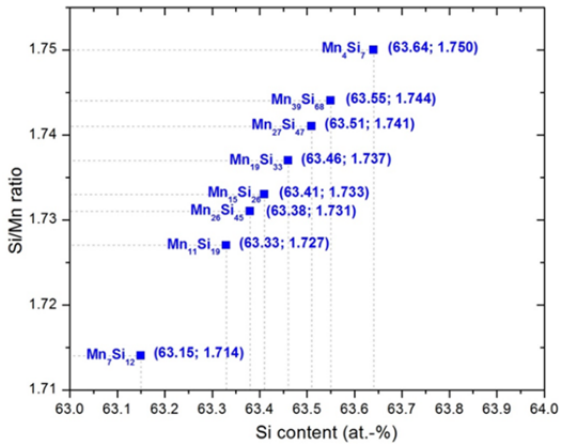

Figure 2.3 Different structural formulas of HMS with the corresponding Si/Mn ratios and Si contents (according to Inorganic Crystal Structure Database in 2012).

The four most common formulas of bulk materials are $Mn_{11}Si_{19}$, $Mn_{15}Si_{26}$, $Mn_{27}Si_{47}$, and Mn_4Si_7 (Table 2.1), for which all the atomic positions have been experimentally determined, while the others (Mn_7Si_{12}, $Mn_{19}Si_{33}$, $Mn_{39}Si_{68}$) were only obtained from nanowires or nanoribbons,[67,68] or as a microscopic domain in an inhomogeneous sample ($Mn_{26}Si_{45}$, $Mn_{19}Si_{33}$, Mn_7Si_{12}, $Mn_{39}Si_{68}$).[69,70] These commensurate phases usually coexist in an as-synthesized material, they are undistinguishable using conventional X-ray diffraction (XRD), and the conditions for separately synthesizing a particular compound have not been identified yet.

Table 2.1 The four most common structural formulas of HMS. While the Si/Mn atomic ratios in different HMS compounds are very close, the *c*-axis lengths vary over a wide range. Three and two data sets were found from the database for Mn_4Si_7 and $Mn_{15}Si_{26}$, respectively.

Formulae	Mn_4Si_7[71,72]	$Mn_{11}Si_{19}$[73]	$Mn_{15}Si_{26}$[74,75]	$Mn_{27}Si_{47}$[76]
ICSD #	20323 (97393) (183036)	43280	15339 (43059)	23789
Space group	$P\bar{4}c2$ (116)	$P\bar{4}n2$ (118)	$I\bar{4}2d$ (122)	$P\bar{4}n2$ (118)
a (Å)	5.525 (5.5259) (5.5406)	5.52	5.531 (5.525)	5.53
c (Å)	17.463 (17.5156) (17.4954)	48.2	65.311 (65.550)	117.9
d (g/cm^3)	5.19 (5.17) (5.15)	5.14	5.17 (5.16)	5.16
Z	4			
R value	0.1232 (0.029) (0.0444)	0.095	0.044 (0.118)	0.093
Comments	Single crystal XRD		Powder XRD	

The HMS compounds are potential materials to fabricate thermoelectric modules with high stability during heating cycles in various atmospheres for several reasons. First, the constituent elements of manganese and silicon are nontoxic and inexpensive. Second, these compounds can be used in high heat sources up to 1100 K with no sublimation in vacuum, and they are strongly resistant to oxidation at high temperature. Okada *et al.*[77] have

experimentally studied the oxidation process of $Mn_{27}Si_{47}$ crystals in air, and found that the oxidation reaction was just initiated at about 1033 K. Similarly, the oxidation of $Mn_{15}Si_{26}$ single crystals only started at approximately 1053 K, producing MnSi, γ-Mn_2O_3, and SiO_2.[78] Moreover, the HMS-based materials maintain good mechanical strength for a long period. Practically, the Vickers microhardness measured on the (100) plane of $Mn_{15}Si_{26}$ single crystals reaches a high value about 10 GPa.[78] Additionally, the figure of merit of the HMS compounds remains at an adequate value over a broad temperature range. Lastly, The HMS-based materials have a low neutron capture cross section, which is suitable for the thermoelectric applications inside thermal nuclear reactors.

Recently in 2013, Miyazaki and Kikuchi have provided a review on HMS, [79] covering many different aspects, e.g. chemical formula, crystal structure, single crystal growth, electronic structure, thermoelectric properties, and practical applications, which can be referred to in addition to the summary given here. The general formulas of HMS can be $MnSi_{2-x}$, $MnSi_{\gamma}$, or Mn_nSi_{2n-m}, depending on particular situations where the compounds are mentioned.

2.3.1 Nowotny chimney ladder structure

HMS adopt the Nowotny chimney ladder structure briefly described as the Mn atoms form the chimneys in which the Si atoms spiral as the ladders (Figure 2.4).[67]

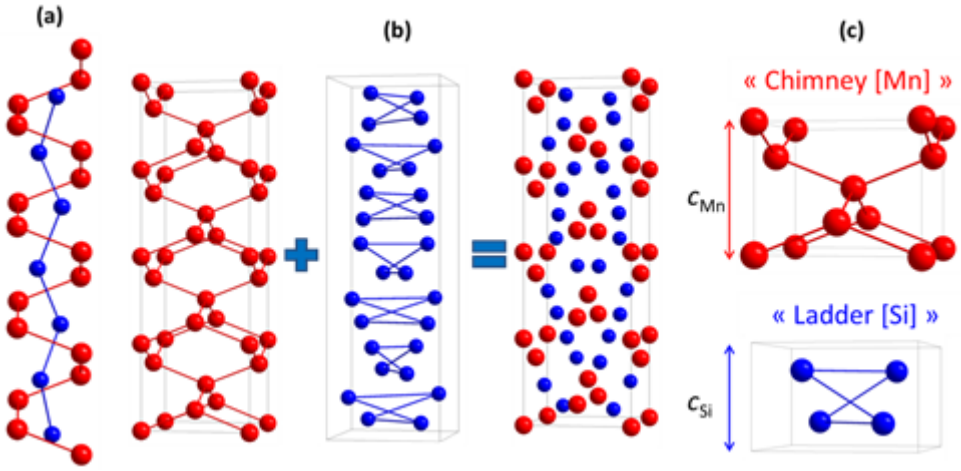

Figure 2.4 (a) Nowotny chimney ladder structure of HMS;[80] (b) Four stacked Mn subcells and seven stacked Si subcells to form Mn_4Si_7 compound;[80] (c) Mn and Si subcell.[81]

The structure was named after the Austrian chemist, Hans Nowotny, who was the first one describing the crystal chemistry of defect transition metal silicides.[82] According to Nowotny, the chimney ladder structure is derived from the $TiSi_2$-type structure, made of close packed layers stacked in the sequences of 1234 to avoid the contacts between Ti atoms from adjacent layers (Figure 2.5).[83] The Ti atoms in each layer are coordinated by six nearest Si atoms, while each Si atom is surrounded by two Ti atoms and four Si atoms.

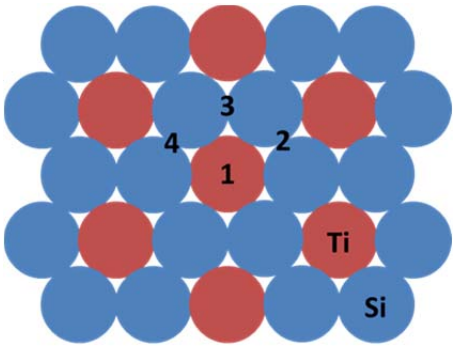

Figure 2.5 Close packed layers of $TiSi_2$.

The structure of defect manganese disilicides $MnSi_{2-x}$, where the term "defects" refers to the nonbonding vacancies, is an intermediate structure between the $TiSi_2$ type and the fluorite type, first recognized for the $Mn_{11}Si_{19}$ compound. Nowotny described the structure consisting of two partial lattices, where the Mn atoms form a diamondoid arrangement, while the Si atoms are regularly expanded due to the defect formation in comparison to the disilicide compound (Figure 2.4). The expansion of the Si partial lattice displaces these atoms out of the planes to prevent the interference with the neighboring transition metal atoms, resulting in a helix formation of Si atoms in the [001] direction.

The structural formulas of HMS can also be generally expressed as Mn_nSi_{2n-m}, where n is the multiplication of the subcells along the *c*-axis (Figure 2.4), e.g.the crystal structure of $Mn_{15}Si_{26}$ with n = 15 and m = 4 consisting of 15 stacked Mn subcells, where 52 Si pairs are oriented alternatively in opposite quadrants about the central axis along the *c* direction.[74] The value of n is sensitive to minor defect changes, resulting in various compounds with different structural formulas. Some substitutions, such as Cr or Fe at Mn sites, changed the value of n, implying the formation of different superstructures via reducing or increasing the defects by modifying the electron concentration. Because of the minor energetic differences between HMS compounds, Nowotny predicted that the formation of different n values strongly depends on the thermal and mechanical treatments.

It was found that the odd n and m values result in the $P\bar{4}n2$ space group, the even n and odd m values cause the $P\bar{4}c2$ space group, while the odd n and even m values lead to the $I\bar{4}2d$ characteristic group. The Si-Si interactions are loose, especially along the *c*-axis, allowing Si atoms to move flexibly along this direction, yielding different stacking periods of Si subcells, while maintaining that of Mn atoms. The short Mn-Si distances refined from single crystals of $Mn_{15}Si_{26}$,[74] which are significantly below the total elemental radius for Mn and Si, indicating covalent bonding characteristic.

The aforementioned HMS compounds have commensurate structures, where the c_{Si}/c_{Mn} ratios can be expressed as simple integers. If the ratio is irrational, the unit cell will have an infinite length along the *c*-axis, where the number of atomic sites grows significantly

and the structural analysis becomes practically impossible. A (3+1)-dimensional space was applied to describe the coordinates of $MnSi_{\gamma}$ and a modulation vector was used to index the electron diffraction pattern in this superspace group approach to reduce the number of input parameters.[84] Consequently, all the HMS phases having different 3*D* symmetries and lattice parameters could be universally treated as an identical $MnSi_{\gamma}$ compound with slightly different stoichiometric γ values.

2.3.2 Electronic structure

The late transition metal Nowotny chimney ladder phases, where the transition metal atoms belong to the groups 7-9, follow the 14 electron rule, which states that the compound is stable if each transition metal atom has an average of 14 valence electrons. Fredrickson *et al*.[85] have chemically explained the rule from extended Hückel calculations for $RuGa_2$ compound, resulting in a schematic molecular orbital diagram adopted here in the Mn_4Si_7 case (Figure 2.6). For each Mn_4Si_7 formulae, 20 Mn *d*-orbitals interact with (8 + x) *sp*-orbitals from the Si atoms, where x is the number of Si orbitals strongly interacting with the Mn ones, which generally depends on the studied *k*-point. These x Si *sp*-levels generate bonding and antibonding molecular orbitals with x Mn *d*-levels, leading to 8 Si-Si bonding, x Mn-Si bonding, and (20 – x) Mn nonbonding levels. Therefore, the total number of valence electrons is 56, calculated from 7 and 4 valence electrons for Mn and Si, respectively, corresponding to 14 electrons per Mn atom, and completely filling in 8 Si-Si, x Mn-Si, and (20 – x) Mn levels. Consequently, a forbidden gap arises in Mn_4Si_7 between the filled and unfilled orbitals, resulting in a semiconductor behavior with the Fermi level situated in the gap. If a Si deficiency exists or the Si/Mn atomic ratio is less than 1.75 as in Mn_4Si_7, the total valence electron will be reduced and the bonding and non-bonding molecular orbitals will be partially empty. As a consequence, the other formulas behave as heavily doped *p*-type semiconductors with the Fermi level locates inside the valence band, assuming that the band structures show no significant changes when Si/Mn atomic ratios are slightly modified.

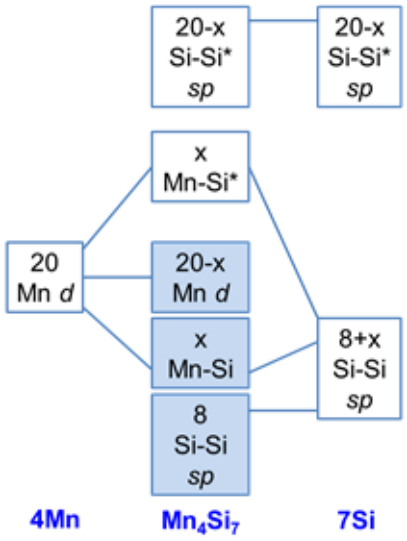

Figure 2.6 Schematic molecular orbital diagram for one Mn_4Si_7 formulae.[85]

The validity of the empirical rule of the 14 valence electrons has been studied for $Mn_{11}Si_{19}$ using a first-principle pseudopotential method, confirming that the Fermi level was located just below the energy gap.[86] Moreover, the theoretical and experimental investigations on the electronic and optical properties of HMS have confirmed the semiconductor behavior of Mn_4Si_7 and the metallic characteristic of $Mn_{11}Si_{19}$ and $Mn_{15}Si_{26}$.[87]

The bandgap value and type is a controversial issue due to structural variations, where theoretical and experimental data attain either a direct bandgap near 0.7 eV or an indirect gap near 0.4 eV. The photon energy dependence of the optical absorption coefficient revealed a direct gap of 0.68 eV,[88] while the temperature dependence of the electrical conductivity exhibited a bandgap of 0.70 eV with no information on the bandgap type.[89] Several other works have indicated the existence of a shallow indirect bandgap approximately 0.40-0.46 eV, such as the temperature dependence of electrical conductivity,[90] optical transmission and reflection,[91] ellipsometric measurement,[92] or the temperature dependence of Hall coefficient.[93]

Migas *et al.*[94] have reported an indirect bandgap of 0.77 eV via first principle calculations, which would possibly decrease in experimental measurements due to stacking

faults. Moreover, *ab initio* calculation methods, e.g. DFT, tend to overestimate the band gap energies of materials. Another calculated bandgap of approximately 0.6 eV with unclear type obtained from the modulated structure using the full potential linearized augmented plane-wave method (FLAPW) was in good agreement with the experimental value.[81]

The contradicting bandgap data could be attributed to slight differences in the structural parameters and local arrangements of Si atoms, originating from the small variation of γ, which can be varied by changing the starting compositions and the heat treatments of the materials. The structural parameters can be appropriately controlled by substituting at Mn or Si sites or introducing stacking faults.

2.3.3 Phase transformation between different HMS compounds

The HMS compounds were found to decompose to form MnSi due to a mechanochemical effect induced by the high-energy ball milling regardless of what materials the milling balls and vials are made from.[95,96] The internal energy of HMS is higher than that of MnSi judging from the much higher *c*/*a* ratio in these compounds than 1 in MnSi, so that the long *c*-axis structure could be broken into the smaller unit cells with shortened *c*-axis under high mechanical impact. The presence of the MnSi phase, which is more thermodynamically stable than the HMS compounds, would lower the free energy of the system. Moreover, the Fe doping effect was considered to be the dominant decomposition mechanism using stainless steel vials and balls to generate $Mn_{1-x}Fe_xSi$.[96] A noticeable decomposition took place when the particle sizes were reduced to a certain critical value corresponding to a few tens of HMS unit cells along the *c*-axis.

Zhou *et al*.[97] have investigated the grain size effects on the phase transformation of HMS using an energy dispersive XRD for the micro- (MPs) and nano-powders (NPs) obtained by ball milling an induction melt ingot. The authors found that the presence and intensity of the MnSi phase, occurs earlier and faster in the NPs than in the MPs due to the high internal energies, which can be depressed by applying a high pressure, and the HMS phases with a lower Si content are preferable with increasing temperature. However, no chemical reactions for any phase evolutions were specified in the report.

The stability ranges of different HMS phases have been investigated by *in situ* XRD on the materials prepared via arc melting, annealed at 773 K and 1073 K for two and one week, respectively, then quenched in water at room temperature to reach the equilibrium state.[98] The MnSi quantity in Si deficient sample remained stable from room temperature up to 1093 K, then increased up to 1153 K, and decreased again and disappeared at 1273 K. while the Si amount in silicon rich material was nearly constant from room temperature to 1133 K, then slightly decreased, and increased again at 1233 K. The angular difference between the peak located at $2\theta = 43°$ using Cu K_α radiation and its previous one, which increases as increasing the silicon content in HMS compounds, was considered to identify the corresponding HMS formulae. The results suggested that the only stable phase from room temperature up to at least 1273 K was $Mn_{27}Si_{47}$ regardless of starting compositions and heating procedures. Two phase transformations took place at higher temperatures, leading to the formation of $Mn_{15}Si_{26}$ and $Mn_{11}Si_{19}$, while no evidence of Mn_4Si_7 was observed. It has also been reported that the intensity and position of the peak at $2\theta = 43°$ was sensitive to the doping concentration of Ge or Re.[99,100] Accordingly, the phase transformation between various HMS formulas could be summarized using four following reactions, where the first and second reactions were applicable to Si deficient HMS materials, and the others were employed for Si rich compounds.

$$\text{At 1093 K: } 11Mn_{27}Si_{47} + 3MnSi \rightarrow 20Mn_{15}Si_{26}$$

$$\text{At 1153 K: } 8Mn_{15}Si_{26} + MnSi \rightarrow 11Mn_{11}Si_{19}$$

$$\text{At 1133 K: } 15Mn_{27}Si_{47} \rightarrow 27Mn_{15}Si_{26} + 3Si$$

$$\text{At 1233 K: } 11Mn_{15}Si_{26} \rightarrow 15Mn_{11}Si_{19} + Si$$

Subsequently, a new approach was investigated to synthesize Mn_4Si_7 compound, in which a bulk material with initial compositions $Mn_{35}Si_{65}$ underwent a heat treatment under 5 GPa, through the reaction between $Mn_{27}Si_{47}$ and unreacted elemental silicon.[101] Recently, Kikuchi *et al*.[102] have carried out an XRD study at high temperature on $MnSi_\gamma$ polycrystals prepared by arc melting. The results showed that the $MnSi_\gamma$ phase partially decompose to

produce MnSi above 773 K in vacuum. The MnSi amount increased with elevating temperature and conversely decreased above 1193 K.

Moreover, Zamanipour *et al.*[103] claimed that different HMS compositions were generated during the synthesis, judged from the peak shifts towards higher angles and the increased relative intensities when the Si/Mn atomic ratios change from 1.73 to 1.77. The corresponding melting points obtained from differential thermal analysis thermographs also showed slight differences from each other.

To conclude, the phase transformations as well as the stability range of different HMS phases are still the controversial issues. To the best of our knowledges, the phase stability in different temperature ranges and the formation of various HMS compounds depending on the composition of the starting materials has never been widely confirmed. On the other hand, the transformation between different HMS structural formulas is quite apparent, which can be induced by either thermal energy through heat treatments or mechanical energy via ball milling or using high pressure.

2.3.4 MnSi precipitations

HMS bulks materials were commonly synthesized from the melts, which was unfavorable to obtain the pure phases due to their incongruently melting characteristic. As a result, the MnSi phase was always precipitated when cooling down a liquid stoichiometric HMS phase. These precipitations are theoretically, not experimentally, avoidable by employing a rapid quenching rate. Consequently, the MnSi existence, which is undesirable for thermoelectric properties, is usually considered as an inherent property in the melt-grown HMS boules. Moreover, the stoichiometric composition of the melt was also modified owing to the evaporation of elemental Mn, especially in the Czochralski or Bridgman method.

In order to observe the microstructure and distribution of MnSi phase, the as-synthesized samples were etched by an acid solution containing hydrofluoric acid (HF). The monosilicide phase reacted with HF faster than the HMS compounds, resulting in marks on the matrix surface, which were observable via optical or electron microscopy.[104]

The MnSi morphology was somewhat peculiar,[105–107] which was commonly recognized as nearly parallel linear striations perpendicular to the *c*-axis of the HMS matrix (Figure 2.7). It was proposed that the layer morphology was caused by the anisotropic growth of the HMS phases, but a precise explanation was still unknown.[108] The microstructure and distribution of MnSi striations could be modified by either annealing,[89,109,110] or doping, e.g. Ge[99,104,108]or Cr.[111]

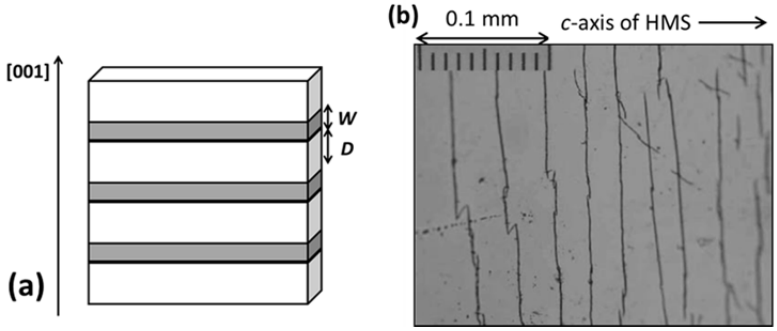

Figure 2.7 (a) Schematic drawing of MnSi linear striations (dark regions) in an HMS matrix (white regions); (b) MnSi layers segregated as black lines in Al-doped HMS,[112] Reprint from http://iopscience.iop.org/article/10.1143/JJAP.44.4275/meta, Copyright (c) 2005 The Japan Society of Applied Physics.

The presence of MnSi side products strongly influenced the thermoelectric properties in the [001] direction due to charge carrier and phonon scattering at the MnSi/HMS interfaces, thereby inducing anisotropy.[89,110] The presence of MnSi impurities at low concentrations mostly affected the carrier mobility and electrical resistivity due to charge carrier scattering and had little influences on the electronic structure, i.e. doping, Seebeck coefficient, or phonon transport, i.e. thermal conductivity.[99] Consequently, similar electrical properties for the materials cut perpendicular to the *c*-axis regardless of doping type and concentration have been observed.[112] Moreover, the discrete element circuit model showed that the true resistivity, thermopower, and thermal conductivity of pure HMS should be

higher than the measured values, which would lead to a three-fold improvement for the figure of merit.[107]

Apparently, the presence of MnSi in the incongruently melting HMS materials prepared by the melting techniques seems to be inevitable at the moment, which significantly affected their thermoelectric properties. The reason behind the particular morphology of this side product is still unknown, but theoretical calculations using the discrete element circuit model have shown that an improvement in thermoelectric performance of the HMS-based materials could be expected through completely eliminating the formation of MnSi.[107]

2.3.5 Thermoelectric properties

Single crystals of HMS exhibit a large anisotropy in their transport properties depending on the temperature. The electrical resistivity measured perpendicular and along the *c*-axis directions, $\rho_{\perp}$ and $\rho_{/\!/}$, differs 5 to 10 folds from each other, while the corresponding proportions of the Seebeck coefficient, $S_{\perp}/S_{/\!/}$, and the thermal conductivity, $\kappa_{\perp}/\kappa_{/\!/}$, are 1.5 and 2, respectively (Table 2.2).[113]

Table 2.2 Thermoelectric properties at room temperature.[107]

	S (μV/K)	ρ (mΩ.cm)	κ (W.m^{-1}.K^{-1})
MnSi	35	0.15	13
Mn_nSi_{2n-m}/MnSi (parallel to *c*-axis)	170	4.6	3.0
Mn_nSi_{2n-m}/MnSi (perpendicular to *c*-axis)	100	0.94	5.4

Polycrystalline materials are preferable for thermoelectric materials due to homogeneous and isotropic properties. The samples for the transport property measurements could be directly cut from the as-grown boules, or the densified pellets obtained from sintering the pulverized or solid state reacted powders. Occasionally, the element mixtures were mechanically alloyed or mixed before undergoing thermal treatments using conventional furnace or reactive sintering. Innovative techniques such as heating Mn

compacts in a Na-Si melt or chemical vapor transport were also employed to prepare the HMS compound, which resulted in low yields. The *ZT* of non-doped HMS was still less than unity regardless of various Si/Mn atomic ratios, mainly in the range from 0.3 to 0.5 (Table 2.3).

Table 2.3 The maximum figure of merit of non-doped HMS prepared by different methods; BM: ball milling; SSR: solid state reaction; HP: hot pressing; SPS: spark plasma sintering.

Composition	Method	$(ZT)_{max}$ at T	Reference
Mn_4Si_7	Induction melting Induction melting + HP	0.75 at 700 K 0.38 at 675 K	64
$Mn_{15}Si_{26}$	Vacuum levitation melting + BM+ HP	0.3 at 793 K	96
$MnSi_{1.733}$	Induction melting + HP	0.4 at 823 K	99,114
$MnSi_{1.8}$	SSR + BM + SPS	0.45 at 800 K	100
$MnSi_{1.75}$	Hard BM + Sintering	0.55 at 873 K	103
$MnSi_{1.80}$	BM + SPS	0.36 at 775 K	111
$Mn_{15}Si_{26}$	Vacuum levitation melting + HP	0.45 at 793 K	115
$MnSi_{1.75}$	Hard BM + Sintering Soft BM + Heat treatment + Sintering	0.47 at 773 K 0.4 at 773 K	116
$MnSi_{1.75}$	Soft BM + Heat treatment + Sintering	0.43 at 890 K	117
$MnSi_{1.75}$	Induction melting + SPS Induction melting + Annealing + SPS	0.62 at 800 K 0.4 at 800 K	118
$MnSi_{1.75}$	Heating Mn compact in Na-Si melt	0.31 at 798 K	119
$MnSi_{1.72}$	Furnace melting + SPS	0.63 at 723 K	120
$MnSi_{1.73}$	BM in hexane+ SPS	0.34 at 873 K	121
$MnSi_{1.73}$	Induction melting + HP	0.30 at 673 K	122
$MnSi_{1.85}$	BM + SPS	0.67 at 873 K	123
$MnSi_{1.7326}$	Arc melting + Annealing + SPS	0.45 at 800 K	124

$MnSi_{1.85}$	Mechanical milling + HP	0.29 at 723 K	[125]
$MnSi_{1.91}$	Arc melting + HP	0.63 at 723 K	[126]
$MnSi_{1.73}$	SSR + HP	0.33 at 823 K	[127,128]
$MnSi_{1.80}$	Induction melting + SPS	0.5 at 800 K	[129]
$MnSi_{1.74}$	Induction melting + SPS	(0.37 at 700 K)	[130]
$MnSi_{1.84}$	BM + Pulse discharge sintering	0.83 at 818 K	[44]
$MnSi_{1.75}$	Induction melting + SPS	0.42 at 800 K	[131]
$MnSi_{1.73}$	BM + Pulse discharge sintering	0.47 at 873 K	[132]
$MnSi_{1.73}$	BM + HP	0.28 at 823 K	[133]
$MnSi_{1.74}$	Induction melting + SPS	0.41 at 850 K	[134]
$MnSi_{1.73}$	Arc melting + SPS	0.4 at 723 K	[135]
$MnSi_{1.73}$	Hard BM + HP	0.5 at 823 K	[136]
$MnSi_{1.80}$	Induction melting + Annealing + SPS	0.45 at 850 K	[137]
$MnSi_{\gamma}$ ($\gamma \sim 1.7$)	Arc melting + Annealing	0.28 at 800 K	[138]
$MnSi_{1.74}$	BM + SPS Hand milling + SPS	0.1 at 723 K 0.4 at 723 K	[139]
$MnSi_{1.73}$	SSR+ Chemical vapor transport + SPS SSR + SPS	0.52 at 750 K 0.45 at 750 K	[140]

Various experimental efforts to improve thermoelectric performance of HMS compounds have been carried out through doing, e.g. Cr, Mo, Re, Fe, Ru at Mn sites, Al, Ge at Si sites, or compositing, e.g. Ag_2Te, PbTe, MnSi, Si_yGe_{1-y}, Yb, alumina (Table 2.4). Aside from the common doping elements, the others have been considered but not widely published yet, i.e. B at the Si sites, and Ti,[141] Cu, or Os (2015 TMS) at the Mn sites. Additionally, composites between HMS and $CeSi_2$ have also been prepared but the transport properties were incompletely reported.[142]

The defect manganese silicides were considered as carrier concentration-stabilized phases, especially with either Cr or Fe substitution.[143] Shi *et al.*[131] predicted an optimal

carrier concentration approximately 5×10^{20} cm^{-3} at 300 K for $MnSi_{1.75}$ according to a single parabolic band model, while it was indicated to be around 1.5×10^{20} cm^{-3} by Norouzzadeh *et al.*[144] for crystalline and bulk nanostructured HMS using a semi-classical two-band model including different scattering mechanisms for charge carriers.

The electronic and transport properties of substituted Mn_4Si_7 have recently been studied through DFT calculations with Co, Mo, Ru, Rh, Cd, Ir substituting at Mn sites, and Sb, Te, Pb, Bi substituting at Si sites.[87] The Mo- and Pb-substituted materials remained *p*-type, while a transition from *p*-type to *n*-type was observed for Ir, Co, Rh, and Ru, or Bi, Sb, and Te substitutions. The transport properties were simulated at different carrier concentrations, resulting in remarkable improvements for the power factors, especially in Bi, Sb, Te, Ru, and Ir cases when the carrier concentration was in the order of 10^{20} cm^{-3}. The power factor was significantly reduced when the carrier concetrations exceeded 10^{21} cm^{-3}. The best calculated value, which was 3.1×10^{-3} $W \cdot m^{-1} \cdot K^{-2}$, was achieved for the $Mn_{31}Ru_1Si_{56}$ compound at 1000 K, leading to a predicted *ZT* value of 1.55 using an experimental value for the thermal conductivity of pure HMS at the same temperature, which was approximately 2 $W \cdot m^{-1} \cdot K^{-1}$.[120]

The excitation of intrinsic carriers in HMS was usually initiated between 773 K and 873 K, depending on the compositions, which has been experimentally suppressed through adding nanostructured MnSi powder.[117] The Lorenz number for degenerate semiconductor of 2.44×10^{-8} $V^2 \cdot K^{-2}$ was commonly used for HMS-based materials to calculate the electronic thermal conductivity, while the extracted values from the measured electrical properties for Re-substituted HMS ranged from 1.3 to 1.7×10^{-8} $V^2 \cdot K^{-2}$.[100]

The lattice thermal conduction mostly dominated the total thermal conductivity of HMS (more than 75%), which could be reduced by enhancing phonon scattering through generating mass fluctuation, or introducing secondary phases to increase the interfaces, e.g. evenly distributed nanostructured MnSi powder.[117] The lowest lattice thermal conductivity with Re substitution was approaching the minimum value calculated using the Callaway and Cahill model, which is less than 1.5 $W \cdot m^{-1} \cdot K^{-1}$.[100]

To summarize, polycrystalline HMS-based materials have been extensively investigated through different synthesizing and processing methods, doping at the Mn and Si sites, nanostructuring, and compositing. Unfortunately, the thermoelectric performance of these materials remains at a moderate level, where the maximum *ZT* values mostly fell into the 0.3 – 0.5 range (Table 2.3 and Table 2.4).

Table 2.4 The maximum *ZT* of HMS-based materials i.e. composites (regular), and substituted compounds at the Mn sites (italic), at the Si sites (bold), and both sites (underline); the brackets signified the estimated *ZT* values.

Composition	$(ZT)_{max}$ at *T*	Reference
$MnSi_{1.733}$-0.02Si_yGe_{1-y}	0.5 at 823 K	114
$(Mn_{15}Si_{26})_{0.98}(Ag_2Te)_{0.02}$ $(Mn_{15}Si_{26})_{0.98}(PbTe)_{0.02}$	0.30 at 793 K 0.36 at 793 K	115
$(MnSi_{1.75})_{0.99}(MnSi)_{0.01}$	0.5 at 843 K	117
$MnSi_{1.73}$-1% Yb (nanoinclusions)	0.42 at 873 K	145
HMS-1 vol.-% alumina nanoparticles	0.58 at 800 K	146
$Mn_{0.95}Re_{0.05}Si_{1.75}$	0.59 at 675 K	64
$Re_{0.04}Mn_{0.96}Si_{1.8}$	0.57 at 800 K	100
Re-doped HMS	0.52 at 744 K	109
$Mn_{0.995}Cr_{0.005}Si_{1.80}$	0.29 at 825 K	111
$(Mn_{0.9}Fe_{0.1})Si_{1.75}$	0.31 at 798 K	119
$(Mn_{0.9}Fe_{0.1})Si_{1.7143}$ (p-type) *$(Mn_{0.7}Fe_{0.3})Si_{1.6809}$ (n-type)*	0.34 at 750 K 0.071 at 644 K	124
$MnSi_{1.73}$-$Cr_{0.01}$/$MnSi_{1.73}$-$Cr_{0.005}$	0.36 at 823 K	127,128
$Mn_{0.8}Cr_{0.2}Si_\gamma$	0.45 at 900 K	138
Re-doped HMS	0.64 at 800 K	141
$Mn_{0.95}Cr_{0.05}Si_{1.74}$/$Mn_{0.97}Cr_{0.03}Si_{1.74}$	0.6 at 850 K	147

$Ru_{0.1}Mn_{0.9}Si_{1.732}$	0.76 at 874 K	[148]
$MnSi_{1.73}$-0.19 wt.-% Fe	0.35 at 823 K	[149]
$Mn(Si_{0.95}Ge_{0.05})_{1.75}$	0.38 at 675 K	[64]
$Mn(Si_{0.992}Ge_{0.008})_{1.733}$	0.6 at 833 K	[99]
$Mn(Al_{0.0045}Si_{0.9955})_{1.8}$/$Mn(Al_{0.0035}Ge_{0.015}Si_{0.9815})_{1.8}$	0.57 at 823 K	[150]
$Mn(Al_{0.0015}Si_{0.9985})_{1.80}$	0.65 at 850 K	[129]
$Mn_{15}Si_{26}$ - ~ 1 at.-% Al	0.7 at 773 K	[151]
$(Mn_{0.98}Mo_{0.02})(Si_{0.9865}Al_{0.0035}Ge_{0.01})_{1.74}$ (//c-axis) $(Mn_{0.98}Mo_{0.02})(Si_{0.9865}Al_{0.0035}Ge_{0.01})_{1.74}$ ($\perp$ c-axis)	0.57 at 780 K 0.64 at 880 K	[112]
$Mn_{0.9}Fe_{0.1}Si_{1.65}Al_{0.1}$	(0.5 at 800 K)	[152]

2.3.6 The *n*-type HMS materials

Miyazaki *et al*.[81] predicted that a partial substitution of the Mn atoms with a heavier element will raise the Fermi level to the bottom of the conduction band, resulting in a comparable *n*-type thermoelectric performance to the *p*-type counterpart. The *n*-type HMS materials have been synthesized by substituting Ru,[148] or Fe,[124,143] at the Mn sites, or in the $(FeSi_2)_{0.3}(MnSi_{1.73})_{0.7}$ quasi-binary material containing around 4 at.-% excess silicon.[135] For Fe substitution, the transition from *p*-type to *n*-type took place at 28-30 at.-% of Fe. Moreover, the Co-substituted solid solution $(Mn_{1-x}Co_x)Si_\gamma$ has been prepared by arc melting and annealing.[153] The transition from *p*-type to *n*-type conduction was expected for $x > 0.06$, which was not experimentally observed for all solid solutions. However, the solubility limit prevented the increase of electron density in HMS matrix, which led to a high electrical resistivity in *n*-type materials. Currently, the thermoelectric performance of *n*-type HMS-based materials is inadequate for thermoelectric applications.

2.3.7 Single crystal growths

Single crystals of HMS were grown through solution-melt technique, using Sn,[72,154–156] Pb,[154,156] Ga,[78,155,156] Zn,[157] Cu,[156] as the fluxes. HMS phases were usually detected in

XRD patterns when silicon-rich mixtures were used, mixing together with MnSi and the elements. Different HMS compounds with various sizes have been identified depending on the growth conditions, e.g. $Mn_{11}Si_{19}$,[155] $Mn_{15}Si_{26}$,[78,156] $Mn_{27}Si_{47}$,[156] or Mn_4Si_7.[155] The single crystals were mostly in polyhedral shape with mirror-like facets. Occasionally, the obtained crystals were even big enough for the physical property measurements.[155]

The crystal growth through chemical vapor transport has been performed using different transport agent i.e. I_2,[158] or metal halides ($CuCl_2$, $FeCl_2$, $MnCl_2$, $ZnCl_2$, $AlCl_3$, $SnCl_2$, $CrCl_2$, MnI_2, FeI_2).[106,140,158] Single crystals with various shapes and sizes were obtained depending on the transport agent, e.g. fine crystals with the shape of a flat-top polygonal pyramid using I_2, large crystals around 1.5 mm in average sizes with the shape of long and narrow polyhedron using $CuCl_2$, small crystals with the shape of a polygonal pyramid using $MnCl_2$. The grown crystals contained no MnSi striations or contaminations, and mainly identified as $Mn_{15}Si_{26}$. However, the long growth duration up to several weeks has limited the application of this synthesis method in large scales. Among different metal halides, $CuCl_2$ and $FeCl_2$ were found to be effective transport agents for producing a large quantity of highly pure well-faceted crystals as large as approximately 2 mm.[140]

2.3.8 Thermoelectric applications

Different materials including metals i.e. Co, Ni, Cr, Ti, Mo, and silicides i.e. MnSi, $TiSi_2$ have been investigated to find the best contact for HMS.[159] The pure metals mostly failed to make reliable electrical contacts due to poor mechanical and chemical stability at high temperature, while the silicides exhibited excellent mechanical bonding and chemical and thermal resistance after the stability test. The contact resistance of silicides was within the range of practical interest up to 700°C (i.e. from 10^{-5} $\Omega \cdot cm^2$ to 10^{-4} $\Omega \cdot cm^2$), where nano-grained MnSi and $TiSi_2$ showed low contact resistance. Nickel was commonly considered to be one of the most appropriate contact materials for HMS thermoelectric modules.[160] However, the formation of Mn-Ni-Si intermetallic phases at the contact region usually causes cracks and voids due to different partial diffusion coefficients of the components and the brittleness of the intermetallic phases. Therefore, a chromium layer was used as a diffusion-

inhibiting barrier, leading to improve mechanical and electrical properties in HMS/Ni contact.[161,162]

A German research group has attempted to fabricate single couple thermoelectric generators comprising of *n*-type $Fe_{0.95}Co_{0.05}Si_2$ or $Fe_{0.93}Co_{0.07}Si_{1.99}Al_{0.01}$ and *p*-type $MnSi_{1.73}$.[122] The hot-side contact was made from a bridge made of $TiSi_2$ using titanium activated silver for soldering, while a Zn-Al-Cu alloy was used to solder the cold side. When the cold side temperature was kept at 373 K and the temperature difference was 600 K, an efficiency of 2.7% and 3% was obtained for two generators, respectively, measured in vacuum.

Aoyama *et al*.[112] have fabricated two types of thermoelectric module consisting of 8 pairs of *n*-type $Mg_2Si_{0.4}Sn_{0.6}$ and *p*-type (Al, Ge and Mo)-doped HMS legs parallel or perpendicular to the *c*-axis. The maximum conversion efficiency of the module with the *p*-type legs cut parallel to the *c*-axis was clearly higher than that with the legs sliced perpendicular to the *c*-axis due to a higher output power and lower heat flux. The highest efficiency reached 7.3 % when the cold-side and hot-side temperatures were 303 K and 823 K, respectively, with an output power of 5.5 W. Moreover, a high performance of 12.1% at the same temperatures was achieved for the cascaded module constructed by stacking the Bi_2Te_3-based and silicide modules together with a maximum total output power of 5.02 W.[163]

A direct contact *p*/*n* multilayer-type thermoelectric power generation block has been developed using *p*-type $MnSi_{1.74}$ and *n*-type $Mn_{0.7}Fe_{0.3}Si_{1.68}$ materials containing 10 *p*/*n* pairs with a thickness of 500 μm.[164] The maximum output was 0.0117 W when the cold and hot side temperatures were 293 K and 973 K, respectively. The engine test bench revealed an output of 0.0055 W and a voltage of around 0.6 V at the hot side temperature of 909 K and a temperature difference of 595 K.

In conclusion, bulk HMS-based materials have been widely investigated for thermoelectric modules. However, the efficiency of these modules is fairly low, requiring further optimizations in both the performance of the materials and the production technology of the modules.

2.4 Conclusions

The HMS compounds comprised of different structural formulas are the only binary phases which are interesting for thermoelectric materials. Eight formulas have been identified as HMS phases, where the Si contents vary between 63 at.-% and 64 at.-%, but only four of them have been synthesized as bulk samples, including Mn_4Si_7, $Mn_{11}Si_{19}$, $Mn_{15}Si_{26}$, and $Mn_{27}Si_{47}$. All the HMS phases crystallize in the tetragonal Nowotny chimney ladder structure composed of the Mn and Si sublattices with similar lengths of the *a*-axes and rational *c*-axis sizes.

The HMS phases follow the rule of 14 valence electrons, where the Mn_4Si_7 compound is an intrinsic semiconductor and the others exhibit the characteristics of heavily doped *p*-type semiconductors. The bandgap value and type is still in debate due to structural variations, which is either a direct bandgap near 0.7 eV or an indirect gap near 0.4 eV.

The transformations between different HMS phases have been induced through mechanical or thermal energy, but the stability range in different temperature and compositional ranges have not yet been established. The MnSi side product was unavoidable for the HMS materials prepared from the melts due to their incongruently melting characteristics, which significantly degraded the thermoelectric performance.

For thermoelectric applications, the polycrystalline HMS-based materials were preferred thanks to their homogeneous and isotropic properties. Various attempts have been carried on tuning the transport properties, such as changing the synthesis techniques, using different dopants, reducing the particle sizes, and introducing the secondary phases. However, the thermoelectric efficiency is still at an average level, where the maximum *ZT* values were mostly between 0.3 and 0.5 for the *p*-type formulations. The *n*-type materials have also been studied, but their performance is insufficient to be applied in thermoelectric modules.

All in all, several challenges still remain for the HMS system, including: i) to specify the conditions for preparing separately different HMS phases, which are decided by the energy of formation and kinetic factors, ii) to search for the unknown formulas, and iii)

identify the differences in physical properties between different HMS compounds. For thermoelectric applications, the *ZT* value, which is still less than 1, needs to be improved via eliminating undesirable side products by optimizing the synthesis conditions, tuning the carrier concentrations with appropriate dopants, and controlling the microstructures using powder metallurgy. Moreover, innovative preparation methods have to be investigated to achieve an effective and scalable process for industrial productions.

Chapter 3

Synthesis and characterization methods

Abstract

This chapter aims to cover all the synthesis techniques and characterization methods being used for HMS-based materials. At first, different preparation methods, i.e. solid state reactions, mechanical alloying, and chemical vapor transport will be consecutively described in the three sections 3.1, 3.2, and 3.3. Subsequently, the densification using either spark plasma sintering or hot pressing to achieve the solid pellets will be introduced in section 3.4. Next, the characterization of phase composition and morphology utilizing powder XRD and scanning electron microscopy, respectively, will be correspondingly given in section 3.5 and 3.6. Afterward, the techniques for measuring the physical properties of the materials will be presented in section 3.7, 3.8, and 3.9 for thermal diffusivity, carrier concentration and mobility, and electrical properties. Finally, the experimental errors will be briefly discussed in section 3.101, focusing on the aforementioned instruments and analyses.

3.1 Solid state reaction

Solid state reaction, or ceramic method, is the most common method for preparing polycrystalline solids from a mixture of solid starting materials.[165] Generally, solids are unable to react with each other at ambient temperature on typical time scales, even if the reaction is thermodynamically favorable. The ions or atoms are trapped on their appropriate lattice sites in the crystal structure through strong bonding interactions, which makes it hard to move to adjacent sites. Therefore, it is necessary to heat them up, often above 200°C, so that sufficient energy for the ions or atoms to diffuse through the lattice is provided and the reaction rate is appreciable.

To illustrate this method, the two reactants A and B are considered to be in an intimate contact with each other at one face (Figure 3.1). When no melts is formed during the process, the nucleation of the product C is started at the interface between A and B due to

structural reorganization. Once the product layer is formed, the reactants are no more in contact. In order for the reaction to progress, the ions from A have to diffuse to B through the product layer and vice versa. As the reaction continues, the product layer grows thicker, resulting in longer diffusion paths. The product layer acts as a barrier between the reactants, which gradually slows down the reaction rate.[166]

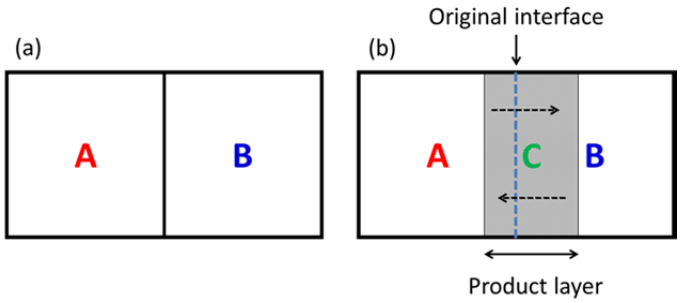

Figure 3.1 (a) Two reactants A and B in an intimate contact with each other at one face; (b) Diffusion from A to B and vice versa through the product layer C.

A conventional preparation procedure for a solid state reaction in practice involves:

(1) To select appropriate reacting agents, *i.e.* components, purity, particle sizes. The reactants are usually dried, purified, ground, and stored in the glove box under an inert argon atmosphere to prevent unwanted oxidation or hydration of the materials. The O_2 and H_2O pressure in the box is usually maintained below 2 ppm.

(2) To weigh out stoichiometric amounts of the starting materials. The weighing step is commonly carried out inside the glove box.

(3) To mix homogeneously the powder mixtures. The grinding and mixing process is usually done either manually in mortar and pestle or mechanically using milling machine. In order to maximize the contact, the reacting powders are often compressed into a pellet before undergoing heat treatments.

(4) To select the reaction atmosphere. The reaction can occur under a flowing gas, such as oxidative air, reductive hydrogen, inert argon, or vacuum. The gas is purged out of the quartz tube using a Schlenk vacuum line prior to sealing (Figure 3.2).

(5) To choose the container, depending on the reactivity, thermal stability, cost, and availability. Sealed quartz tube is a common option for solid state reaction. Inert crucibles, i.e. alumina, graphite, are occasionally inserted inside or graphite is coated over the inner wall side in case the reactants or products react with the tube (Figure 3.2).

(6) To decide on the heating profile. The temperature is selected to avoid the volatilization or decomposition of the substances, where an initial heating to a lower temperature is found to help. The heating and dwelling duration needs to be optimized to save time and energy as well as to achieve a complete reaction. Several remixing steps are often required to retain an appreciable reaction rate.

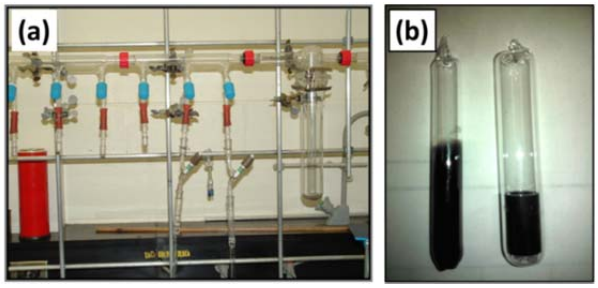

Figure 3.2 (a) Schlenk vacuum line; (b) Vacuum sealed quartz tube with graphite coating (left) and graphite crucible (right).

3.2 Mechanical alloying

Mechanical alloying (MA) is a solid state powder processing technique involving repeatedly cold welding, fracturing, and re-welding of powder particles using a high-energy ball-mill.[167,168] Through violently deforming the particles, the material is highly energized to a non-equilibrium (metastable) state. Subsequently, the material is quenched into a

configurationally frozen state, which can be employed as a precursor to achieve desired chemical constitution and microstructure through further heat treatment or processing. It is recognized that the powder mixtures can be mechanically activated to induce chemical reaction at a lower temperature than in a conventional solid state synthesis.

The planetary ball mills commonly referred as Pulverisette, manufactured by Fristch GmbH, Germany, are named after the planet-like movement of the vials. The vials rotate around their own axes and are arranged on a rotating support disk in the opposite directions, producing the centrifugal force to act on the materials and grinding balls inside the vials. Whenever two balls collide, a certain amount of powder is trapped between them (Figure 3.3). The impact forces plastically deform the particles leading to breaking down the particles. The new surfaces allow the particles to weld together resulting in an increase in particle sizes. Next, the particles get work hardened and fractured through a fatigue failure mechanism and fragmentation of the fragile flakes with continuous deformation. The tendency to fracture predominates over cold welding; therefore, the particle sizes are continuously reduced. Subsequently, the particle structure is steadily refined with continued impacts of grinding balls, but the particle sizes remain constant. The milling process also increases the amount of defects and dislocations in the structure. It's these features that enhance the diffusion of atoms in solid state reactions.

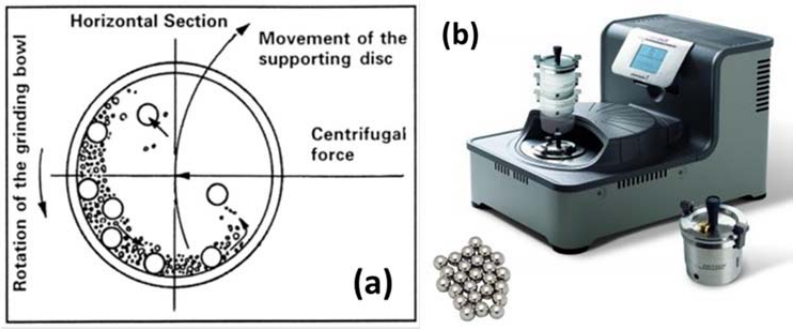

Figure 3.3 a) Schematic ball motion inside planetary ball mills,[167] reprinted from *Prog. Mater. Sci.*, *46*, C. Suryanarayana, Mechanical alloying and milling, 1-184, Copyright

(2001), with permission from Elsevier; (b) Pulverisette 7 premium line planetary mill from Fritsch GmbH with WC balls.

MA has been extensively investigated for the system of HMS, e.g. Ivanova has ball milled the as-melt ingot of Re-doped HMS using jasper vessel and balls.[141] Stainless steel ball mill were found to generate iron contamination in HMS, which can be reduced via using shorter milling time.[95,122] Zhou *et al*.[95] inferred that this contamination can induce phase transformation of HMS, which changes the compositional and phase configurations. Moreover, SiO_2 and WC are considered to be neutral to preclude the doping effect in HMS. The high density and hardness of WC compound helps to effectively refine the particles through generating more effective collisions. Therefore, WC vials/balls are able to depress the HMS decomposition and be suitable for nano-structuring process. Dry milling or using hexane milling media will promote the decomposition of HMS, while acetone or ethanol will depress the effect.[95]

Pulverisette 7 premium line planetary mill from Fritzsch GmbH was used for the ball milling experiments in this thesis (Figure 3.3). The machine consists of two stations for the vials with a capacity of 20 ml, which means that 1 - 9 ml of materials can be ground at one station in one run. The balls and mills are commercially available in seven different materials including: agate, silicon nitride, sintered corundum, zirconium oxide, stainless steel, hardened steel, tungsten carbide, where the list is in the order of increasing material density.

For a conventional ball milling procedure, the desired amount of balls is first placed in the empty vials. The reactants are then poured onto the balls, and the liquid phases are added in the end. A flat gasket seal made of silicone is inserted to simultaneously seal and relieve excess pressure during the milling process. The vials are then closed and sealed with the gas-tight lids, and placed into the machine. The processing parameters is set with the maximum possible entries including speed of 1100 rpm, time of 999 minutes, pause of 99 minutes, cycles of 99. The vials after milling experiments are usually at very high temperatures; therefore, they need to cool down before being removed from the machine.

3.3 Chemical vapor transport

Chemical vapor transport is a crystal growth method via the gas phase.[169,170] The process is characterized by a reversible conversion of non-volatile elements and compounds into their volatile derivatives (Figure 3.4). These derivatives are formed by chemical reactions of the starting materials with added transport agents, migrate throughout the reactor and deposit elsewhere. The deposition takes place due to the differences of the external conditions of the equilibrium between the positions of volatilization and crystallization (Figure 3.4). The choice of transport agent depends on the investigated systems to ensure that all solid components of the system are transferred into the gas phases.

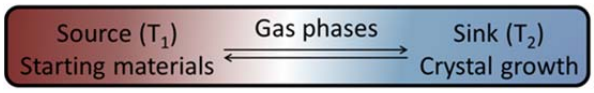

Figure 3.4 (a) Schematic illustration of chemical vapor transport; (b) Reaction tube inside a two zone furnace for chemical vapor transport.

A chemical vapor transport reaction can be divided into three steps: the forward reaction at the source material, the gas motion, and the reverse reaction leading to the formation of the solids at the crystallization zone. The basic precondition is that the transport reaction is not at the extreme equilibrium position, so that the dissolution into the gas phases and the solid re-condensation is possible under a slight change of experimental conditions. The exothermic transport reactions will transfer to the hot zone, and endothermic transport reactions will transfer to the cold zone.

The source materials and the transport agent are sealed in a silica tube under vacuum. Liquid nitrogen can be used to cool the tube during evacuating to prevent the evaporation of volatile transport agent, i.e. I_2. The amount of the powder mixture is limited to avoid explosions due to overpressure at elevated temperature. The tube is usually wide and long to enhance the transport rate as well as to ensure a sufficient temperature difference between the

hot and cold ends. The sealed tube is then placed properly inside a temperature difference, so that all the starting materials and the transport agent are at one side. The recrystallization zone can be cleaned prior to the transport reactions via placing the tube in the inverse direction and applying the heat treatments for a short time. The tube needs to be completely cooled down to room temperature before being removed from the furnace. The crystals are sometimes distributed along the tube walls, especially when the temperature gradient exists; therefore, cares need to be taken so as to not mix the final products with the starting materials.

3.4 Densification

Sintering is the term to describe the process wherein the particles are fused together to decrease the voids, eventually to achieve a dense solid body when a compacted powder is heated at an elevated temperature below its melting point. The driving force for sintering is the excess surface energy of a powder compact. The surface energy is reduced by decreasing the total surface area of the compact through mass transport for joining the particles together during heat treatments (Figure 3.5).

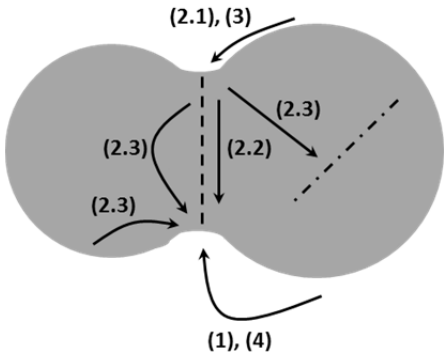

Figure 3.5 Diffusion paths during sintering: (1) Evaporation-condensation; (2) Diffusion: (2.1) Surface diffusion, (2.2) Grain boundary diffusion, (2.3) Volume diffusion; (3) Flow; (4) Dissolution-precipitation.[165]

The most important factors affecting the sintering process are particle sizes, particle packing and particle shape. Smaller particles accelerate the sintering process and lower the sintering temperature and pressure due to shorter diffusion distances, higher surface energy, and smaller pores to be filled. The average grain size increases, and the size distribution narrows as sintering progresses. Grain growth occurs especially in the final sintering stage, when the pores are gradually eliminated, and the relative density increases to above 0.95, and usually uncontrollable. Densification occurs faster with less volume shrinkage when the particle packing is improved to increase the contact areas between adjacent particles. Irregularly-shaped particles, having a high surface area to volume ratio, are sintered faster than equiaxed particles.

Spark plasma sintering (SPS) is a sintering technique utilizing a pulsed (on-off) direct electrical current (DC) to perform a rapid consolidation of powder.[171,172] A typical SPS system consists of a sintering machine with vertical uniaxial pressurization, a water-cooled chamber operating under vacuum or controlled atmosphere, a DC pulse generator, and a SPS controller (Figure 3.6). The powders are stacked inside the graphite die between two punches. The die is placed on the stage in the chamber between two electrodes. The process is based on the electrical spark discharge phenomenon, where a highly energetic, low voltage pulsed current momentarily generates spark plasma discharges at the local hot points, reaching several to ten thousand degrees Celsius, which facilitates thermal and electrolytic diffusion at the contacts (Figure 3.6). The evaporation and melting on the surface of powder particles occurs to form necks around the contact areas. However, the occurrence of a spark plasma discharge is still in debate and undetectable at the moment. Recently, the phrase "spark plasma sintering" has been referred to as “pulsed electric current sintering” (PECS) or “field assisted sintering” (FAS) to avoid any confusion. The passage of electrical current through the particles induces Joule heating, which assists the particles to be welded under mechanical pressure.

Punches and dies are made from electrically conductive graphite (used for pressure less than 100 MPa), and graphite papers and disks are wrapped around the inner walls of the graphite die and placed under the punches to prevent direct contacts between different

graphite parts and the materials, which facilitates the removals as well as guarantees an overall electrical contact. If the material is electrically conductive, which occurred for almost all thermoelectric materials, energy is dissipated directly within the sample and the electrically conductive parts of the pressing tool.

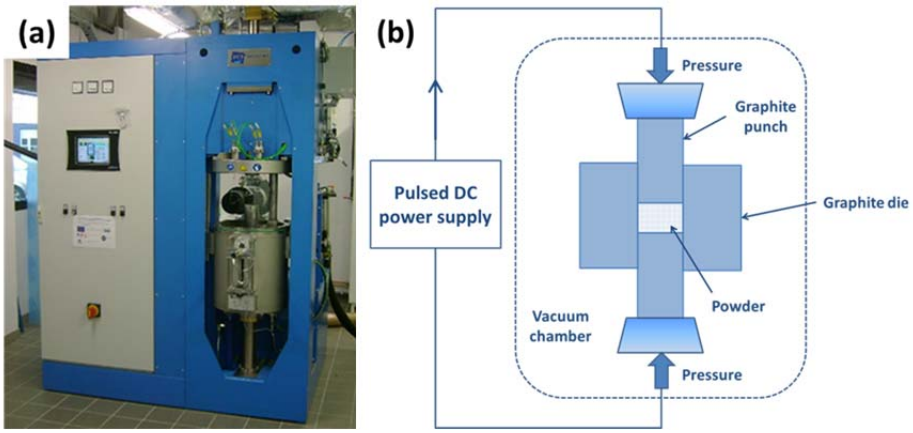

Figure 3.6 (a) Spark plasma sintering, Fritsch, GmbH – Caen, France; (b) Schematic drawing to explain the operational principles of SPS.

To obtain samples with high density, it is necessary to apply a sintering temperature that is at least two thirds of the melting or decomposition temperature of the materials. The SPS method can also be used to synthesize new compounds and densify materials in one step (Figure 3.7).

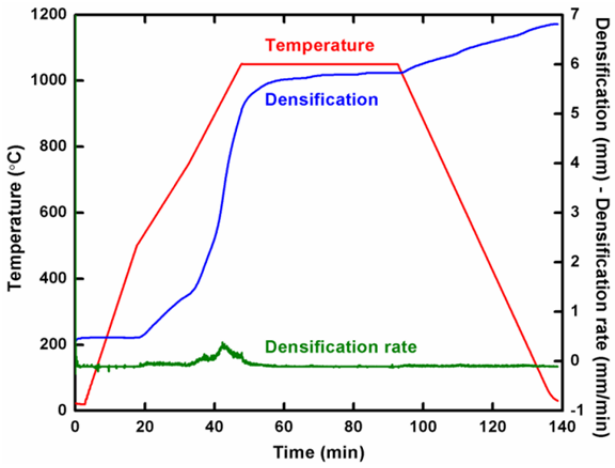

Figure 3.7 Typical sintering behavior for HMS-based materials using SPS including temperature (red line), densification (blue line), and densification rate (green line). The densification, which is actually the piston displacement, increase as the sample cools due to the contraction of the materials and the die upon cooling.

Hot pressing is a powder metallurgy method using simultaneous applications of heat and pressure to induce sintering process forming powder compact at elevated temperature (Figure 3.8). The sample assembly is heated by radiation from the enclosing furnace through external heating elements and convections of inert gases. Therefore, the heat transfer occurring through conduction from the outer surface of the graphite die to the inner powder heats the sample to a high temperature. The resulting heating rate is typically low and the process can take several hours. Most of the heat is wasted to warm up the whole volume of space rather than the actual sample. The hot presses using induction heaters are considerably more efficient and have very good heating rates. Hot pressing can occasionally occur in air because the heated graphite die can protect the materials from oxidation.[141]

The heating energy in a hot pressing process is distributed homogeneously on a macroscopic scale over the entire volume of the compact body, while the heating power is dissipated locally on a microscopic scale at the contact points of the particles in SPS. To lower the pressing temperature for HMS-based materials, titanium was added as a reductant. The same density previously achieved at 1390 - 1410 K was then reached at 1220 K with 2

wt.-% Ti addition.[141] However, this addition also resulted in a reduction of the Seebeck coefficient and an increase of the electrical resistivity of the material in the temperature range from 300 K to 1000 K, which degraded the thermoelectric performance of HMS.

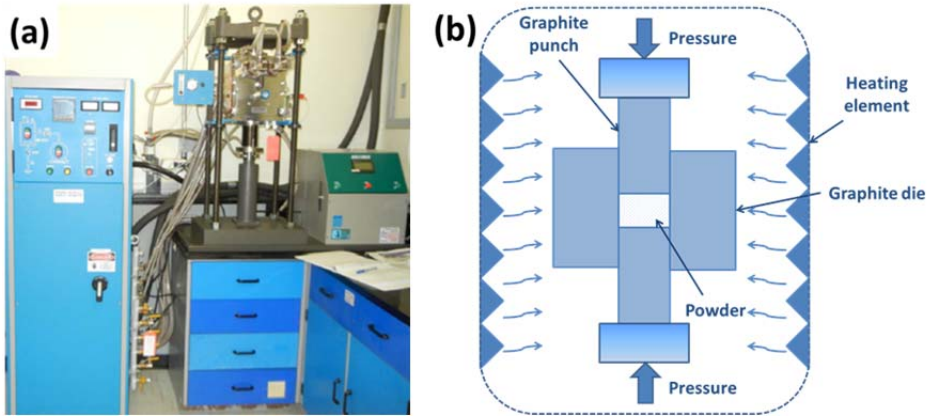

Figure 3.8 a) Hot pressing, Oxy-Gon Industries, INC. – Waterloo, Canada; (b) Schematic drawing to explain the operational principles.

3.5 Powder X-ray diffraction (P-XRD)

P-XRD is a non-destructive characterization method widely used in all scientific and technological fields.[173] X-ray is electromagnetic radiation with short wavelength lying between 0.01 and 10 nanometers. In particular, the radiations used in diffraction experiments are in the range from 0.07 to 0.25 nanometers (0.7 - 2.5 Å) to be in the same order of magnitude as atomic sizes and bond distances.

X-rays are generated using either laboratory scale X-ray tube or large scale synchrotron. For X-ray tube, the electrons are emitted from the cathode, a heated tungsten filament, and accelerated by a high voltage towards an anode, usually made of copper. The incident electrons possessing high energy can expel an electron out of inner shells of the bombarded atom. An electron from the outer shell, then, fills the vacancy, emitting an X-ray photon with energy equal to the difference of binding energies between the outer and inner electron shell. Therefore, X-ray wavelength is a characteristic of the target material. The

produced X-ray radiations are passed through several filters and collimators to achieve monochromatic and focused beams hitting the sample. A Phillips X-Pert Pro Panalytical diffractometer using Cu $K_{\alpha1}/K_{\alpha2}$ radiations (λ = 1.540598 Å, 1.544426 Å) is used in the CRISMAT laboratory in Caen, France, while an INEL powder diffractometer with a position-sensitive detector using a Cu $K_{\alpha1}$ radiation (λ = 1.540598 Å) is employed at Kleinke's research group in Waterloo, Canada, for P-XRD.

A synchrotron is a large scale facility to produce high intensity X-rays with precise wavelengths. The electrons are first accelerated by a linear accelerator before entering a racetrack shaped booster ring, in which their final speed at an energy level of 6 GeV for European Synchrotron Radiation Facility (ESRF) is reached. These electrons are injected into an enormous vacuum storage ring, containing bending magnets and insertion devices called undulators or wigglers. Intense X-ray radiation is released when the electrons change their orbital paths, which are projected in the forward directions to leave the storage ring and enter the beamlines, where they will be used for research (Figure 3.9).

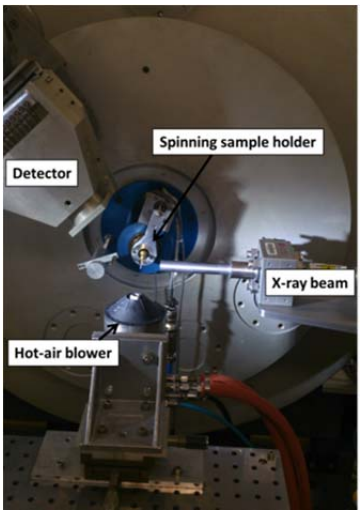

Figure 3.9 Beamline ID22 at ESRF - Grenoble, France.

XRD results from the interactions between X-rays and electrons of the atoms.[174] The interferences between the scattered radiations are constructive if the path difference between two diffracted rays differs by an integer multiple of the wavelength, as described by Bragg's equation (Figure 3.10). Generally, a typical diffraction pattern comprises of a series of reflections at certain diffraction angles, where each peak can be assign to a family of planes. The positions and intensities of the peaks is the fingerprint of a crystal structure consisting of specific atoms in specific planes. It's the number of the atoms and their atomic number *Z* that give the resultant diffraction intensity. Subsequently, the experimental pattern is compared to the reference for identifying the phase composition.

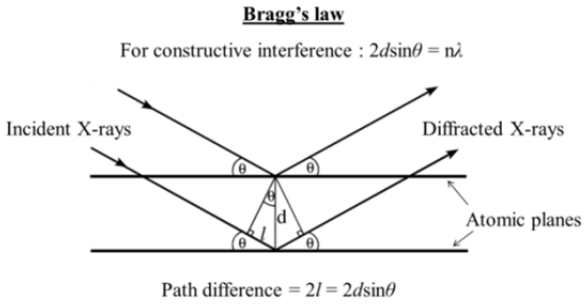

Figure 3.10 Bragg's law.[175]

An ideal polycrystalline sample for diffracting experiments contains randomly oriented crystallites, or coherently diffracting crystalline domains. In order to attain reproducible diffraction patterns, the powder is finely ground to less than 10 μm to have a sufficient large number of particles. In order to prepare for data collection, the powder is placed on an aluminum sample holder, flattened using a glass slide. The sample holder is mounted on rotating disc at the center of the beam path. The detector captures the diffracted beams at the 2θ angles and transferred the data to a computer for analysis. The collection time depends on the nature of sample and purpose. The XRD patterns of HMS-based materials usually contain high backgrounds due to the presence of manganese producing

fluorescence with copper radiations. Therefore, a long duration more than one hour is commonly used to achieve a reasonable peak profile.

In order to perform *In situ* P-XRD using synchrotron radiations, the samples were contained in borosilicate glass capillaries with 1 mm in diameter, prepared under helium atmosphere, and mounted on the diffractometer. The sample holder was spun at approximately 2 Hz during the data collection process to improve the powder averaging. For high temperature experiments, the samples were heated using a hot-air blower with the heating rate of 2ºC/min. The diffraction patterns were recorded for 20 minutes at each temperature during heating and cooling operations.

3.6 Scanning electron microscope (SEM)

SEM is an instrument for the studies of microstructural morphology and chemical compositions, where a focused electron beam is utilized to systematically scan across the surface of the specimen, generating a large amount of signals (**Error! Reference source not found.**).[176]

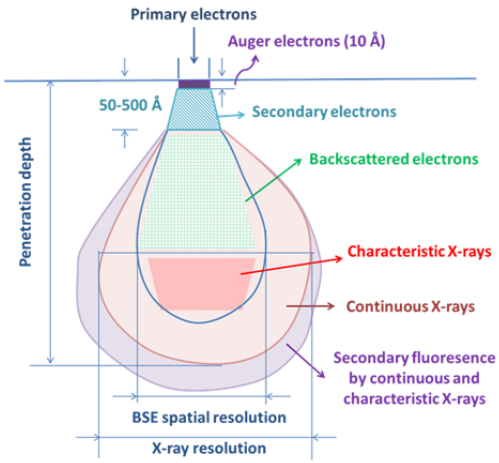

Figure 3.11 Schematic drawings of interactions between electrons and matters.

The incident electrons interact with the electrons and atoms of the specimen, transferring a substantial amount of energy to the atom (inelastic scattering). The ionization of the atoms releases loosely bound electrons, generating secondary electrons (SE) beam used to image or analyze. These electrons have low energy approximately 3-5 eV, escaping from a few nanometers from the specimen surface. SE provides topographic contrast with high resolution, i.e. surface texture and roughness in the order of less than 10 nm, especially with low energy incident electrons.

The incident electrons are deflected by the atomic nucleus or outer shell electrons with similar energy (elastic scattering), resulting in a negligible energy loss and a wide-angle directional change of the scattered electrons. Backscattered electrons (BSE) are produced through large angle elastically scattering (>90°) yielding signals for imaging. BSE undergoes several scattering events, bouncing back with energy greater than 50 eV, providing both compositional and topographic information. BSE provides atomic number contrast in the SEM images, where heavier elements appear brighter, and the features underneath the surface due to the large escape depth of the signals. The lateral resolution of a BSE image is around 1 μm.

Energy Dispersive X-ray Spectroscopy (EDS or EDX) is a qualitative and quantitative X-ray microanalytical technique accompanying SEM, which provides information on the chemical compositions of a sample for the elements after lithium in the periodic table ($Z > 3$)**.** When the primary electron collides with the atoms and kicks out an electron from an inner shell, an outer shell electron falls into the empty space, emitting a characteristic X-ray photon. The energy of the emitted X-ray photon is equal to the difference between the ionization energies of the electrons involved in the transition, which is characteristic for the element. The emitted X-rays are detected by an energy dispersive detector which presents the signals as a histogram of number of X-rays or X-ray count rate versus X-ray energy. The elemental identification is determined via the energies of the characteristic X-rays, while the intensities of the characteristic X-ray peaks quantify the concentrations of the corresponding elements. The typical spatial resolution for X-ray microanalysis in SEM is on the order of a few microns. The detection limit of EDS analysis

in SEM is approximately 0.1-0.5 wt.-%, depending on chemical compositions of the sample being analyzed. The level of precision is lowered with the presence of elements having similar atomic numbers *Z* or a poor sample preparation.

X-ray element distribution maps can be produced via a raster of the electron beam over a rectangular area of the sample in SEM imaging. The elemental X-ray map is a record of the number of X-ray photons of a specified energy generated from each point over a fixed duration, which is converted into a brightness value for a pixel on the screen or digital image to be displayed with the assigned colors in the final image. The total acquisition time varies from around 0.5 hours to more than 12 hours, depending on the required resolution and the dwelling time.

Fortunately, typical thermoelectric materials are conductive enough to be directly loaded on the carbon tape for a SEM observation. The sintered sample can simply be broken into several pieces to observe the fracture surfaces. In order to perform EDS analysis, the sample is immersed in wax and mirror polished, or else a somewhat flat surface should be chosen.

3.7 Laser flash method

Laser flash apparatus is a widely used instrument for measuring the thermal diffusivity of bulk samples.[177,178] One side of the sample is irradiated by a short (< 1 ms) laser pulse, and the high energy of the pulse is absorbed on the front surface. The heat then conducts through the sample's thickness to induce a temperature rise at the opposite plane-parallel side, which is monitored through an IR detector (Figure 3.12 (a)). The temperature rise versus time profile (a thermogram) is recorded for calculating the thermal diffusivity (Figure 3.12 (b)). The thermogram depends on the thermal diffusivity of the sample and the heat loss factor, which represents the heat exchange between the sample and the environment. The thermal diffusivity is measurable from 10^{-7} to 10^{-3} m^2/s in a broad temperature range from 75 to 2800 K.[179179]

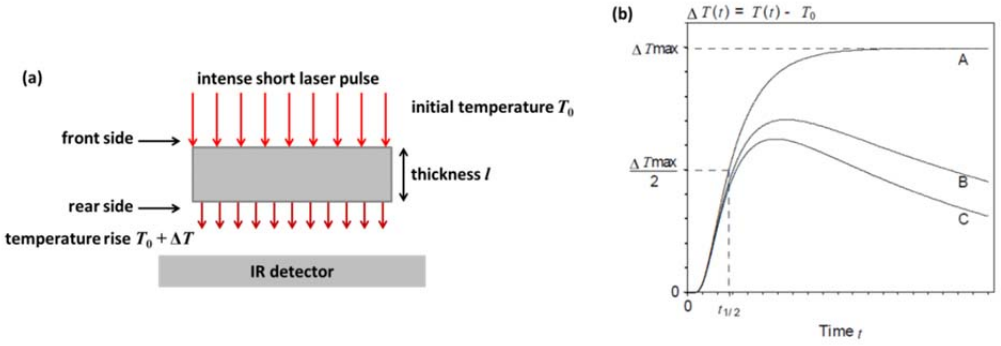

Figure 3.12 (a) Schematic principle of laser flash method; (b) Characteristic thermogram with no (A) and increasing (B, C) heat losses, reprinted with permission from [W. J. Parker, R. J. Jenkins, C. P. Butler, and G. L. Abbott, *J. Appl. Phys*. **1961**, *32*, 1679-1684]. Copyright [1961], AIP Publishing LLC.[180]

Different analysis techniques accompany the laser flash method, including the Parker, Cowan, Cape and Lehman, Larson and Koyama, Heckman, Clark and Taylor, Koski, and Degiovanni techniques, where the solutions from Cape and Lehman, or Clark and Taylor have been used here. The differences between various techniques usually fell within the experimental error range.

Parker *et al*.[180] in 1961 have proposed an ideal solution to calculate the thermal diffusivity, α, from the thickness of the sample, l, and the time for the temperature of the rear surface to reach one-half of the maximum value, $t_{1/2}$ (Eq. 3.1).

$$\alpha = \frac{1.38}{\pi^2} \times \frac{l^2}{t_{1/2}} \qquad \text{(Eq. 3.1)}$$

Several strict conditions need to be assumed for achieving the ideal solutions, including homogeneous and isotropic materials, very thin specimen, temperature invariant properties within the experimental conditions, instantaneous irradiation, homogeneous heating over the entire front side of the sample, negligible heat losses, and one directional heat flows.

Cowan in 1962 has observed a gradual decrease in the temperature change after the maximum temperature value.[181] He then included the radiative heat losses from the front surface after being irradiated by the intense laser pulse, which results in less temperature change than in the ideal solution, assuming that the pulse time is much shorter than $t_{1/2}$ (Eq. 3.2).

$$\alpha \times t_{1/2} = c \times l^2 \qquad \text{(Eq. 3.2)}$$

where c is a constant related to the ratio between the temperature at five time of $t_{1/2}$ and that of $t_{1/2}$ (Eq. 3.3).

$$c = \frac{1.38}{\pi^2} \times \frac{T_{5t_{1/2}}}{T_{t_{1/2}}} \qquad \text{(Eq. 3.3)}$$

Cape and Lehman in 1963 have attempted to correct the radiation and finite pulse time effects through optimizing the sample thickness.[182] An optimum thickness is required for a given material at a given pulse time to avoid the influences of radiative losses and finite pulse width at high temperature.

Clark and Taylor in 1975 have also included the radiative losses in their calculations of thermal diffusivity.[183] They considered the temperature rise curve before the peak at the points of 0.2 × ΔT, 0.3 × ΔT, 0.4 × ΔT, 0.7 × ΔT, and 0.8 × ΔT, and set up different values of c parameters based on the three ratios of $T_{0.8}/T_{0.2}$, $T_{0.7}/T_{0.3}$, and $T_{0.8}/T_{0.4}$.

A Netzsch LFA 457 Micro Flash measuring system[184] with a wavelength of the laser λ = 1054 nm and an IR detector made of InSb is ulitized in Crismat for the measurements of thermal diffusivity (Figure 3.13 (a)). The sintered samples are cut into square pieces of 6 × 6 × 1 mm^3, and polished to obtain parallel surfaces. The experiments are performed under a nitrogen flow of 20 ml/min from room temperature to 873 K. The sample is measured three times at each temperature, and an average value is then deduced.

The Anter Flashline 3000 apparatus (Figure 3.13 (b)) in Kleinke's research group contains a Xenon flash source, a graphite sample holder able to hold three samples coupled with a furnace, an environmental control chamber operating under an argon flow, a

temperature response IR detector, and a recording device. The operation of the entire instrument is fully computer controlled and automatic. The sample is a thin disc with a diameter of 12.7 mm. The optimum thickness, typically from 1 to 6 mm, depends on the magnitude of the thermal diffusivity, which should be chosen so that the time to reach the maximum temperature is between 40 and 200 milliseconds.[179]

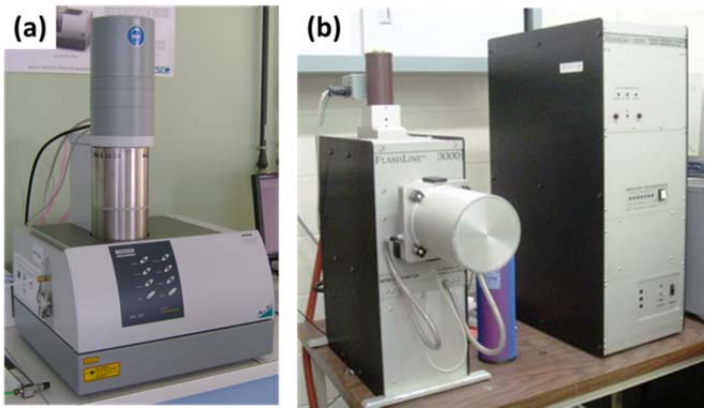

Figure 3.13 (a) Netzsch's LFA 457 Micro Flash; (b) Anter Flashline 3000.

3.8 Hall measurement

Edwin Herbert Hall, an American physicist, in 1879 observed a transverse voltage induced across a metal leaf carrying a current flow in an applied magnetic field. The Hall effect states that when a magnetic field is applied at a right angle to the direction of an electric current, an electric field appears perpendicular to the direction of both the current and the magnetic field (Figure 3.14).[185] The underlying physical principle is the Lorentz force, which acts on an electron moving along the electric field, I, along the x-axis, within an applied magnetic field, B, along the z-axis. The Lorentz force causes the electrons to drift away from the current direction toward the y-axis, which results in an excess surface charge on this side of the sample. This charge accumulation induces a potential difference across the two sides of the specimen, called the Hall voltage, V_H.

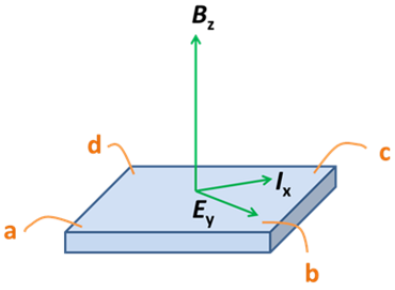

Figure 3.14 Schematic drawing of Hall effect.

Hall measurement is a common technique to determine the carrier density and mobility in semiconductor materials. Once the Hall voltage, V_H, is measured, the carrier concentration, n, can be deduced from the voltage value, the elementary charge, q = 1.602 × 10^{-19} C, and the known variables, i.e. the sample thickness, d, the applied electric and magnetic field, I and B, respectively (Eq. 3.4).

$$|V_H| = \frac{1}{nqd} IB \qquad \text{(Eq. 3.4)}$$

R_H is defined as the Hall coefficient, which can be either negative or positive, depending on the type of major charge carriers, which are electrons or holes, respectively (Eq. 3.5).

$$|R_H| = \frac{1}{nq} \qquad \text{(Eq. 3.5)}$$

The carrier mobility, μ, is then calculated from the electrical resistivity, ρ, at the same temperature with the Hall experiment (Eq. 3.6).

$$\mu = \frac{1}{nq\rho} \qquad \text{(Eq. 3.6)}$$

Physical property measurement system (PPMS) from Quantum Design is used to carry out Hall measurements in Crismat. The solid sample is cut into a square platelet of 3 x

3 mm^2 and polished to a very small thickness, which is ideally less than 0.5 mm. However, a size of 0.7 to 0.9 mm was applicable for HMS-based materials due to their high brittleness and hardness. The copper wires are soldered onto the four corners of the sample using indium. An alternative electric current of 5 mA is applied between two opposite corners (a and c), while a perpendicular magnetic field from -9 to 9 Tesla is provided at 300 K. The resistance, which is proportional to the induced Hall voltage, is measured between the other two corners (b and d). The slope from the linear fit of the resistance versus the magnetic field provides the Hall coefficient, from which the carrier concentration can be deduced. Subsequently, the carrier mobility is determined using the electrical resistivity measured at the same temperature in a separate experiment.

3.9 Electrical property measurement

ZEM-3 (ULVAC-RIKO) is the instrument designed to measure Seebeck coefficient and electrical resistivity of thermoelectric materials under a partial pressure of helium atmosphere (Figure 3.15).

Figure 3.15 ZEM-3 Model M8 measuring from room temperature up to 800°C, using thermocouple probe type R and electrode type Ni.

The sample shape can be either a rectangular parallelepiped or cylinder, where the widths or diameter are from 2 to 4 mm, and the length is between 5 and 22 mm. The sample

is polished in such a way that the top and bottom ends are reasonably parallel to each other and flat to ensure electrical contact with the electrodes. The sample size and geometry does not affect the results, and the preferred minimum sizes are $2 \times 2 \times 10$ mm^3 to reduce experimental errors.

After the sample is mounted between the electrodes and the gas displacement is carried on, the measurement program is set up including the sample parameters and the temperature profile. The measurement is started after obtaining a linear *V*-*I* plot to ensure electrical contacts. The temperature is stabilized in each step before the resistance and Seebeck coefficient are measured. The measurement data is then analyzed using specific software to achieve the final average values and eliminate the effects of the wires.

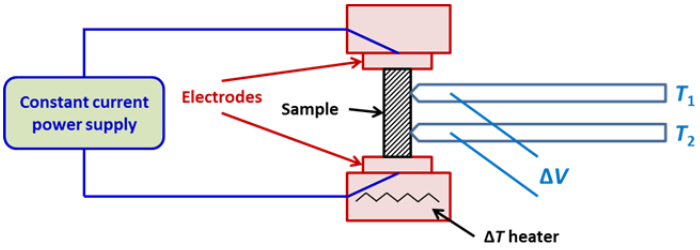

Figure 3.16 Schematic drawing to illustrate the measurement principles in ZEM-3.

The sample resistance, *R*, is calculated via the current passing through the electrodes and the sample, *I*, set with the constant current power supply, and the measured voltage between the thermocouples, ΔV ((Eq. 3.7), Figure 3.16).

$$R = \frac{\Delta V}{I} \qquad \text{(Eq. 3.7)}$$

Consequently, the electrical resistivity, ρ, is derived from the resistance, *R*, the cross sectional area of the sample, *A*, and the probe separation distance, *l* (Eq. 3.8).

$$\rho = \frac{R \times A}{l} \qquad \text{(Eq. 3.8)}$$

The Seebeck coefficient, S, is deduced from measuring the temperatures at the two probes, T_1 and T_2, and the induced voltage between the thermocouples, ΔV, when a temperature difference, ΔT, is applied between the two blocks ((Eq. 3.9), Figure 3.16).

$$S = \frac{\Delta V}{T_2 - T_1} \qquad \text{(Eq. 3.9)}$$

3.10 Experimental errors

All measurements are subjected to some uncertainties due to a wide range of errors and inaccuracies.[186,187] There are three main sources of experimental errors, i.e. the accuracy of the measuring apparatus, the limitations and simplifications of the experimental procedure, and the uncontrolled changes to the environment.

There exist two types of errors. Systematic errors are associated with the particular instrument or measurement technique being used, which affects the accuracy of a measurement, deciding how the yielded results differ from the true or accepted value. Systematic errors are difficult to detect, and cannot be analyzed by statistical method. Random errors are produced by a large number of unpredictable and unknown variations in the experiment. It is possible to deal with random errors using statistical analysis. Random errors are easily, which affect the precision of a measurement, deciding how the results fluctuate around the true or accepted values.

The experimental errors are reported as either absolute or relative values. The absolute error is usually specified by the manufacturer (Eq. 3.10), while the relative error can be calculated if the true or accepted value is known (Eq. 3.11). Generally, the relative error can be estimated through repeating the experiment at the same conditions.

$$\text{Absolute error} = \left|\text{Experimental value - True value}\right| \qquad \text{(Eq. 3.10)}$$

$$\text{Relative error} = \frac{\left|\text{Experimental value - True value}\right|}{\text{True value}} \times 100\% \qquad \text{(Eq. 3.11)}$$

If various measurements are used to calculate a result, the error of the result will depend on the errors of the individual measurements. Supposing that a quantity Q depends upon several observed quantities a, b, c, …, the error ΔQ and the relative error $\Delta Q/Q$ can be calculated from individual errors Δa, Δb, Δc, ..., and the partial derivatives of Q with respect to a, b, c, … e.g. $\partial Q/\partial a$, $\partial Q/\partial b$, $\partial Q/\partial c$, ...((Eq. 3.12), (Eq. 3.13)).

$$\Delta Q = \frac{\partial Q}{\partial a}\Delta a + \frac{\partial Q}{\partial b}\Delta b + \frac{\partial Q}{\partial c}\Delta c + \ldots \quad \text{(Eq. 3.12)}$$

$$\frac{\Delta Q}{Q} = \frac{1}{Q}\frac{\partial Q}{\partial a}\Delta a + \frac{1}{Q}\frac{\partial Q}{\partial b}\Delta b + \frac{1}{Q}\frac{\partial Q}{\partial c}\Delta c + \ldots \quad \text{(Eq. 3.13)}$$

For thermoelectric property measurements, the widely accepted fractional errors for Seebeck coefficients and electrical resistivity are 3% and 5%, respectively, using ZEM3. The fractional error for thermal conductivity is commonly 5%. Consequently, the experimental error of ZT is estimated to be 16% (Eq. 3.14).

$$\frac{\Delta ZT}{ZT} = 2\frac{\Delta S}{S} + \frac{\Delta \rho}{\rho} + \frac{\Delta \kappa}{\kappa} \quad \text{(Eq. 3.14)}$$

Moreover, a relative error of around 9% for ZT is obtained from the variance formula, which is commonly agreed among experimentalists (Eq. 3.15).

$$\frac{\Delta ZT}{ZT} = \sqrt{\left(2\frac{\Delta S}{S}\right)^2 + \left(\frac{\Delta \rho}{\rho}\right)^2 + \left(\frac{\Delta \kappa}{\kappa}\right)^2} \quad \text{(Eq. 3.15)}$$

Chapter 4

Thermoelectric properties of higher manganese silicide-based composites[I]

Abstract

Composites made of Higher Manganese Silicide (HMS)-based compounds, i.e. $Mn_{15}Si_{26}$, $MnSi_{1.75}Ge_{0.02}$, and $MnSi_{1.75}$, and nano-inclusions, i.e. fullerenes C_{60}, and multi-walled carbon nanotubes (MWCNTs), were prepared through different methods, i.e. solid state reaction, manually mixing, and hot pressing, or mechanical milling under mild conditions and reactive spark plasma sintering. The later approach has proved its easiness and effectiveness in synthesizing the MWCNT/HMS-based material composites mainly containing the HMS phases in a short period of time. SEM compositional mappings showed a homogeneous dispersion of MWCNTs in the HMS-based matrix. Electronic and thermal transport properties were measured from room temperature to 875 K. While power factors were virtually unchanged by the addition of MWCNTs, the lattice thermal conductivity was significantly reduced by about 30%. As a consequence, the maximum figure of merit for the MWCNT/HMS-based material composite with 1.0 wt.-% MWCNTs was improved by about 20% compared to the MWCNT-free HMS-based sample. Further increasing the content of MWCNTs up to 2.0 wt.-% degraded the thermoelectric performance due to increasing the electrical resistivity and slightly raising the total thermal conductivity. The results revealed that a fine distribution of nano-inclusions played a crucial role in reducing thermal conductivity through enhancing phonon scattering in HMS-based materials.

4.1 Introduction

Recently, a variety of studies has been conducted on tuning the transport properties of polycrystalline HMS to improve their performance for thermoelectric applications.[112,129,144]

[I] Part of this chapter is reprinted from http://dx.doi.org/10.1039/C4DT01441C.

However, the efficiency of HMS-based materials still remains at a moderate level as their thermoelectric figure of merit is typically not greater than 0.6.[129] This is mainly due to their high thermal conductivity compared to conventional materials such as Bi_2Te_3 or PbTe. Interestingly, the dominant contribution of the thermal conductivity of HMS comes from the phononic term that represents approximately 70% of the total value.[115] Therefore, one strategy to improve the thermoelectric performance of HMS consists of reducing their lattice thermal conductivity.

It has been previously reported that the introduction of selected secondary phases within the matrix can increase the phonon scattering at the interfaces, e.g. at the grain boundaries. Some examples of these composites are given as Si nanowires/Ge,[188] single-walled carbon nanotubes/Si_3N_4,[189] amorphous SiO_2 nanoparticles/$(Bi_2Te_3)_{0.2}(Sb_2Te_3)_{0.8}$,[190] or graphene/PbTe,[191] where the first mentioned phases are the added secondary phases, and the later ones are the matrix materials. For HMS, several studies on different composites have been reported, utilizing secondary phases such as Ag_2Te,[115] PbTe,[115] $CeSi_2$,[142] Si_yGe_{1-y},[114] in situ formed[118] and externally processed[117] MnSi, Yb nano-inclusions,[145] and alumina nanoparticles.[146] In all these cases with the exception of $CeSi_2$, a reduction of thermal conductivity was observed and attributed to either the low thermal conductivity of the secondary phases or the enhancement of phonon scattering due to the increased impurity concentration at the grain boundaries.

According to the Bergman theory, the effective *ZT* of a composite cannot exceed the value of its constituents in the absence of size and interface effects. Therefore, the sizes and distributions of these secondary phases are considered to affect the transport properties of the host materials. A random distribution of Ag_2Te and PbTe micro grains,[115] $CeSi_2$ fine particles,[142] Si–Ge micro dots and strips,[114] Yb pinning points and nanometer agglomerations[145] along the grain boundaries of HMS materials was noted, and small Yb particles dispersed in the bulk composites were also observed.[145] From the composites with Ag_2Te and PbTe, Zhou *et al.*[115] first proposed that a fine dispersion is necessary to enhance the thermoelectric performance of HMS-based composites. Furthermore, Luo *et al.*[118] prepared p-type HMS with in situ formed nano-sized and evenly distributed MnSi, and

reported a huge improvement of more than 50% of the thermoelectric figure of merit up to 0.62 at 800 K compared to that with micro-sized, and unevenly distributed MnSi. Lately, Shi *et al*.[117] added a small amount (about 1 at.-%) of externally processed, nanostructured MnSi to $MnSi_{1.75}$, and observed a reduction in both the lattice and ambipolar thermal conductivity, but the morphology and distribution of the secondary phase was not clarified in the report. Moreover, uniform dispersion of alumina nanoparticles at the HMS grain boundaries has helped to reduce the lattice thermal conductivity and improve the thermoelectric performance of the matrix material by 25%.[146]

Fullerenes, named as buckminsterfullerenes or buckyballs, C_{60}, and their derivatives possess a great number of potentially useful physical, chemical, and biological properties, e.g. highly electrically conductive, resilient to high temperature and pressure, selectively reactive with various species while maintaining the spherical geometry, possible to entrap any element from the periodic table, and fairly soluble in common solvents.[192] C_{60} has been extensively applied for different biomedical applications, e.g. antioxidants, high performance MRI and X-ray contrast agents, photodynamic therapy, or drug and gene delivery, and many other practical aspects, e.g. organic photovoltaics, catalysts, water purification, bio-hazard protection, portable power, or electric vehicles as electrodes for the capacitor. Occasionally, carbon nanotubes were considered as one type of fullerenes. Since the discovery of MWCNTs more than two decades ago, they have been widely used in many industrial applications such as conductive polymers, electromagnetic interference shielding composites, and electrostatic dissipation. MWCNTs are endowed with exceptional properties including high electrical conductivity (as conductive as copper), and high mechanical strength (up to 20 times stronger than steel). Moreover, they are light weight, flexible, thermally stable and chemically inert.[193] In this chapter, composites between HMS-based materials and the nano-inclusions were synthesized and their transport properties were studied with the aim of improving the thermoelectric performance of HMS-base materials.

4.2 Experimental section

Higher Manganese Silicide (HMS)-based composites were synthesized from the high purity elements purchased from Alfa Aesar as follows: Mn powder, 99.95%, −325 mesh; Si powder, crystalline, 99.9%, −100 mesh; Ge powder, 99.999%, −100 mesh; fullerene powder, mixed, typically 98% C_{60}, 2% C_{70}; and multi-walled carbon nanotube (MWCNT) powder, 6 to 9 nm in diameter and up to 5 μm long, >95% (carbon) from Sigma-Aldrich.

The theoretical density values of the composites, d_C, were formulated as $1/d_C = W_I/d_I + W_{HMS}/d_{HMS}$, where W_I and W_{HMS} are the mass fractions of nano-inclusions, i.e. C_{60} or MWCNTs and HMS-based material, respectively, d_I is the density of the nano-inclusions given by the manufacturer, i.e. 1.7 g/cm^3 for fullerenes, and 2.1 g/cm^3 for MWCNTs, and d_{HMS} is the density of HMS-based materials. The theoretical densities of $Mn_{15}Si_{26}$ and $MnSi_{1.75}$ was taken from the Inorganic Crystal Structure Database (ICSD – 15339 and ICSD – 183036, respectively), while the density of $MnSi_{1.75}Ge_{0.02}$ was calculated from that of $MnSi_{1.75}$ with the assumption that the addition of a small amount of Ge did not change significantly the unit cell of HMS.

It must be noted that all the C_p of $MnSi_{1.75}Ge_{0.02}$/MWCNTs composites were experimentally measured and they mostly fall below the Dulong-Petit values (Figure 4.1). Unfortunately, the second measurement resulted in a large difference compared to the first one due to the presence of side products in all samples. The Dulong-Petit specific heat, therefore, was used for the thermal conductivity calculations.

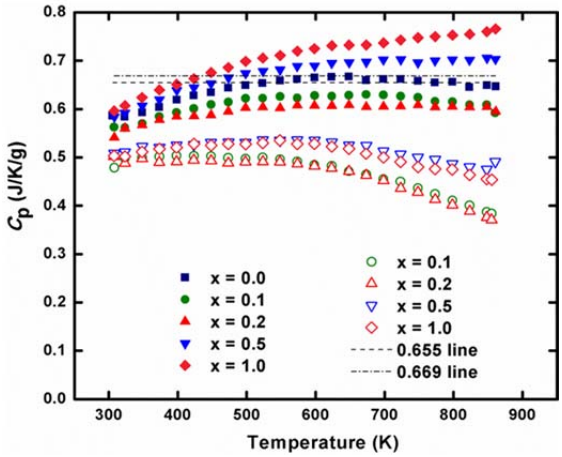

Figure 4.1 Temperature dependence of specific heat of the $MnSi_{1.75}Ge_{0.02}$/MWCNTs composites; the dashed dotted line represents the highest Dulong–Petit value (i.e. 0.669 $J \cdot K^{-1} \cdot g^{-1}$), and the dashed line represents the lowest Dulong–Petit value (i.e. 0.655 $J \cdot K^{-1} \cdot g^{-1}$), the filled and empty symbols imply the first and second measurement, respectively.

Two processes were used to prepare HMS-based composites, leading to different distributions of nano-inclusions inside the matrix materials. The part of results and discussions was thus divided into two subsections according to the preparation methods.

4.3 Results and discussions

4.3.1 Solid state reaction, manually mixing, and hot pressing

A large amount of the $Mn_{15}Si_{26}$ stoichiometry was prepared by solid state reaction as mentioned later in Chapter 6. The desired quantities of the $Mn_{15}Si_{26}$ compound and the nano-inclusions, i.e. C_{60} or MWCNTs, were manually blended together using agate mortar and pestle until fairly uniform mixtures were obtained. The mixtures were then hot pressed at 1000ºC for 60 minutes under a pressure of 54 MPa to achieve dense pellets for physical property measurements.

All the $C_{60}/Mn_{15}Si_{26}$ composites had experimental densities more than 94% of the theoretical densities, which was sufficient for subsequent thermoelectric property measurement (Table 4.1).

Table 4.1 Nominal C_{60} content, theoretical and experimental densities of the $C_{60}/Mn_{15}Si_{26}$ composites.

Nominal C_{60} content (wt.-%)	Theoretical density (g/cm^3)	Experimental density (g/cm^3)	Percentage (%)
0.0	5.17	5.08	98
0.1	5.16	4.95	96
0.5	5.12	4.86	95
1.0	5.07	4.82	95
2.0	4.97	4.67	94

The relative density decreased from 98% for the pure $Mn_{15}Si_{26}$ sample to 94% for the sample containing 2.0 wt.-% C_{60} due to increasing the amount of nano-inclusions, which required a re-optimization of the hot pressing parameters.

The elemental mapping using SEM-EDS exhibited uneven distributions of carbon in the matrix material (Figure 4.2) with the agglomerations as large as several tens of microns even at a fairly low C_{60} concentration of 0.5 wt.-%. The C_{60} inclusions were not only distributed at the grain boundaries, but also randomly dispersed inside the bulk samples. The observations showed that manually mixing was insufficient to homogenize the powder mixtures, especially for the fine inclusions at the nano-dimensions. Another reason was the high tendency to aggregate of C_{60} owing to the presence of large surface areas. Moreover, the hot pressing at high temperature for a long time period might enhance the aggregation of C_{60}. Furthermore, the silicon islands with various sizes ranging from several microns to a few tens of micrometers were non-uniformly allocated in the matrix material resulted from incomplete

solid state reaction. The overall elemental concentrations were quite comparable with the expected values considering a few atomic percents as errors for the EDS analyses.

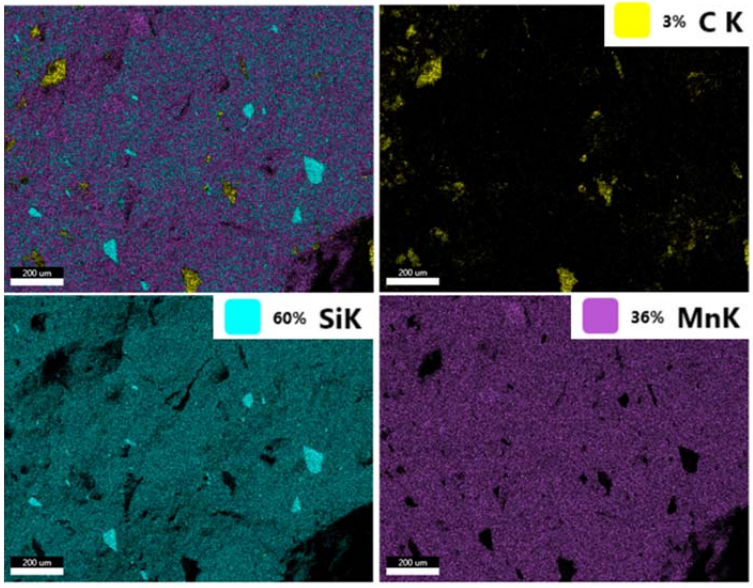

Figure 4.2 Elemental mapping of the $C_{60}/Mn_{15}Si_{26}$ composites with 0.5 wt.-% of C_{60}; the expected compositions are 1.5 at.-% of C, 62.5 at.-% of Si, and 36 at.-% of Mn.

The electrical resistivity of all the samples increased with elevating the temperature up to approximately 760 K due to enhanced acoustic phonon scattering at high temperature (Figure 4.3), then plateaued above this temperature. The Seebeck coefficient for all the composites also increased with increasing temperature, reaching the maximum value, ranging from 200 μV/K to 230 μV/K, at around 675 K, and slightly decreased at higher temperatures (Figure 4.3). The electrical resistivity of the $C_{60}/Mn_{15}Si_{26}$ composites increased with increasing the content of C_{60}, while the Seebeck coefficient was nearly identical for all the composites over the whole temperature range. For materials with parabolic band and energy-independent scattering approximation, the Seebeck coefficient is inversely proportional to the carrier concentration. Consequently, the carrier contents in the $C_{60}/Mn_{15}Si_{26}$ composites might be constant regardless of the C_{60} amounts or there existed no strong electronic

interactions between C_{60} and the matrix material. The increase in electrical resistivity was, therefore, caused by a reduction of the carrier mobility due to the presence of C_{60} agglomerations in the bulk samples, which scattered the charge carriers. Nevertheless, a measurement of carrier concentration and mobility was necessary to verify the explanations.

The thermal conductivity decreased with increasing temperature for all the samples, achieving the minimum value in the range of 2.70 $W \cdot m^{-1} \cdot K^{-1}$ to 2.75 $W \cdot m^{-1} \cdot K^{-1}$ at about 675 K, then increased again at higher temperature (Figure 4.3). Combining this with the observations of electrical resistivity and Seebeck coefficient, the bipolar diffusion in the $C_{60}/Mn_{15}Si_{26}$ composites was probably initiated from 675 K to 760 K, which limited the maximum operational temperature of these materials in this range. Surprisingly, the thermal conductivity of the composites with C_{60} was almost the same for all the compositions. As aforementioned in the introduction, the decrease in thermal conductivity was observed for the composites where the distribution of inclusions was more uniform in the matrix material. Therefore, it is assumed that the size of the dispersed inclusions was more important than their distribution in affecting the thermal conduction. The agglomerations of C_{60} were apparently too large to efficiently scatter the phonons, which would result in a decrease in thermal conductivity of $Mn_{15}Si_{26}$.

The figure of merit, *ZT*, increased with increasing the temperature, attaining the highest value at around 760 K for most of the samples with the exception of the material containing 0.5 wt.-% of C_{60}, which achieved the best performance at approximately 675 K (Figure 4.3). The bipolar diffusion in the composites with C_{60} was initiated in this temperature range, and might vary with the actual compositions, which thus decreased the thermoelectric performance at higher temperature for all the samples. The *ZT* of the composites decreased with increasing the C_{60} content due to the increase of electrical resistivity. The maximum *ZT* was reduced from 0.37 for the pure HMS to 0.29 for the composite containing 2.0 wt.-% of C_{60} at 760 K.

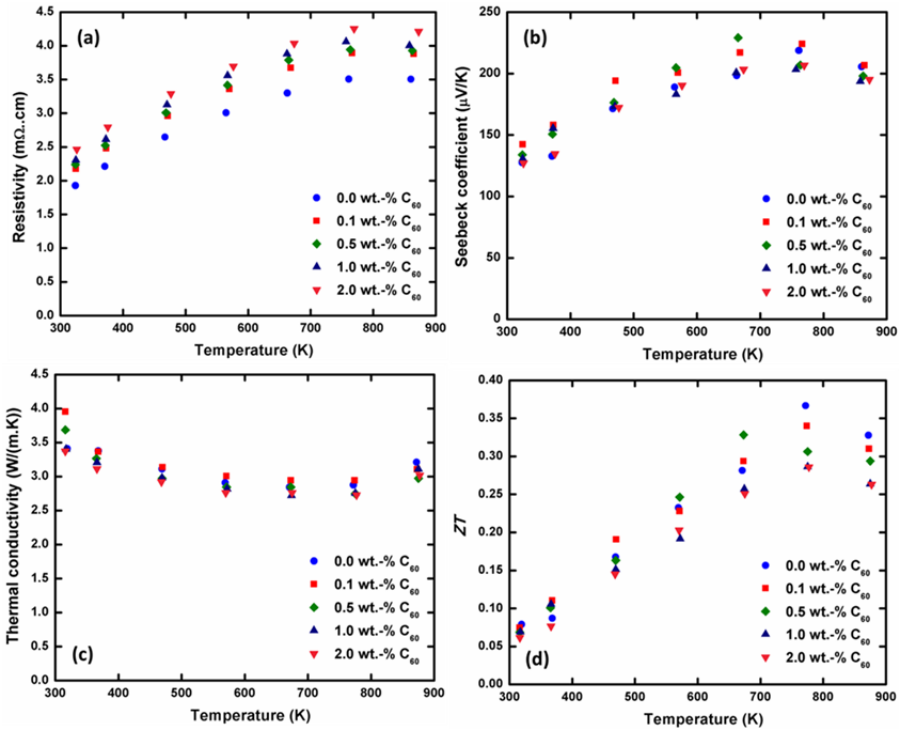

Figure 4.3 Temperature dependence of (a) electrical resistivity, (b) Seebeck coefficient, (c) thermal conductivity, and (d) *ZT* for the $C_{60}/Mn_{15}Si_{26}$ composites.

The introduction of C_{60} into the $Mn_{15}Si_{26}$ material increased the electrical resistivity and barely changed the Seebeck coefficient of the matrix. A constant carrier concentration with reduced carrier mobility due to enhanced charge carrier scattering with the C_{60} agglomerations was expected, requiring further measurements for verifying. The thermal conductivity was unaltered for all the composites with C_{60} due to the presence of large aggregations which ineffectively scattered the phonons. The *ZT* of the $C_{60}/Mn_{15}Si_{26}$ composites was, therefore, lowered owing to the increased electrical resistivity. A finer distribution of C_{60} in the HMS matrix was anticipated to promote the phonon scattering, which would reduce the thermal conductivity of the material.

All the MWCNT/$Mn_{15}Si_{26}$ composites prepared by manually mixing and hot pressing had experimental densities higher than 95% of the theoretical densities, which was satisfactory for subsequent physical property measurements (Table 4.2). The relative density

also slightly decreased from 98% to 95% for the sample containing 2.0 wt.-% of MWCNTs, which could be attributed to unoptimized pressing conditions with increasing the amount of nano-inclusions.

Table 4.2 Nominal MWCNTs content, theoretical and experimental densities of the MWCNTs/$Mn_{15}Si_{26}$ composites.

Nominal MWCNTs content (wt.-%)	Theoretical density (g/cm^3)	Experimental density (g/cm^3)	Percentage (%)
0.0	5.17	5.08	98
0.1	5.16	4.94	96
1.0	5.10	4.87	95
2.0	5.02	4.75	95

Similarly, the electrical resistivity of the MWCNTs/$Mn_{15}Si_{26}$ composites increased, while the Seebeck coefficient was almost consistent with increasing the MWCNTs content (Figure 4.4). This could also be explained by unchanged carrier concentration due to no electronic interaction between MWCNTs and the matrix material, and reduced carrier mobility due to enhanced charge carrier scattering. The bipolar diffusion was shown to initiate between 675 K and 775 K. Unfortunately the thermal conductivity of the composites increased with introducing the nano-inclusions. The reason might stem from the high thermal conductivity of MWCNTs, which was around 500 times higher than the HMS matrix. Similar agglomerations of the nano-inclusions were also observed in the C_{60}/$Mn_{15}Si_{26}$ composites, but insignificant changes existed in the total thermal conductivity due to the low thermal conduction of C_{60}, which was less than 0.5 $W \cdot m^{-1} \cdot K^{-1}$ at 300 K.

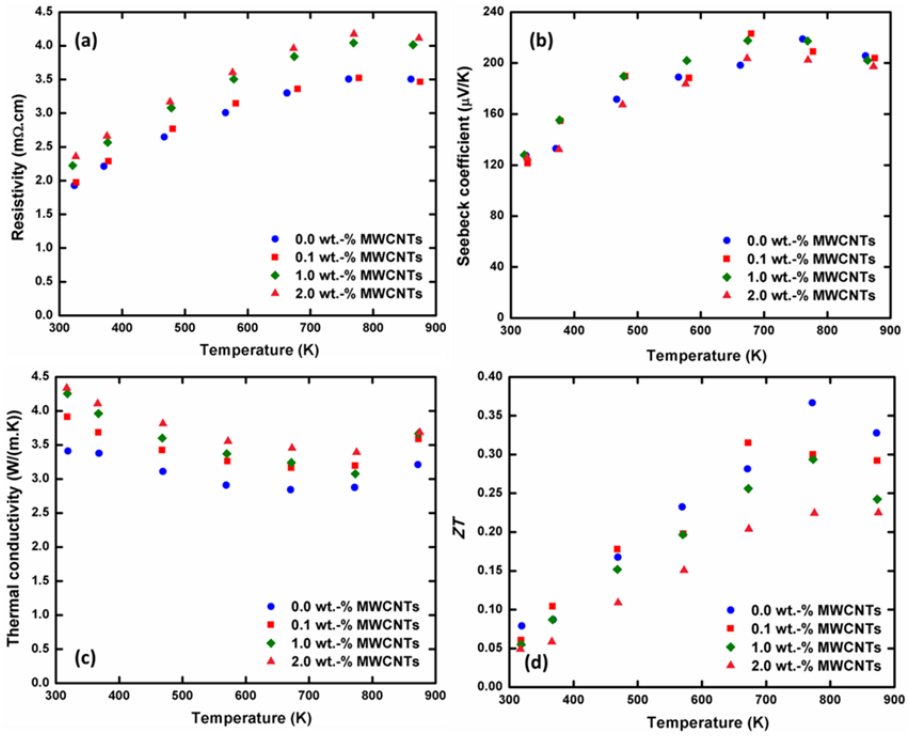

Figure 4.4 Temperature dependence of (a) electrical resistivity, (b) Seebeck coefficient, (c) thermal conductivity, and (d) *ZT* for the MWCNTs/$Mn_{15}Si_{26}$ composites.

As a result of increased electrical resistivity and thermal conductivity, the figure of merit was considerably reduced with the introduction of MWCNTs (Figure 4.4). The highest *ZT* values were mostly achieved at approximately 775 K except for the composite containing 0.1 wt.-% of MWCNTs, reaching the maximum *ZT* at about 675 K, which corresponded to the temperature range in which the initiation of bipolar diffusion probably occurred. A low *ZT* of approximately 0.22 was achieved at 775 K for the composite with 2.0 wt.-% of MWCNTs, which was around 40% lower than that of the pure $Mn_{15}Si_{26}$ material.

The MWCNTs/$Mn_{15}Si_{26}$ composites exhibited an increased electrical resistivity and fairly invariant Seebeck coefficient with increasing the content of nano-inclusions, which was similar to the composites with C_{60} prepared by the same procedure. However, the thermal conductivity of the samples containing MWCNTs increased considerably due to the high thermal conductivity of the inclusions. This led to significant reduction in

thermoelectric performance of the matrix materials by introducing MWCNTs. A homogeneous distribution of MWCNTs was also expected to create the phonon scattering centers in HMS-based materials, which would be the objective of the next section.

4.3.2 Mechanical milling and reactive spark plasma sintering

A simple and effective synthetic process was carried out involving two steps, namely: mechanical milling and spark plasma sintering (SPS). The stoichiometric amounts of the elements, e.g. $MnSi_{1.75}Ge_{0.02}$ + the MWCNTs, were blended via planetary ball milling using vials and balls made of tungsten carbide. Soft conditions were used with a ball-to-powder weight ratio of 3:1, i.e. 20 g of powders and seven balls with a diameter of 10 mm, a slow speed of 400 rpm, and a total duration of 20 minutes divided into two periods of rotation in reverse directions. The obtained homogeneous mixtures were directly loaded into a graphite die for SPS at 1050 °C in 45 minutes using a maximum pressure of 28 MPa. The sample containing 2.0 wt.-% of MWCNTs was synthesized later using the same method to investigate the effects of increasing amounts of MWCNTs loading..

The combination of ball milling and spark plasma sintering was used to prepare HMS and composites made of commercial MWCNTs and HMS matrix. A nominal formula of $MnSi_{1.75}Ge_{0.02}$ was chosen as addition of Ge has been reported to improve the thermoelectric properties of HMS. Moreover, a solubility limit of about 1.6% has been determined. Our choice of $MnSi_{1.75}Ge_{0.02}$ (that is 1.1% of Ge on the Si site, well below the solubility limit) was thus based on the reported improvement.[99] The rather gentle ball milling conditions utilized (400 rpm for 20 minutes) were sufficient to reduce the particle sizes of the elemental precursors but also assure their intimate mix. The same technique was previously used to prepare magnesium silicides (Mg_2Si), and it was proven that a short heating process either using microwave radiation,[194] regular resistance furnace[195] or spark plasma sintering[196] was enough to trigger and complete the reaction. Here, the intimately mixed, fine powders of the elemental precursors were directly subjected to a spark plasma sintering cycle, the resulting pucks had measured densities typically of at least 93% of the theoretical one. This process had evident advantages as it was fast and required a fairly low amount of energy, both

important parameters when considering the mass production of any materials. Pucks of up to 50 grams each have been prepared; however, in this study, 15 mm diameter pucks weighing approximately 2 grams were fabricated. In order to also insure the ideal mix of the MWCNTs and the (Mn, Si, Ge) powders, the MWCNTs were introduced in the milling jar and consequently, also subjected to the ball milling step.

The phase compositions were identified by P-XRD of the ground samples after the sintering process, all showing the major phase to be the desired HMS with traces of MnSi and Si. The introduction of carbon nanotubes did not bring any extra peaks on the X-ray powder pattern, even at the high content of 1.0 wt.-% (Figure 4.5).

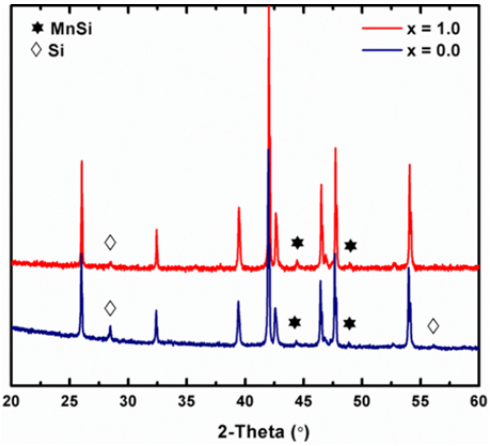

Figure 4.5 P-XRD patterns of the x wt.-% MWCNTs/$MnSi_{1.75}Ge_{0.02}$ composites prepared by mechanical milling and reactive spark plasma sintering.

The typical morphologies of MWCNT/HMS-based composites were shown in Figure 4.6 for the sample with 1.0 wt.-% MWCNTs. Micro pores and cracks were visible, similarly to what was reported by Chen *et al.*[150] Few impurities of elemental Si and MnSi phases were also seen as distinct islands with different sizes ranging up to several microns in the HMS matrix. The presence of these two phases was not surprising as it was well known that it was difficult to obtain HMS as single phase; moreover, the presence of MnSi was usually

detrimental to the thermoelectric performance as its metallic character contributed to a reduced Seebeck coefficient and an increased thermal conductivity.[108] Interestingly, it should be mentioned that there was no observation of carbon agglomerations for the samples with 0.1, 0.2, and 0.5 wt.-% MWCNTs; however, some carbon clusters became visible for the sample with 1.0 wt.-% MWCNTs as indicated in the same figure. The elemental mappings of the sample with 1.0 wt.-% MWCNTs were presented in Figure 4.6 for the four constituting elements Mn, Si, Ge, and C. Overall the sample was homogeneous and the MWCNTs, even at this high volume concentration, were distributed quite uniformly in the HMS matrix, again with the exception of some minor clusters.

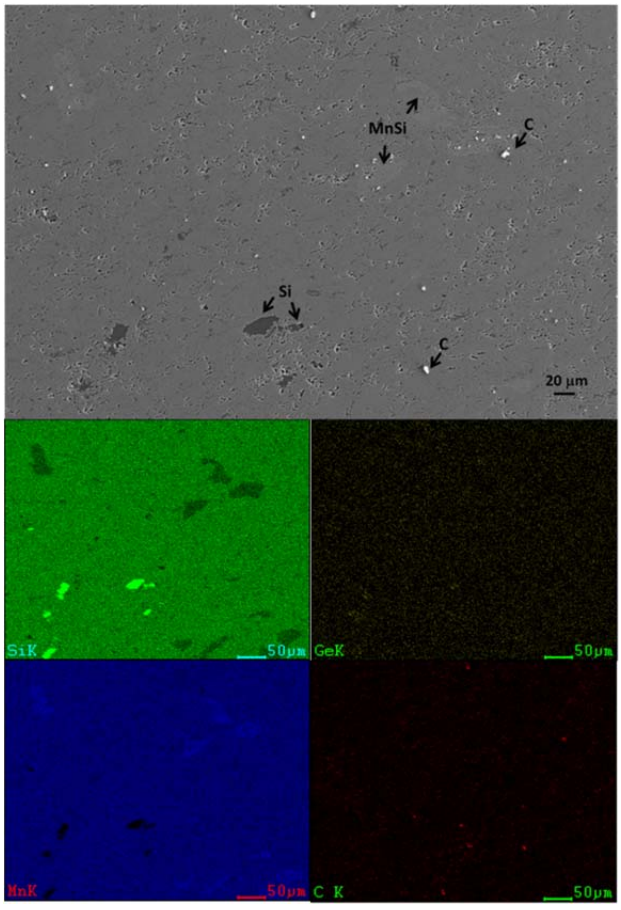

Figure 4.6 SEM image (top) and elemental mapping (bottom) of the MWCNTs/$MnSi_{1.75}Ge_{0.02}$ composite with 1.0 wt.-% MWCNTs.

The calculated densities of MWCNT/HMS-based composites are given in Table 4.3. The theoretical values, d_C, are also given in comparison, Unit cell determination via profile matching indicated a slight increase of the *a* parameter due to the insertion of Ge, changing from a = 5.5226(1) Å to a = 5.5267(4) Å for the materials without and with germanium substitutions, respectively. All the composites prepared had experimental densities higher than 93% of the theoretical one allowing us to proceed to the physical property measurements considering the error range of the density determinations. These results might even be underestimated as the SEM observations show very little residual porosity, typically less than 3%. In turn, this underestimation might come from the error inherent to the measurement of the density together with the actual calculation of the theoretical density. However, the sample containing 2.0 wt.-% of MWCNTs has achieved only 90% of the theoretical density, which could be explained by the high amount of nano-inclusions requiring different sintering conditions.

Table 4.3 Nominal MWCNT content, theoretical and experimental densities of the MWCNT/$MnSi_{1.75}Ge_{0.02}$ composites.

Nominal MWCNT content (wt.-%)	Theoretical density (g/cm^3)	Experimental density (g/cm^3)	Percentage (%)
0.0	5.22	4.96	95
0.1	5.21	4.93	95
0.2	5.20	4.94	95
0.5	5.18	4.90	95
1.0	5.14	4.79	93
2.0	5.07	4.57	90

Room temperature transport data are given in Table 4.4. They indicated that the carrier concentration was not modified by the addition of MWCNTs, which resulted in good

agreement with the quasi constant value of the Seebeck coefficient (estimated 15% and 5% errors are generally accepted for the measurements of carrier concentration and Seebeck coefficient, respectively). However, an increase of electrical resistivity was notable with the addition of MWCNTs, concomitant with a slightly decreasing mobility. Since this effect did not seem to come from any sort of doping that would have also affected the Seebeck coefficient, it could be reasonably postulated that the introduction of MWCNTs within the HMS matrix affects the microstructure in a way that disturbed the electron flow because of a greater grain boundary scattering. As the electrical conductivity of MWCNTs depends on their structure, it is possible that different results might be found depending on the source of MWCNTs used and whether or not they are more conducting than the HMS matrix. However, in this study, only microstructural effects could be evidenced. Evidently, if the addition of MWCNTs degraded the electronic transport, it also degraded the thermal transport as demonstrated by the evolution of the room temperature thermal diffusivity that drops from 1.28 mm^2s^{-1} in the MWCNT free sample to 0.91 mm^2s^{-1} in the 1.0 wt.-% sample, a rather impressive 30% decrease.

Table 4.4 Room temperature carrier concentration (n_p), mobility (μ_p), Seebeck coefficient (S), electrical resistivity (ρ) and thermal diffusivity (α) of the composites.

Nominal MWCNT content (wt.-%)	n_p (10^{21} cm^{-3})	μ_p ($cm^2 \cdot V^{-1}s^{-1}$)	S ($\mu V \cdot K^{-1}$)	ρ ($m\Omega \cdot cm$)	α ($mm^2 \cdot s^{-1}$)
0.0	2.19	1.71	127	1.66	1.28
0.1	2.81	1.33	123	1.65	1.19
0.2	2.27	1.57	119	1.74	1.06
0.5	2.15	1.54	119	1.87	0.95
1.0	3.00	1.05	124	1.96	0.91

The HMS being a promising thermoelectric material for medium range temperature applications (typically below 900 K), the transport properties of the prepared samples have

been measured up to 850 K. Figure 4.7 (a) and (b) show the evolution of the electrical resistivity and Seebeck coefficient with temperature, respectively. The bipolar diffusion was observed in the temperature range from 775 K to 820 K, which was higher than in the composites prepared by manually mixing and hot pressing, most probably due to different amounts of side products and the substitution of Ge at the Si sites, which altered the band structure. For all the samples, the Seebeck coefficient increased with temperature. However, if there were only slight differences at low temperature, the two samples, the richest in MWCNTs, had higher Seebeck coefficient than the other samples at high temperature, reaching a value of above 200 $\mu V \cdot K^{-1}$ and above 700 K. In parallel, these two samples had also the highest electrical resistivity as they both reached values higher than 3.5 $m\Omega \cdot cm$ above 800 K; the resulting power factor of all the samples was almost independent of the MWCNT content since the (slightly) increased Seebeck was compensated by the slightly increased electrical resistivity. An explanation of this behavior that could be hypothesized was a possible electron filtering effect at the grain boundaries, thus enhancing the Seebeck coefficient, coupled with reduced electrical conductivity due to the increased number of grain boundaries. The material with 2.0 wt.-% of MWCNTs exhibited a high electrical resistivity, which was more than 2 $m\Omega \cdot cm$ at room temperature and reached approximately 4 $m\Omega \cdot cm$ at around 815 K, which could be explained by not only the reduced carrier mobility due to enhanced scattering with MWCNTs but also its low density owing to the sintering conditions, which were needed to be optimized.

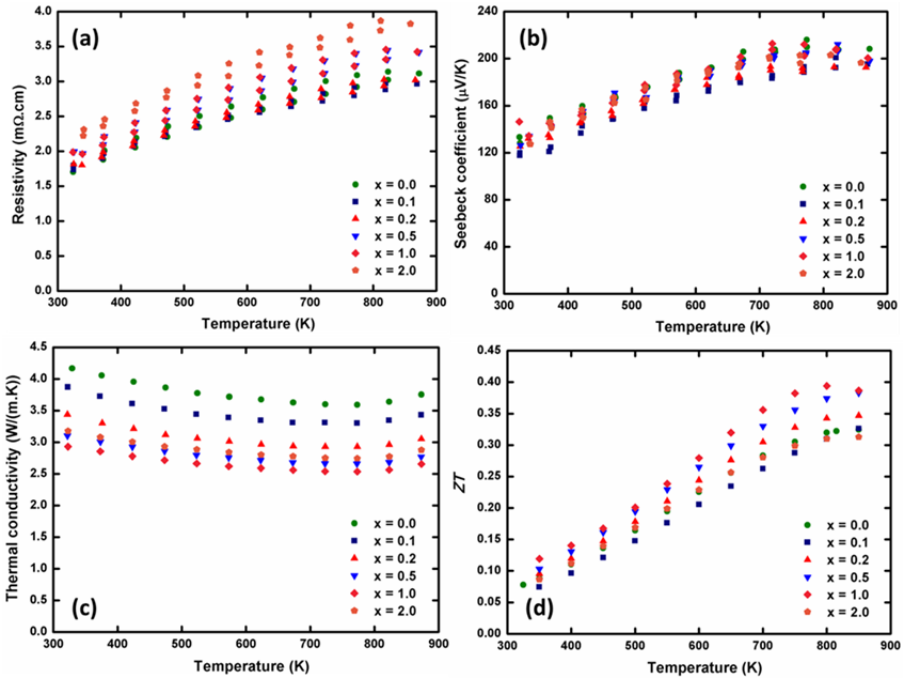

Figure 4.7 Temperature dependence of (a) electrical resistivity, (b) Seebeck coefficient, (c) thermal conductivity, and (d) *ZT* for the x wt.-% MWCNTs/$MnSi_{1.75}Ge_{0.02}$ composites.

What was more striking – and somewhat expected – was the effect of the addition of MWCNTs on the thermal transport properties. The thermal diffusivity of the different composites is shown in Figure 4.8. Clearly, while the thermal diffusivity for the composites prepared by manually mixing and hot pressing was either unaltered with the C_{60} nano-inclusions or increased with the MWCNTs additions, the thermal diffusivity here gradually decreased with increasing the MWCNTs content. Along the whole temperature range, the difference between the MWCNT-free compound and the 1.0 wt.-% MWCNT composite was about 30%. This notable reduction directly affected the variation of the thermal conductivity as shown in Figure 4.7. Furthermore, the composite containing 2.0 wt.-% MWCNTs presented a higher thermal diffusivity, leading to a higher total thermal conductivity, than the ones with 0.5 and 1.0 wt.-% of MWCNTs.

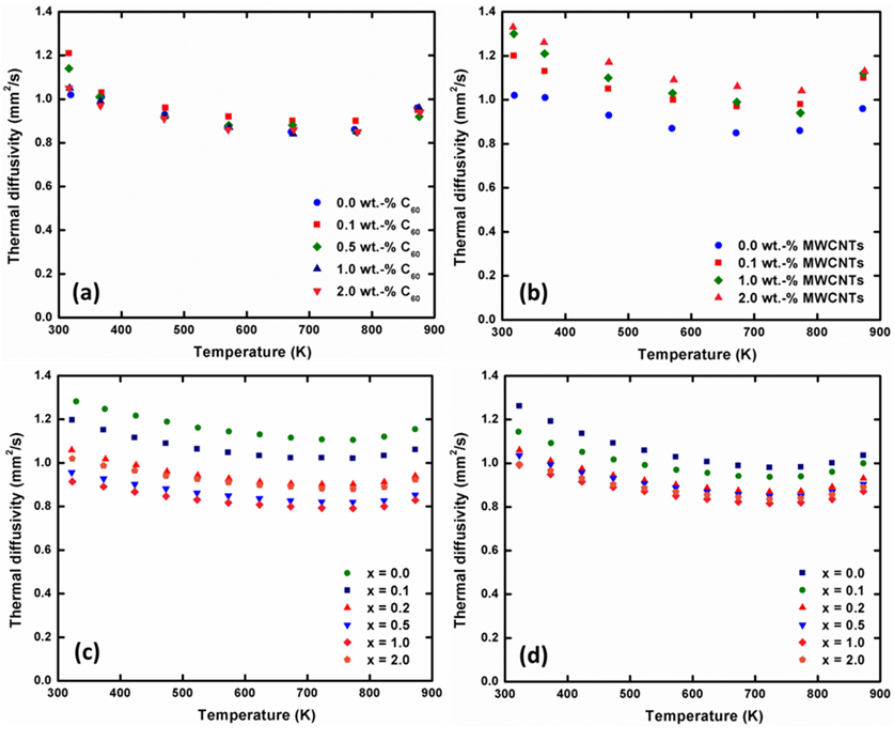

Figure 4.8 Temperature dependence of the thermal diffusivity for the different composites (a) $C_{60}/Mn_{15}Si_{26}$, (b) MWCNTs/$Mn_{15}Si_{26}$, (c) MWCNTs/$MnSi_{1.75}Ge_{0.02}$, and (d) MWCNTs/$MnSi_{1.75}$.

The addition of finely distributed MWCNTs, indeed, participated in the increase of the phonon scattering; this was also visible on the evolution of the lattice thermal conductivity (Figure 4.9) that could be extracted from the values of the total thermal conductivity and the electrical resistivity, for the sake of comparison, the electronic component of the thermal conductivity has also been plotted for each compound in the same figure.

It thus appears that the electronic component was nearly independent of the MWCNT content and that the thermal conductivity of the composites (and of HMS in general) was mainly driven by its lattice component, and that even with the addition of MWCNTs, it remained fairly high (above 2 $W \cdot m^{-1} \cdot K^{-1}$) but dropped dramatically compared to the MWCNT free sample. The material with 2.0 wt.-% of MWCNTs had higher lattice thermal

conductivity than the ones with 0.5 and 1.0 wt.-% of MWCNTs, which was the main contribution to the behavior of its total thermal conductivity. The reasons could be interpreted by the high content of MWCNTs, which possessed very high thermal conductivity and were possibly agglomerated into some clusters as implied from the mapping of the sample containing 1.0 wt.-% of MWCNTs.

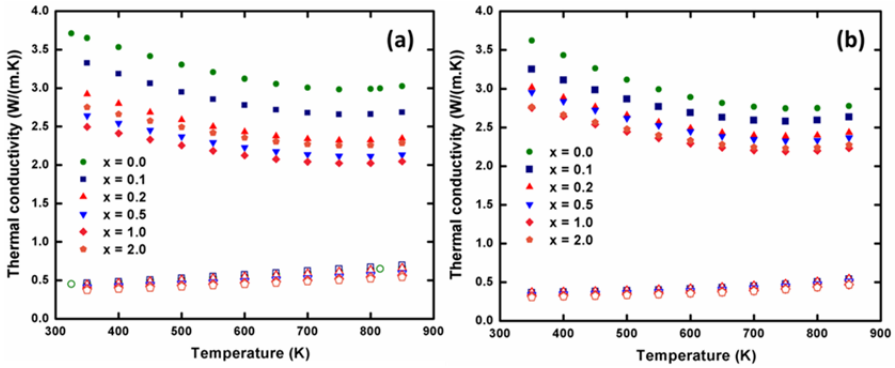

Figure 4.9 Temperature dependence of the electronic (empty markers) and phononic component (filled markers) of the thermal conductivity for the different composites (a) MWCNTs/$MnSi_{1.75}Ge_{0.02}$ and (b) MWCNTs/$MnSi_{1.75}$.

Similar composites between $MnSi_{1.75}$ and MWCNTs were prepared also using mechanical milling and spark plasma sintering to check the validity of our synthesis method and neglect the effect of germanium substitutions on the explanations. Very much comparable observations were achieved. Again, the experimental densities (Table 4.5) were achieved to attain more than 93% of the theoretical values with the exception of the sample containing 2.0 wt.-% of MWCNTs, which allowed us to continue on the physical property measurements.

Table 4.5 Nominal MWCNT content, theoretical and experimental densities of the MWCNT/$MnSi_{1.75}$ composites.

Nominal MWCNT content (wt.-%)	Theoretical density (g/cm^3)	Experimental density (g/cm^3)	Percentage (%)
0.0	5.15	4.92	96
0.1	5.14	4.92	96
0.2	5.14	4.95	96
0.5	5.11	4.88	95
1.0	5.08	4.72	93
2.0	5.00	4.57	91

The electrical resistivity of the MWCNTs/$MnSi_{1.75}$ composites exhibited a very slight decrease with introducing 0.1 and 0.2 wt.-% MWCNTs (Figure 4.10), which might stem from the experimental errors due to the small amount of the nano-inclusions, judged from very close experimental densities of these materials. The samples containing the higher contents of MWCNTs showed a small increase in electrical resistivity and Seebeck coefficient (Figure 4.10), which was resemble with the MWCNTs/$MnSi_{1.75}Ge_{0.02}$ composites. The bipolar initiation was recognized in the temperature from 725 K to 775 K.

The thermal diffusivity systematically decreased with increasing the MWCNTs amount (Figure 4.8), which resulted in similar trend for the total thermal conductivity of the composites (Figure 4.10). The lattice thermal conductivity was also the main contribution in the total thermal conductivity of the composites with $MnSi_{1.75}$ (Figure 4.9). For all the thermal terms, the thermal conduction of the sample with 2.0 wt.-% MWCNTs was nearly identical to that of the 1.0 wt.-% MWCNTs/$MnSi_{1.75}$ composite. However, the effect of introducing MWCNTs into $MnSi_{1.75}$ was a bit of less impressive with a reduction in thermal conductivity of approximately 20% over the whole temperature range for the sample containing 1.0 wt.-% of MWCNTs. The total thermal conduction of around 4.1 $W \cdot m^{-1} \cdot K^{-1}$ in

the MWCNTs free sample was reduced to about 3.1 $W \cdot m^{-1} \cdot K^{-1}$ in the material with 1.0 w.-% of MWCNTs at 325 K.

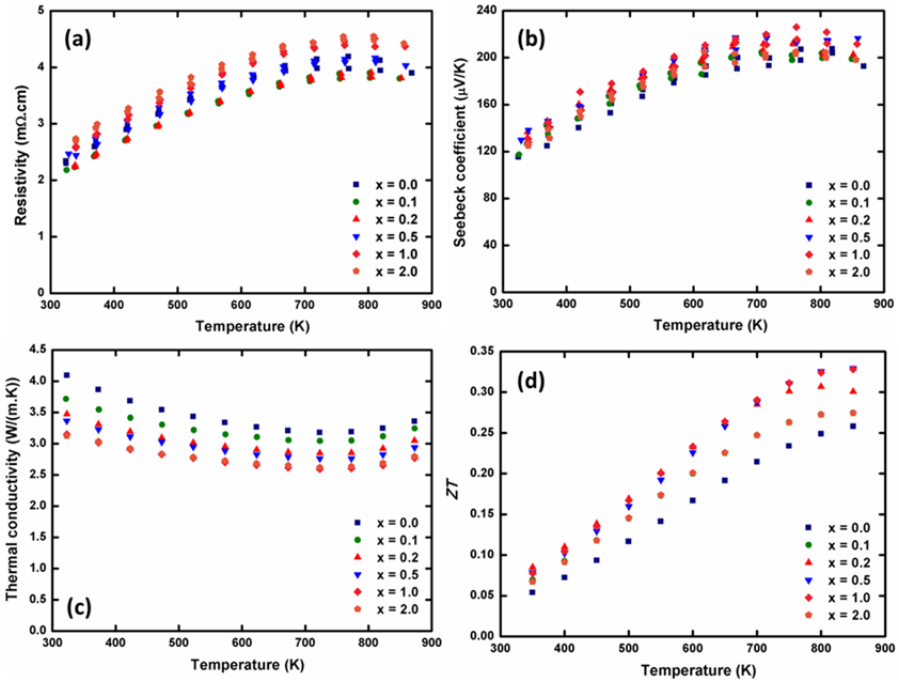

Figure 4.10 Temperature dependence of (a) electrical resistivity, (b) Seebeck coefficient, (c) thermal conductivity, and (d) *ZT* for the x wt.-% MWCNTs/$MnSi_{1.75}$ composites.

As a consequence of a nearly unchanged power factor, together with a decrease of total thermal conductivity, the thermoelectric figure of merit increased with the MWCNT content regardless of the matrix material, i.e. $MnSi_{1.75}Ge_{0.02}$ (Figure 4.8) or $MnSi_{1.75}$ (Figure 4.10). In this study, a *ZT* of 0.4 and 0.33 at 850 K was achieved for the 1.0 wt.-% MWCNTs/$MnSi_{1.75}Ge_{0.02}$ and $MnSi_{1.75}$ composites, respectively.

This value was relatively low but the – most likely – detrimental presence of MnSi metallic impurities, usually contributing to an increased thermal conductivity,[108] also hindered the thermoelectric properties. Efforts are underway to adjust the parameters of synthesis in order avoid the presence of MnSi and Si impurities.

4.4 Conclusions

To summarize, the composites between the nano-inclusions, i.e. C_{60} and MWCNTs and HMS-based materials, i.e. $Mn_{15}Si_{26}$, $MnSi_{1.75}Ge_{0.02}$, and $MnSi_{1.75}$ have been prepared using two different approaches.

The first approach combining solid state reaction, manually mixing, with hot pressing, produced the composites with inhomogeneous distributions of the inclusions. The C_{60} and MWCNTs aggregated into large agglomerations, which ineffectively scattered the phonons but sufficiently influenced the charge carrier mobility. Consequently, the electrical resistivity was considerably increased with increasing the amount of inclusions, while the thermal conductivity was either unchanged for the composites with C_{60} or increased for the composites with MWCNTs depending on the thermal conductivity of the inclusions. Significantly electronic interactions between the nano-inclusions and the matrix materials were not observed from the fairly unvarying Seebeck coefficient. As a result, the thermoelectric performance was greatly decreased with the additions of nano-inclusions, and a finer dispersion was anticipated to scatter phonons more effectively.

The second approach has shown to be simpler and more effective. Indeed, short ball milling time coupled with spark plasma sintering led to the fast fabrication of sizable samples. Using this simple method, MWCNTs were evenly dispersed within the HMS-based matrix. The addition of MWCNTs had a huge effect on reducing the thermal diffusivity of the composite material, while the electrical properties were not or much less affected by the introduction of this secondary phase. These observations were consistent for both $MnSi_{1.75}Ge_{0.02}$ and $MnSi_{1.75}$ materials.

To the best of our knowledge, this was the first attempt to introduce a carbon-based secondary phase into bulk HMS-based materials. The only other report concerning carbon addition was from Hou *et al.*[197] for polycrystalline HMS films prepared by magnetron sputtering, which was beyond the scope of this investigation. The preliminary results showed a promising improvement of figure of merit up to 20% with 1.0 wt.-% MWCNTs. However, further increase of the MWCNTs addition to 2.0 wt.-% strongly increased the electrical

resistivity with no more reduction of the thermal conductivity, which limited the best performance of HMS-based composites. We believed that the performance of these composites could be further enhanced by the optimization of the conditions of synthesis and processing, i.e. to eliminate the presence of the side products, and to prevent the agglomerations, including optimizing the concentrations of MWCNTs. Moreover, considering the numerous sorts of other carbon-based nano-allotropes that are commercially available, it is reasonable to assume that depending on the nature of the nano-inclusions used in the composites, thermoelectric properties of HMS-based materials could be much more improved.

Chapter 5

Different substitutions for enhancement of the thermoelectric performance of Higher Manganese Silicides-based materials[II]

Abstract

An easy and efficient process involving ball milling under soft conditions and spark plasma sintering was used to synthesize higher manganese silicides (HMS)-based materials, for example $MnSi_{1.75}Ge_{0.02}$, with different substitution, e.g. molybdenum, tungsten, or silver at the Mn sites, and germanium or aluminium at the Si sites. The XRD patterns of the samples after sintering showed the main phase to be HMS with the presence of some side products. The best thermoelectric efficiency was achieved for the phase mixture of the non-stoichiometric composition $MnSi_{1.75}Ge_{0.02}$ due to the absence of significant MnSi amount leading to a low electrical resistivity, which was then chosen to be the base material for further substitutions.

Molybdenum substitution enlarged the unit cell more than tungsten substitution, owing to its greater solubility in the HMS structure, whereas substitution with aluminium did not substantially alter the cell parameters. The electrical resistivity of HMS-based materials was reduced by <10% by this substitution, because of increased carrier concentrations. Changes of the Seebeck coefficient were insignificant after molybdenum and aluminium substitution whereas tungsten substitution slightly reduced the thermopower of the base

[II] Springer and Journal of Electronic Materials, 44, 2015, 3603 - 3611, Molybdenum, Tungsten, and Aluminium Substitution for Enhancement of the Thermoelectric Performance of Higher Manganese Silicides, D. Y. N. Truong, D. Berthebaud, F. Gascoin, H. Kleinke, original copyright notice is given to the publication in which the material was originally published, by adding: with kind permission from Springer Science and Business Media.

Part of this chapter is reprinted from http://dx.doi.org/10.1007/s11664-015-3854-x with kind permission from Springer Science and Business Media.

material by approximately 8% over the whole temperature range; this was ascribed to reduced carrier mobility as a result of enhanced scattering. Substitution with any combination of two of these elements resulted in no crucial modification of the electrical properties of the base material. Large decreases of lattice thermal conductivity were observed, because of enhanced phonon scattering, with the highest reduction up to 25% for molybdenum substitution; this resulted in a 20% decrease of total thermal conductivity, which contributed to improvement of the figure of merit *ZT* of the HMS-based materials. The maximum *ZT* value was approximately 0.40 for the material with 2 at.-% molybdenum substitution at the Mn sites.

Moreover, the low solubility of Ag in the HMS-based materials was indicated from the peaks of elemental Ag in the powder diagrams at low substituent contents. Small concentration of Ag substitution was found to reduce the thermal conductivity of $MnSi_{1.75}Ge_{0.02}$, resulting in slightly enhanced thermoelectric performance.

5.1 Introduction

A variety of work has been conducted on tuning the transport properties of HMS by substitution or doping,[99,108,109,111,112,127–129,143,150,198] composite formation,[115,199,200] and nanostructuring.[103,144] For substitution at Si sites, the highest *ZT* values obtained were 0.6 at 833 K and 0.65 at 850 K for Ge and Al-doped polycrystalline HMS, respectively.[99,129] Material containing 3 at.-% and 5 at.-% chromium substitution at Mn sites was reported to reach the highest *ZT* of approximately 0.6 at 850 K.[198] Recently, multiple simultaneous substitutions of HMS systems have attracted renewed interest. A superior *ZT* of approximately 0.65 at approximately 875 K was achieved by complex doping of HMS with aluminium, germanium, and molybdenum, although the experimental procedure was not detailed.[112] Simultaneous substitutions with Cr and Ru at Mn sites were investigated by Ponnambalam *et al.*[198], and a *ZT* of 0.5 at 850 K was achieved for the composition $Mn_{0.65}Cr_{0.20}Ru_{0.15}Si_{1.74}$. Chen *et al.*[150] have studied in detail the effects of Al and Ge doping at Si sites on the thermoelectric properties of HMS, and achieved a maximum *ZT* of 0.57 at 823 K. This motivated us to investigate multiple substitutions of HMS-based materials.

In this chapter, we report the thermoelectric properties of various HMS-based materials, including the ones containing different Ge concentrations, $MnSi_{1.75}Ge_{0.02}$ with aluminium substitution at Si sites and molybdenum, tungsten, or silver substitution at Mn sites. The simple and effective process used for synthesis entailed mixing of the component elements by ball milling under soft conditions, and spark plasma sintering of the powder mixtures obtained.

Improvement of thermoelectric performance by doping with different amounts of Ge was widely reported by several groups;[99,108,109,112,150] the Ge contents were well below the experimentally determined solubility limit of approximately 1.0 at.%.[99] Moreover, the Si-rich compositions, i.e. $MnSi_{1.80}$,[100,111,129,137] $MnSi_{1.84}$,[44] $MnSi_{1.85}$,[123,125] and $MnSi_{1.91}$,[126] have shown better thermoelectric performance than the stoichiometric materials, where the extra silicon played the role of an insulator. Here, the possibly excess germanium with a smaller bandgap, i.e. approximately 0.7 eV, than that of Si, i.e. around 1.1 eV, which is comparable to that of the HMS materials, was expected to have insignificant effects on the electronic structures of the matrix materials. A nominal composition of $MnSi_{1.75}Ge_{0.02}$, corresponding to 0.7 at.-% Ge, exhibited the best properties in this work, which was then chosen as the base material for further substitution with Al, Mo, W, and Ag. Similar to chromium substitution,[109,111,127,128,143,198] molybdenum and tungsten, which belong to the same group as chromium in the periodic table, were expected to have similar electronic effects on HMS-based materials, and possibly reduce the lattice thermal conductivity by creating large mass fluctuations and lattice distortion owing to their size differences compared with the matrix element Mn.

Recently, silver nanoparticles (Ag NPs) has gained considerable attentions because of their unique physical, chemical and biological properties, e.g. superior electrical conductivity, high stability, morphologically dependent properties, surface plasmon resonance effect, and strong bacterial resistance, which are much different to their bulk counterparts.[201] Ag NPs have been extensively used to enhance thermoelectric performance of different materials, e.g. Ba-filled skutterudites,[202] Bi_2Te_3,[203] and polyaniline.[204] In order to initiate the investigations on incorporating Ag NPs into HMS-based materials, the doping

effects of silver were first studied with various Ag concentrations. Even though the atomic radius of manganese and silver, 1.61 Å and 1.65 Å, respectively, are quite similar, the covalent sizes are much disparate, 1.39 Å and 1.53 Å, respectively. Therefore, possible silver substitutions were anticipated to create large structural deformations and influence the band structure of HMS-based material.

5.2 Experimental section

Desired amounts of the constituent elements (Mn powder, 99.95%, -325 mesh; Si powder, crystalline, 99.9%, -100 mesh; W powder, 99.9%, -325 mesh; Mo powder, 99.95%, APS 3–7 micron; Al powder, 99.8%, -40 + 325 mesh; Ge powder, 99.999%, -100 mesh; Ag nanopowder, APS 20-40 nm, 99.9%; all purchased from Alfa Aesar) were mixed in planetary ball milling by use of vials and balls made of tungsten carbide. Soft conditions were used; the ball-to-powder weight ratio was 3:1, the rotation speed was 400 rpm, and the total duration of 20 minutes was divided into two periods in the opposite directions. Homogeneous mixtures of the elements were directly loaded into a graphite die for spark plasma sintering (SPS) at 1050ºC under a pressure of 28 MPa for a duration of 45 min.

The densities of all the pellets were > 94% of the theoretical densities, which enabled us to proceed to the next step of physical property measurement. The density of a phase mixture can be calculated by use of the formula $1/d = \Sigma W_i/d_i$, where W_i and d_i are, respectively, the mass fraction and density of the components. Consequently, the theoretical densities of HMS-based materials could be estimated from the densities and compositions of the phase mixtures and the side products, including Si: 2.33 g/cm^3; MnSi: 5.83 g/cm^3; $MoSi_2$: 6.27 g/cm^3; WSi_2: 9.85 g/cm^3 (all taken from the Inorganic Crystal Structure Database). Because estimating small amounts of the identified side products led to slightly lower theoretical densities in each case, the comparison given in Table 5.1 and

Table 5.2 represents the lower limit of the theoretical density.

Table 5.1 Nominal compositions and Ge content, and theoretical and experimental densities of HMS-based materials containing different Ge amounts.

Nominal compositions	Nominal Ge content (at.-%)	Theoretical density (g/cm^3)	Experimental density (g/cm^3)	Percentage (%)
$MnSi_{1.75}$	0.0	5.15	4.92	96
$MnSi_{1.75}Ge_{0.02}$	0.7	5.25	4.96	94
$MnSi_{1.75}Ge_{0.05}$	1.8	5.33	5.09	95
$MnSi_{1.73}Ge_{0.02}$	0.7	5.19	4.90	94
$MnSi_{1.70}Ge_{0.05}$	1.8	5.26	4.92	94

Table 5.2 Theoretical and experimental densities of HMS-based materials assuming phase purity.

Nominal compositions	Theoretical density (g/cm^3)	Experimental density (g/cm^3)	Percentage (%)
$MnSi_{1.75}Ge_{0.02}$	5.25	4.96	94
$Mn_{0.98}Mo_{0.02}Si_{1.75}Ge_{0.02}$	5.29	5.01	95
$Mn_{0.98}W_{0.02}Si_{1.75}Ge_{0.02}$	5.38	5.08	94
$MnSi_{1.73}Al_{0.02}Ge_{0.02}$	5.25	4.98	95
$Mn_{0.96}Mo_{0.02}W_{0.02}Si_{1.75}Ge_{0.02}$	5.41	5.12	95
$Mn_{0.98}Mo_{0.02}Si_{1.73}Al_{0.02}Ge_{0.02}$	5.29	4.99	94
$Mn_{0.98}W_{0.02}Si_{1.73}Al_{0.02}Ge_{0.02}$	5.38	5.12	95

5.3 Results and discussions

The combination of ball milling under soft conditions and spark plasma sintering was a practical process for synthesis of HMS-based materials.[200] The process was rather atypical compared with conventional methods for preparing HMS, e. g. melting techniques and

mechanical alloying, but was very simple and efficient. The process consisted of two steps and took less than two hours to produce materials in which HMS were the major phases. The dense pellets obtained after the second step were ready for measurement of physical properties or preparation of thermoelectric modules. Moreover, energy consumption and production costs can be reduced sufficiently to make the method very promising for HMS mass production in industry.

5.3.1 Effects of Ge concentrations

Different Ge contents have been introduced into the $MnSi_{1.75}$ material including the stoichiometric and non-stoichiometric compositions (Table 5.1). The nominal Ge content was calculated over the total atomic sites assuming that Si and Ge atoms occupied the same positions. The theoretical densities were estimated from the assumption of constant unit cell volumes due to small amounts of Ge substitutions. Overall, the experimental densities of more than 94% compared to the theoretical values were sufficient for the subsequent physical property measurements.

The XRD patterns revealed the main phase to be HMS with the side products of MnSi and Si (Figure 5.1). Interestingly, the peaks of MnSi were not clearly observed for the non-stoichiometric compositions of $MnSi_{1.75}Ge_{0.02}$, but very obvious for the stoichiometric $MnSi_{1.73}Ge_{0.02}$ even though the Ge content was almost identical in these two materials. It was concluded that a small amount of excess Ge helped to complete the reaction between MnSi and Si to form HMS phases. The relative peak intensities indicated an increase of MnSi phase content in the $MnSi_{1.73}Ge_{0.02}$ sample compared to the pure $MnSi_{1.75}$ where the Ge concentration was still below the solubility limit, which was in agreement with previous work.[104,108] Moreover, large MnSi contents were recognized in both the $MnSi_{1.75}Ge_{0.05}$ and $MnSi_{1.70}Ge_{0.05}$ compositions, where the Ge content was much higher than the reported solubility of Ge in HMS. The reappearance of MnSi striations beyond the solubility limit of Ge has been previously noticed, which was explained by the formation of Si_xGe_{1-x} alloys.[99] Here, the Si_xGe_{1-x} phase was not detected within the detection limits of XRD. The presence

of the metallic MnSi phase is undesirable, which usually degraded the thermoelectric performance of HMS-based materials.

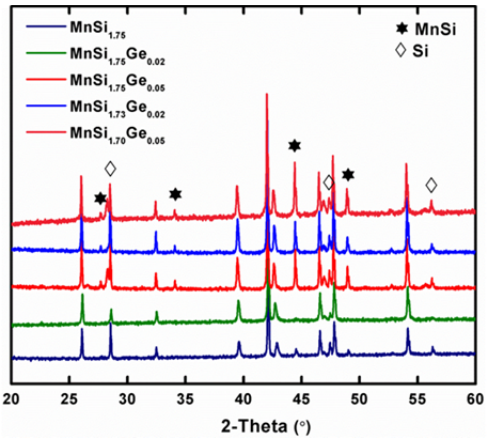

Figure 5.1 XRD patterns of HMS-based materials containing different Ge amounts.

The electrical resistivity of the Ge containing samples was significantly lower than that of the pure $MnSi_{1.75}$ material with an exception of the phase mixture of the nominal $MnSi_{1.75}Ge_{0.05}$ composition, while the Seebeck coefficient was slightly reduced except for the $MnSi_{1.75}Ge_{0.02}$ composition (Figure 5.2). As aforementioned, the MnSi contents increased in most of the materials containing Ge, which led to an increase of carrier concentration decreasing the Seebeck coefficient and the electrical resistivity of the stoichiometric material. Exceptionally, the slight increase of the electrical resistivity in the $MnSi_{1.75}Ge_{0.05}$ sample might stem from the reduced mobility due to the formation of defects scattering the charge carriers. On the other hand, a very small amount of extra Ge substitutions enhanced the completion of the reaction of MnSi with Si in the $MnSi_{1.75}Ge_{0.02}$ sample, and the carrier density was thus nearly unchanged. The decreased electrical resistivity in comparison to the base material, therefore, was explained by an increased mobility owning to the lower amount of side products creating grain boundaries to scatter the charge carriers. The bipolar diffusion was initiated in the temperature range from 775 K to 815 K for all the samples.

Surprisingly, the thermal conductivity of all the Ge containing materials was higher than that of the pure $MnSi_{1.75}$, which was opposite to our expectations (Figure 5.2). This was anticipated to arise from the sizes and distributions of the side products rather than their nature and amount, which strongly affected the phonon scattering. The non-stoichiometric $MnSi_{1.75}Ge_{0.05}$ material showed the highest thermal conductivity, reaching 5 $W \cdot m^{-1} \cdot K^{-1}$ at approximately 325 K. The $MnSi_{1.73}Ge_{0.02}$ exhibited a slightly higher thermal conduction than the other two of Ge-containing materials, where the differences decreased and disappeared with increasing the temperature. Again, a morphological study needed to be done to fully understand the thermal conduction in these materials.

As a result of its high electrical resistivity and thermal conductivity and low Seebeck coefficient, the phase mixture of the nominal $MnSi_{1.75}Ge_{0.05}$ composition showed the lowest *ZT* with the maximum value of only 0.15 at around 850 K (Figure 5.2). The stoichiometric materials exhibited comparable performance to the base sample owing to the decreased electrical resistivity, which compensated for the slightly decreased Seebeck coefficient and the increased thermal conductivity. The best performance was found in the $MnSi_{1.75}Ge_{0.02}$ compositions as a consequence of its lowest electrical resistivity, achieving a highest *ZT* of 0.32 at 815 K, which was then used as the base material for subsequent substitutions.

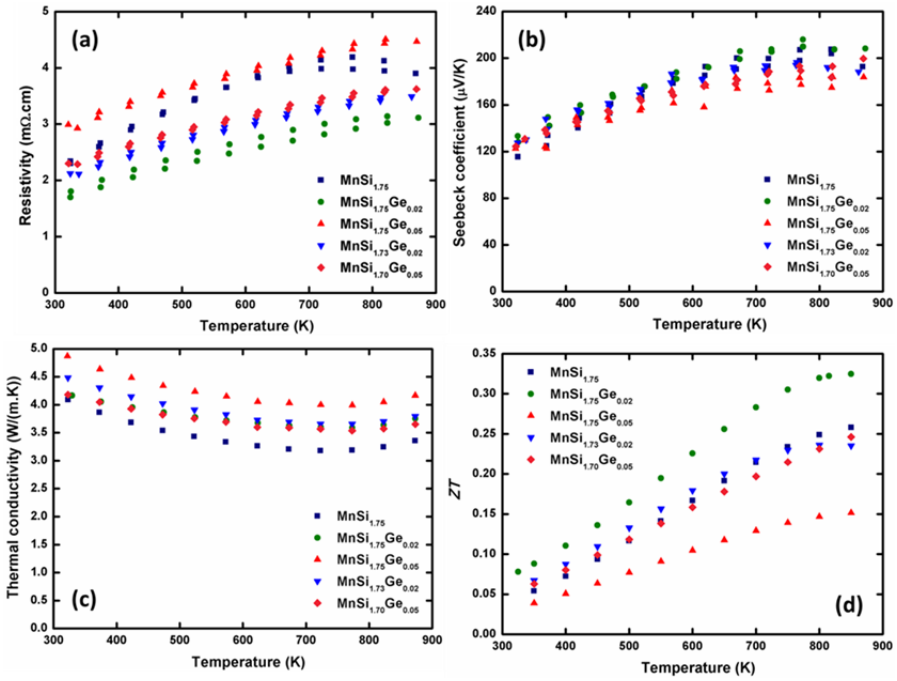

Figure 5.2 Temperature dependence of (a) electrical resistivity, (b) Seebeck coefficient, (c) thermal conductivity, and (d) *ZT* in the HMS-based materials containing different Ge amounts.

5.3.2 Effects of Mo, W, and Al substitutions

The P-XRD patterns of all the samples showed that HMS is the main phase (unlabelled peaks in Figure 5.3) with some side products, for example MnSi, silicon, and disilicides ($MoSi_2$, WSi_2). The duration of the reaction inside the SPS was kept short because a rather well-mixed powder was used as the starting material and grain growth must be avoided. However, this led to incomplete solid-state reactions owing to the low rate of diffusion of silicon and somewhat large particle sizes of the reactants. Further optimization of milling and sintering conditions are in the progress to synthesize pure HMS materials; this is expected to make the method comparable with conventional synthetic techniques. When manganese was substituted by 2 at.-% of molybdenum or tungsten, extra peaks appeared in the patterns; these were ascribed to the disilicide phases, i. e. $MoSi_2$ and WSi_2.

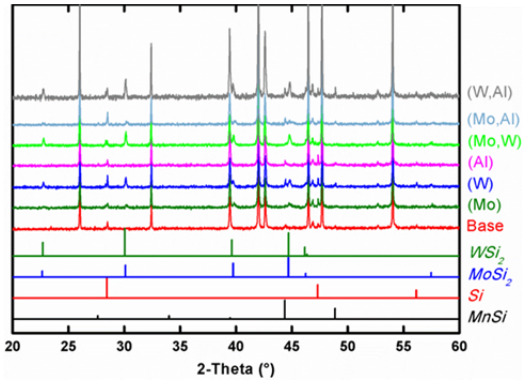

Figure 5.3 P-XRD patterns of HMS-based materials after sintering. Unidentified peaks belong to HMS phases; the reference patterns of the side products are given at the bottom with the names written in italic letters.

As being mentioned in Chapter 2, the HMS include compounds with several different formulas; these have very similar *a*, but quite different *c* lattice parameters. Because of their close structural similarities, their XRD patterns are very similar in both peak positions and intensities. For this reason, a specific compound was rarely identified, but the general name HMS was usually given in most reports.[103,150] Considering *n* Mn and *m* Si tetragonal sublattices stacking along the *c*-axis to form an HMS compound, the lattice parameters of the supercell are calculated as $a = a_{Mn}$ ($\geq a_{Si}$) and $c = n \times c_{Mn} = m \times c_{Si}$, where a_{Mn}, a_{Si}, c_{Mn}, and c_{Si} are the subcell parameters. In this work, the Le Bail refinement with FullProf software was used to fit the experimental patterns with the corresponding peaks of the two sublattices.[205] The c_{Mn}/c_{Si} ratio was then calculated from the refined parameters, and used to predict the formulae as $(Mn, Mo, W)_{11}(Al, Si, Ge)_{19}$ because the typical value of $c_{Mn}/c_{Si} \approx 1.728$. The *a* and *c* parameters of the two sublattices, with the corresponding ratios, are presented in Table 5.3.

Table 5.3 Le Bail-refined parameters for Mn and Si sublattices of HMS-based materials.

Nominal compositions	a_{Mn} (Å)	c_{Mn} (Å)	a_{Si} (Å)	c_{Si} (Å)	c_{Mn}/c_{Si}
$MnSi_{1.75}Ge_{0.02}$	5.5256(2)	4.3682(2)	3.9074(2)	2.5268(2)	1.7287(2)
$Mn_{0.98}Mo_{0.02}Si_{1.75}Ge_{0.02}$	5.5263(2)	4.3692(2)	3.9078(2)	2.5278(2)	1.7284(2)
$Mn_{0.98}W_{0.02}Si_{1.75}Ge_{0.02}$	5.5263(2)	4.3686(2)	3.9076(2)	2.5272(2)	1.7286(2)
$MnSi_{1.73}Al_{0.02}Ge_{0.02}$	5.5260(1)	4.3684(1)	3.9076(2)	2.5268(2)	1.7288(1)
$Mn_{0.96}Mo_{0.02}W_{0.02}Si_{1.75}Ge_{0.02}$	5.5276(2)	4.3702(2)	3.9089(2)	2.5286(2)	1.7283(2)
$Mn_{0.98}Mo_{0.02}Si_{1.73}Al_{0.02}Ge_{0.02}$	5.5264(2)	4.3689(2)	3.9080(2)	2.5278(2)	1.7283(2)
$Mn_{0.98}W_{0.02}Si_{1.73}Al_{0.02}Ge_{0.02}$	5.5254(2)	4.3680(2)	3.9072(2)	2.5275(2)	1.7282(2)

The results showed that the sublattices are slightly enlarged by partial substitution of Mn with Mo and W. Mo resulted in larger cell parameters than W, even though these two elements have nearly identical covalent radius (r_{Mo} = 1.45 Å, r_W = 1.46 Å); this implied that more Mo was incorporated at the Mn sites. This assumption was in agreement with a larger amount of WSi_2 detected by P-XRD compared with $MoSi_2$, judging from the peak intensities. The *c* axis of the Si sublattice was expanded from 2.527 Å to 2.528 Å with only 2 at.-% molybdenum substitution at the Mn sites. The combination of Mo and W substitution, however, increased the lattice parameters substantially compared with only Mo or W substitution, which indicated that more Mo and W could be intercalated when both elements were present. However, it should be mentioned that the high background of the patterns, because of the presence of manganese, might lead to additional errors in the analysis and refinement results.

Furthermore, substitution of Si sites with Al atoms did not result in additional peaks in the XRD pattern of the base material. To the best of our knowledge, this was the largest amount of Al substitution of HMS (approximately 1.1 at.-% at Si sites), reported so

far.[112,129,150] The presence of Al resulted in an insignificant modification of the lattice parameters because of the similar sizes of Al and Si atoms (r_{Al} = 1.18 Å, r_{Si} = 1.11 Å). Therefore, the cell modification as a result of double substitution, where one of the substituent atoms is Al, mainly depended on the other element. As an example, the sample with Mo and Al substitution had lattice parameters almost identical with those of the Mo-substituted one. However, the material substituted with W and Al had slightly smaller lattice parameters, except for c_{Si}, than those of the W and Al-substituted materials, because tungsten substitution was less favorable, i.e. the amount of tungsten in the HMS structure was probably less than the amount of molybdenum. The exceptional modification of c_{Si} could be explained by the ease of modulation of the structure along this axis, which has been reported to result in different structural formulas of HMS.[81]

Typical morphology of these samples is presented in Figure 5.4. Micro pores and cracks were apparent on the surfaces after polishing, and were responsible for porosity of less than 6%. Examples of HMS grains were circled and indicated by arrows in Figure 5.4 (a) with the sizes varying up to several tens of microns, which were quite similar to the particle sizes of the starting elements, with no significant agglomeration as a result of short sintering times. The disilicide phases appeared as distinct islands in the HMS matrix, as is apparent from Figure 5.4 (b) and (c) for the Mo and W-substituted samples, respectively. These islands were of different sizes, including areas of approximately several ten microns and smaller ones, and were randomly distributed throughout the matrix. However, the WSi_2 grains were significantly segregated into large areas of up to more than 50 μm in length. The morphology of the Al-substituted sample in Figure 5.4 (d) was nearly identical with that of the base material. A uniform blend of dopants in the HMS matrix was not achieved for this sample because of the small amounts of dopants and the soft milling conditions. The effect of the morphology of side products on the thermoelectric performance of HMS-based materials has been reported for the products containing MnSi with different sizes and distributions.[117,118] As a consequence, smaller sizes and more even distribution of $MoSi_2$ and WSi_2 were expected to have different effects on the thermoelectric performance of HMS, which might be an interesting topic for further studies.

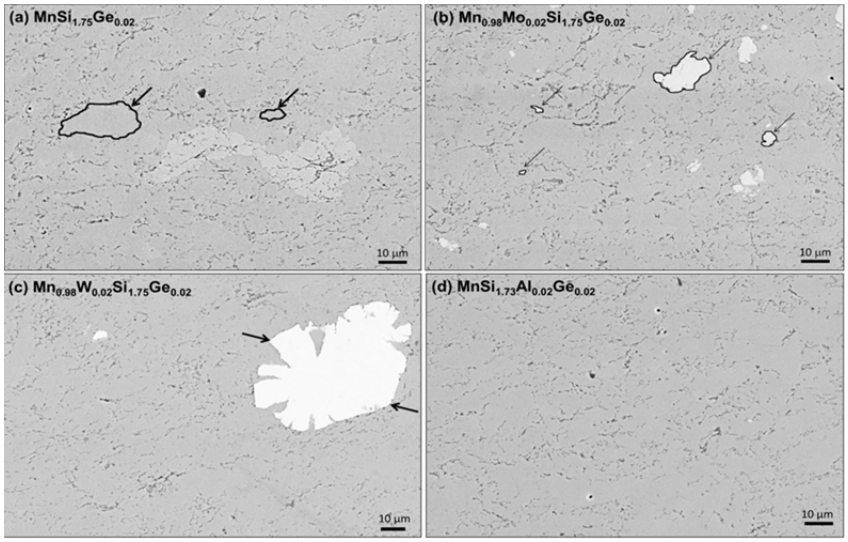

Figure 5.4 SEM images of (a) $MnSi_{1.75}Ge_{0.02}$ with HMS grains highlighted, (b) $Mn_{0.98}Mo_{0.02}Si_{1.75}Ge_{0.02}$ with $MoSi_2$ grains highlighted, (c) $Mo_{0.98}W_{0.02}Si_{1.75}Ge_{0.02}$ with a > 50 μm grain, and (d) $MnSi_{1.73}Al_{0.02}Ge_{0.02}$.

The electrical resistivity and Seebeck coefficient were measured during two heating and cooling cycles to ensure consistency of the data (Figure 5.5). For the same reason, measurement of thermal diffusivity was also performed three times at each temperature, and the average values were used to calculate the thermal conductivity. The same trends were observed for all the samples over the whole temperature range from 300 to 900 K. The electrical properties were highly reproducible during the two measurement cycles, taking into consideration estimated errors of 3% and 5% for the Seebeck coefficient and electrical resistivity, respectively, and the three thermal diffusivity measurements were also replicated.

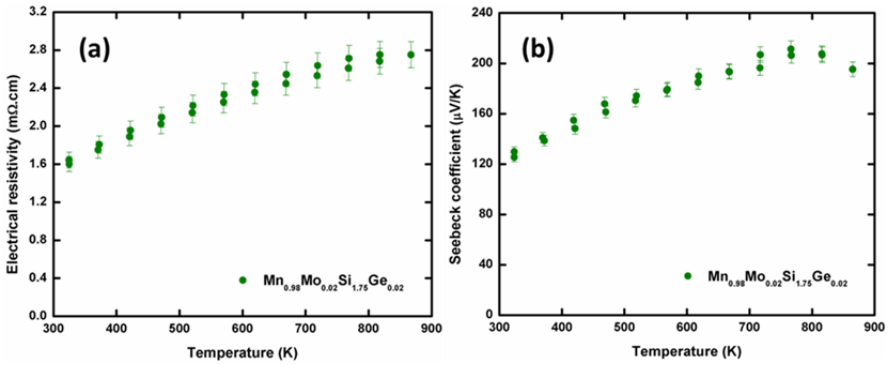

Figure 5.5 Temperature dependence of (a) electrical resistivity with the estimated error of 5% and (b) Seebeck coefficient with the estimated error of 3% of $Mn_{0.98}Mo_{0.02}Si_{1.75}Ge_{0.02}$ at heating up and cooling down.

The experimental specific heat is shown in Figure 5.6; limitations of the calculated values, varying between 0.634 $J{\cdot}K^{-1}{\cdot}g^{-1}$ and 0.655 $J{\cdot}K^{-1}{\cdot}g^{-1}$, are shown by lines for comparison. The measured data had only small temperature dependence, especially above 600 K, and were lower than the Dulong–Petit values, with the exception of the base materials, the experimental values for which were very close to the theoretical values. A maximum discrepancy of up to 30% was observed for the (W, Al)-substituted sample. C_P determination was always a controversial issue, and strongly depended on the instruments, methods, manipulations, and materials and the experimental errors could sometimes be very large. Moreover, the reproducibility of C_P measurements for the HMS-based samples prepared in this work was quite low, because of the presence of phase mixtures. It should be emphasized that the calculated figure of merit would be improved by using the experimental specific heat for calculation of thermal conductivity. However, the Dulong–Petit specific heat was used in this report to avoid the uncertainty of the measurements, the effects of sample quality, and because of our preference to underestimate rather than overestimate thermoelectric performance.

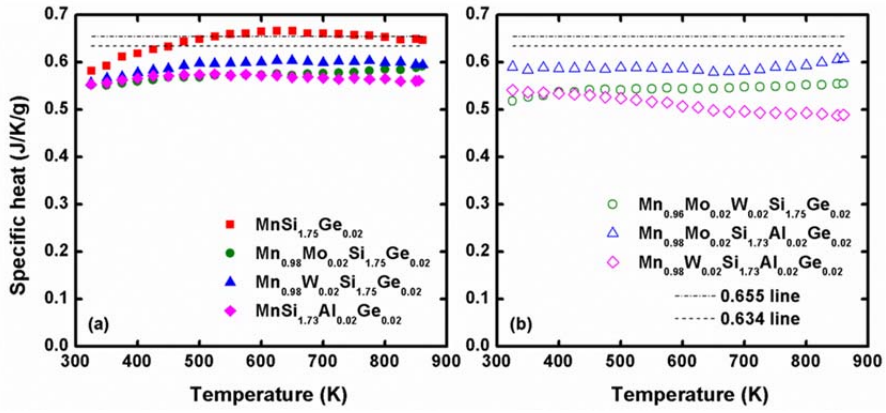

Figure 5.6 Temperature dependence of specific heat of HMS-based materials with the dash–dot line representing the highest Dulong–Petit value (0.655 $J \cdot K^{-1} \cdot g^{-1}$), and the dashed line representing the lowest Dulong–Petit value (0.634 $J \cdot K^{-1} \cdot g^{-1}$): (a) the base and the single-substituted materials; (b) the double-substituted materials.

c_{Mn}/c_{Si} ratios calculated from refined cell constants were nearly identical for all the samples, suggesting no transition between different HMS compounds as a result of substitution. Consequently, the theoretical densities of HMS-based materials given in

Table 5.2 were calculated from the refined cell volumes and the density of the corresponding $Mn_{11}Si_{19}$ compound (taken from Inorganic Crystal Structure Database). Experimental and calculated densities are compared in the same table; the results indicated that all the pellets were dense enough for physical property measurements.

The electrical resistivity of all the samples increased steadily with increasing temperature, as shown in Figure 5.7. This behavior is typical of materials with high carrier concentration, for example heavily doped semiconductors or metals. Carrier mobility decreased at high temperature, because of increasing acoustic phonon scattering. The electrical resistivity curves of the Mo and W-substituted samples were nearly identical over the whole temperature range, increasing from approximately 1.6 mΩ·cm at 325 K to approximately 2.7 mΩ·cm at 815 K; these values were approximately 10% lower than those of the Al-substituted sample and the base material.

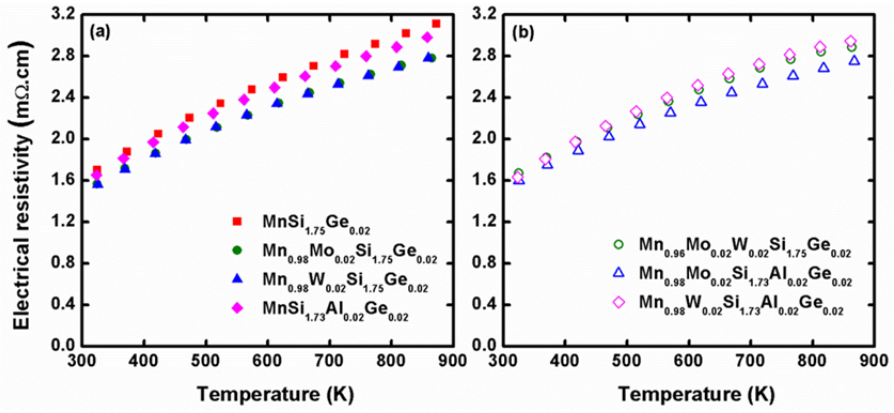

Figure 5.7 Temperature dependence of the electrical resistivity of HMS-based materials: (a) the base and the single-substituted materials; (b) the double-substituted materials.

The behavior of the Seebeck coefficient, increasing with temperature up to 775 K and decreasing slightly at approximately 815 K (Figure 5.8), was indicative of an extrinsic semiconductor. The Seebeck coefficients of the Mo and Al-substituted samples were equal to those of the base material whereas that of the W-substituted sample was 10% lower, ranging from 118 μV/K at 325 K to 200 μV/K at 715 K, where the difference between the thermopower of the materials has vanished. The highest Seebeck coefficient was 216 μV/K, reached at approximately 775 K.

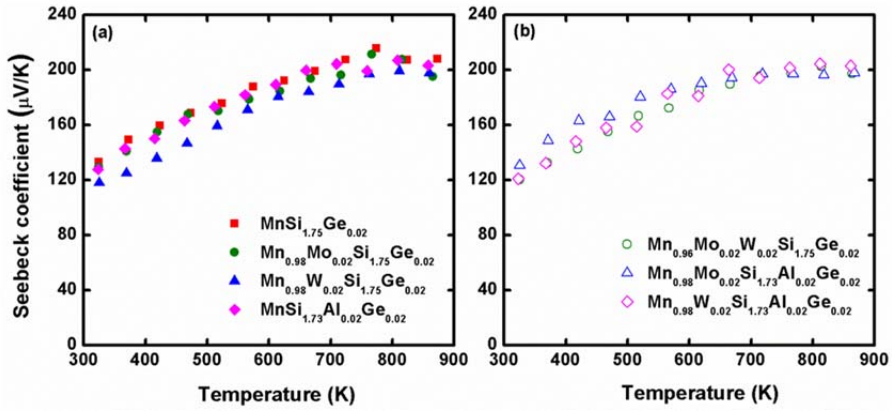

Figure 5.8 Temperature dependence of the Seebeck coefficient of the HMS-based materials: (a) the base and the single-substituted materials; (b) the double-substituted materials.

The substituent elements are in the groups to the left of manganese and silicon, respectively; thus, they provide fewer valence electrons, increasing the concentration of holes, which are the major charge carriers. Luo *et al.*[129] reported a 20% increase of hole concentration from 0.46×10^{21} cm^{-3} to 0.56×10^{21} cm^{-3} on substituting Si sites in $MnSi_{1.80}$ with 1 at.-% aluminium. However, a decrease in the carrier density compared with the undoped HMS was expected with further increasing aluminium content, considering the decreasing trend of the hole concentration when an amount higher than 0.22 at.-% of aluminium was substituted at the Si sites. Similarly, a threefold increase from approximately 1.2×10^{21} cm^{-3} to 3.6×10^{21} cm^{-3} was achieved by substituting 0.6 at.-% aluminium at Si sites in $MnSi_{1.80}$.[150] Moreover, Ponnambalam *et al*. demonstrated that 3 at.-% chromium substitution at Mn sites increased the hole content by up to 25%.[143] Formation of $MoSi_2$ and WSi_2 phases with high hole concentrations of 4.0×10^{21} cm^{-3} and 7.5×10^{21} cm^{-3},[206] respectively, also contributed to increasing the carrier concentrations of the materials. As a consequence, the electrical resistivity of the base material was reduced by substituting Mn with Mo and W, or Si with Al.

However, the Seebeck coefficient changed insignificantly over the whole temperature range, which was attributed to reduction of carrier mobility by enhanced scattering effects, because of the presence of side products and lattice distortions in addition to the increased carrier concentration. This atypical behavior has been observed by Luo *et al.*,[118] and suggested a higher Seebeck coefficient could be obtained by controlling the morphology and the distribution of the side products. The small discrepancy below 715 K for the W-substituted sample compared with the undoped sample was explained by the presence of WSi_2, which resulted in a much higher hole concentration than the HMS matrix.

As shown in Figure 5.9, the thermal conductivity decreased monotonically from low to moderate temperature in the range 300–750 K, and increased at high temperature starting from approximately 800 K. Combining this observation with that obtained by studying the Seebeck coefficient, it can be concluded that bipolar transport effects were initiated below 800 K. The thermal conductivity of the single-substituted materials was reduced over the whole temperature range, because of increased phonon scattering by lattice distortion as a result of substitution.

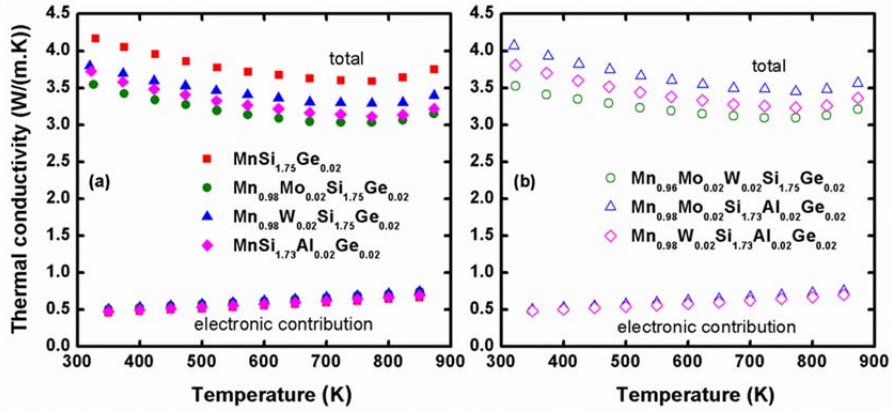

Figure 5.9 Temperature dependence of the total (> 3 $W \cdot m^{-1} \cdot K^{-1}$) and electronic thermal (< 1 $W \cdot m^{-1} \cdot K^{-1}$) conductivity of HMS-based materials: (a) the base and the single-substituted materials; (b) the double-substituted materials.

Here, the Sommerfeld theoretical value of the Lorenz number ($L = 2.44 \times 10^{-8}$ $V^2 \cdot K^{-2}$), usually used for degenerate semiconductors or metals, was used to calculate the electronic thermal conductivity. The lattice thermal conductivity, which was more than 80% of the total value, presented in Figure 5.10, resulting from subtraction of the electronic contribution from the total thermal conductivity, was also reduced. This observation was in agreement with other reports on Al, Mo, and Cr-doped HMS.[112,129,143,150] Liu *et al.*[111] however, reported a different observation for chromium-doped polycrystalline HMS prepared by ball milling and *in situ* SPS, but were not able to explain the reason for this unusual behavior. The comparison with chromium as dopant was chosen because of the lack of a similar investigation for molybdenum and tungsten, all of which belong to the same group in the periodic table. The largest reduction was obtained for the single-substituted sample with 2 at.-% of molybdenum at Mn sites, which was approximately 20% and 25% for the total and lattice thermal conductivity, respectively; this was a consequence of the large distortion of the lattice caused by Mo atoms, which was apparent from the modifications of the lattice parameters reported above. The total thermal conductivity of the Mo-substituted sample ranged from 3.54 $W \cdot m^{-1} \cdot K^{-1}$ at 325 K to 3.06 $W \cdot m^{-1} \cdot K^{-1}$ at 815 K.

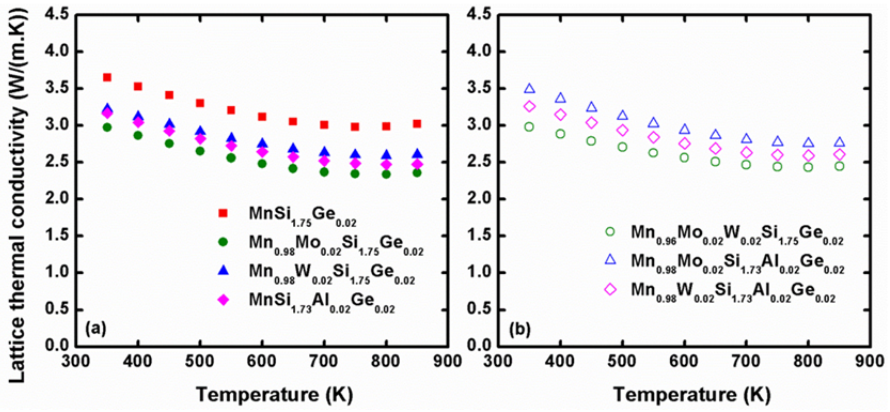

Figure 5.10 Temperature dependence of the lattice thermal conductivity of HMS-based materials: (a) the base and the single-substituted materials; (b) the double-substituted materials.

Because of the presence of a phase mixture, the electrical properties of the double-substituted samples changed in a more complex way than by simply adding the effects of the corresponding single-substituted ones. Here, the example of the (Mo, Al) double-substituted material was compared with the Mo and Al-substituted samples. Its electrical resistivity was nearly identical to that of the Mo-substituted sample and slightly less than that of Al-substituted and base materials. Moreover, the Seebeck coefficients of these materials were very similar from low to moderate temperature (approx. 750 K), and were slightly (6%) different at approximately 815 K from that of the Al-substituted material. This behavior was explained by the dominant lattice distortion effects of molybdenum substitution on charge transport, judging by the refined unit cell parameters. However, both the total and lattice thermal conductivity of the (Mo, Al) substituted material, ranging from 4.07 $W \cdot m^{-1} \cdot K^{-1}$ at 325 K to 3.48 $W \cdot m^{-1} \cdot K^{-1}$ at 815 K, and from 3.56 $W \cdot m^{-1} \cdot K^{-1}$ at 325 K to 2.75 $W \cdot m^{-1} \cdot K^{-1}$ at 815 K, respectively, were unexpectedly higher than that of the single-substituted one, but still lower than those of the base material over the entire temperature range. Interestingly, the lattice thermal conductivity of the (Mo, W) substituted sample, which decreased from 3.03 $W \cdot m^{-1} \cdot K^{-1}$ at 325 K to 2.44 $W \cdot m^{-1} \cdot K^{-1}$ at 815 K, was nearly identical with that of the Mo-substituted one, despite the greater distortion.

A summary of all the properties at 325 K and 815 K is given in Table 5.4. In general, the large reduction in thermal conductivity has overcome the smaller change of the electrical properties because of the low substituent contents; this resulted in enhancement of the figure of merit for all the samples, as is apparent from Figure 5.11. The maximum improvements were approximately 23% and 15% for Mo and Al-substituted samples, respectively, and the performance of the (Mo, Al) substituted sample was equal to that of the base material, within experimental error. Samples containing W were of moderate performance with maximum *ZT* values of approximately 0.36–0.37. The best figure of merit, achieved at 815 K, was 0.40 for the sample with 2 at.-% molybdenum at Mn sites.

Table 5.4 Thermoelectric properties of HMS-based materials at 325 K/815 K.

Nominal compositions	S (μV/K)	ρ (mΩ.cm)	κ ($W \cdot m^{-1} \cdot K^{-1}$)	κ_l ($W \cdot m^{-1} \cdot K^{-1}$)	ZT
$MnSi_{1.75}Ge_{0.02}$	133/208	1.70/3.02	4.16/3.64	3.71/3.00	0.08/0.32
$Mn_{0.98}Mo_{0.02}Si_{1.75}Ge_{0.02}$	130/208	1.57/2.71	3.54/3.06	3.04/2.34	0.10/0.40
$Mn_{0.98}W_{0.02}Si_{1.75}Ge_{0.02}$	118/199	1.56/2.69	3.80/3.30	3.28/2.59	0.08/0.35
$MnSi_{1.73}Al_{0.02}Ge_{0.02}$	128/207	1.65/2.89	3.72/3.13	3.23/2.47	0.08/0.38
$Mn_{0.96}Mo_{0.02}W_{0.02}Si_{1.75}Ge_{0.02}$	120/202	1.67/2.84	3.52/3.13	3.03/2.44	0.08/0.37
$Mn_{0.98}Mo_{0.02}Si_{1.73}Al_{0.02}Ge_{0.02}$	131/196	1.60/2.68	4.07/3.48	3.56/2.75	0.09/0.34
$Mn_{0.98}W_{0.02}Si_{1.73}Al_{0.02}Ge_{0.02}$	121/205	1.63/2.89	3.81/3.26	3.32/2.59	0.08/0.36

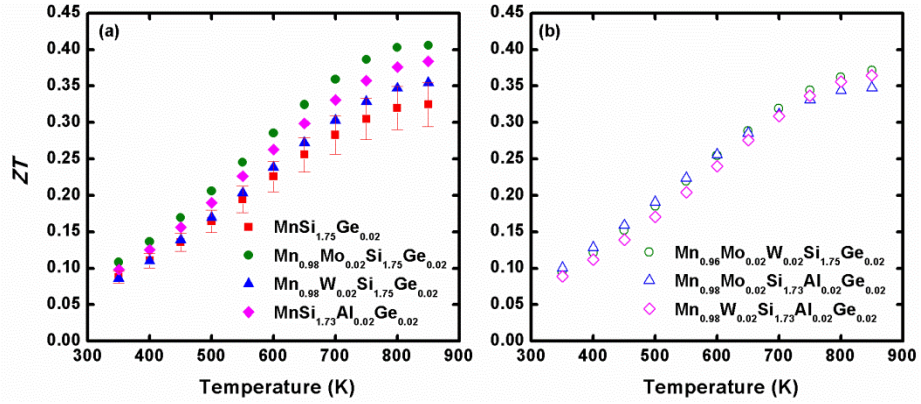

Figure 5.11 Temperature dependence of the figure of merit for HMS-based materials: (a) the base and the single-substituted materials; (b) the double-substituted materials.

5.3.3 Effects of Ag substitutions with different concentrations

The P-XRD patterns showed a low solubility of Ag in the HMS-based material (Figure 5.12), where the peaks of elemental Ag clearly appeared in the powder diagrams even at a low concentration of 1 at.-% at the Mn sites. This has been previously predicted from the large difference of the covalent radius between Ag and Mn. Moreover, no MnSi peaks could be observed, while the relative intensities of Si peaks slightly reduced in comparison to the base material. The presence of Ag, therefore, either possibly enhanced the HMS formation or partly reacted with Si to form silver silicide in trace amounts, which was undetectable within the detection limit of P-XRD.

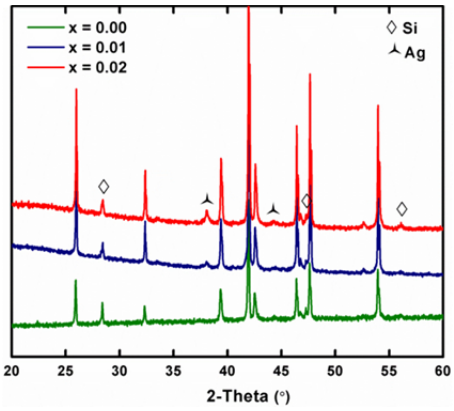

Figure 5.12 XRD patterns of the $Mn_{1-x}Ag_xSi_{1.75}Ge_{0.02}$ materials.

Le Bail refinement revealed slightly reduced parameters for the samples with 1 at.-% of Ag substitution, and increased sizes for the material containing 2 at.-% of Ag compared to those of the base material (Table 5.5). It should be noted that the Ag-containing samples were characterized on a different time to the Ag-free material, which could induced significant errors to the refinement results, especially with the high backgrounds coming from the presence of Mn. However, the increase of lattice parameters except for c_{Si} with increasing the Ag content could be noticed, implying that more Ag might be introduced into the HMS matrix by increasing its initial concentration. Surprisingly, the increased Ag

substitution showed no effects on the *c*-axis of Si subcells, which was usually the easily modified axis due to the weak interaction between Si atoms. This led to an increase of the c_{Mn}/c_{Si} ratio, indicating that the addition of Ag could cause a phase transformation between different structural formulas in the HMS system.

Table 5.5 Le Bail-refined parameters for Mn and Si sublattices of the $Mn_{1-x}Ag_xSi_{1.75}Ge_{0.02}$ materials.

Nominal compositions	a_{Mn} (Å)	c_{Mn} (Å)	a_{Si} (Å)	c_{Si} (Å)	c_{Mn}/c_{Si}
$MnSi_{1.75}Ge_{0.02}$	5.5256(2)	4.3682(2)	3.9074(2)	2.5268(2)	1.7287(2)
$Mn_{0.98}Ag_{0.01}Si_{1.75}Ge_{0.02}$	5.5252(3)	4.3677(3)	3.9066(3)	2.5240(3)	1.7305(2)
$Mn_{0.98}Ag_{0.02}Si_{1.75}Ge_{0.02}$	5.5284(3)	4.3700(3)	3.9089(3)	2.5240(3)	1.7314(2)

The electrical resistivity of the $Mn_{1-x}Ag_xSi_{1.75}Ge_{0.02}$ materials showed either similar values or a small increase of approximately 10% at low Ag concentrations up to 5 at.-% to that of the base material (Figure 5.13 (a)). The resistivity then significantly increased up to 30% in the sample with 10 at.-% of Ag substitution at the Mn sites, reaching approximately 4 mΩ·cm at around 815 K. Moreover, all the Seebeck coefficients of the Ag-containing samples fell within the experimental error range of the phase mixture of the nominal $MnSi_{1.75}Ge_{0.02}$ composition (Figure 5.13 (b)), signifying a similar carrier concentration between different Ag concentrations. As a consequence, the presence of Ag, especially at high content, created scattering centers to disturb the charge transport or reduce the carrier mobility.

The thermal conductivity of $MnSi_{1.75}Ge_{0.02}$ was reduced from 4.16 $W \cdot m^{-1} \cdot K^{-1}$ to 3.69 $W \cdot m^{-1} \cdot K^{-1}$ at 325 K in the sample containing 1 at.-% Ag at the Mn sites (Figure 5.13 (c)). The Ag substitution at low concentration enhanced the phonon scattering, which decreased the thermal conduction in HMS-based materials. However, further introductions of Ag at high content gradually increased the thermal conductivity due to the high thermal conduction

of the Ag substitution. The total thermal conductivity reached around 4.8 $W \cdot m^{-1} \cdot K^{-1}$ in the material containing 10 at.-% of Ag at the Mn sites. The high electrical resistivity and thermal conductivity resulted in low *ZT* values of the material with 10 at.-% of Ag at the Mn sites, achieving only 0.23 at 850 K (Figure 5.13 (d)). The compositions including 5 at.-% of Ag obtained similar performance to that of the base material, while the ones containing low Ag contents exhibited slightly higher *ZT* values. The maximum improvement was approximately 15%, increasing from 0.32 to 0.37 at 850 K, for the sample containing 1 at.-% of Ag substitution owing to its reduced thermal conductivity.

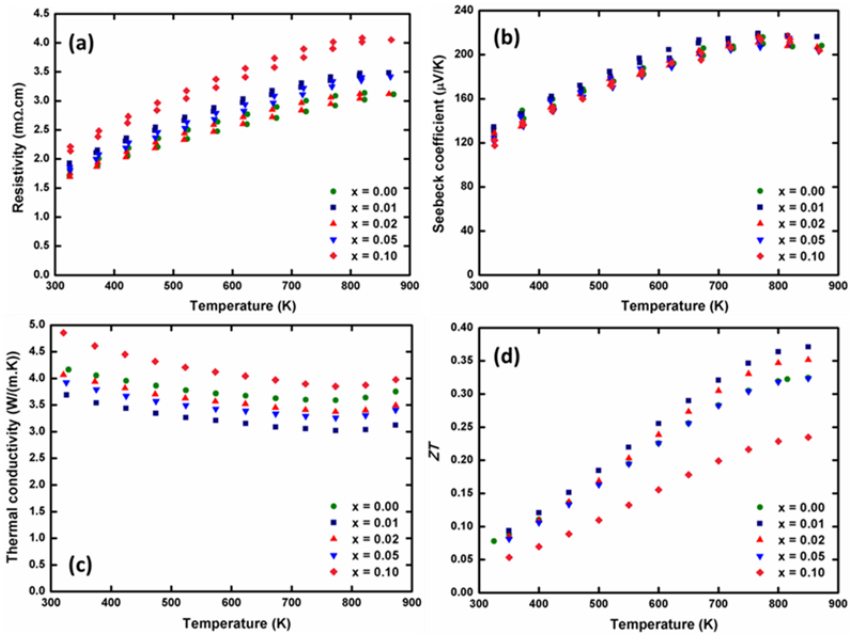

Figure 5.13 Temperature dependence of (a) electrical resistivity, (b) Seebeck coefficient, (c) thermal conductivity, and (d) *ZT* in the $Mn_{1-x}Ag_xSi_{1.75}Ge_{0.02}$ materials.

Ag exhibited low solubility in HMS-based materials, generated extra peaks in the powder diagrams of the base material even at a low content. Materials containing large Ag amounts showed not only an increased electrical resistivity but also a high thermal conductivity, which led to reducing the thermoelectric performance. However, a small

amount of Ag substitutions introduced scattering centers to scatter the phonons, which reduced the thermal conductivity and improved the *ZT* value. Therefore, effects of Ag substitutions at low concentrations with different morphologies might be potential for further studies.

5.4 Conclusions

HMS-based materials substituted by molybdenum, tungsten, silver, germanium and aluminium at the Mn and Si sites were prepared by an easy and effective method. Among different stoichiometric and non-stoichiometric compositions containing Ge, $MnSi_{1.75}Ge_{0.02}$ showed the best performance apparently due to the lowest MnSi amount presenting in this material. This composition was then selected as the base material for further substitutions.

Le Bail refinement revealed enlargements of the unit cells, especially for molybdenum substitution at Mn sites. The electrical resistivity was reduced by substitution, owing to the increased carrier concentration. The Seebeck coefficient was changed insignificantly, because of reduced carrier mobility as a result of scattering effects. In general, the electrical properties of all the substituted samples were only slightly improved, because of the small amounts of substituents. Substitution did, however, reduce the lattice thermal conductivity of the base material for both single and double-substituted materials. Consequently, the figure of merit was improved, reaching a maximum value of 0.40 at 815 K for the Mo-substituted sample.

Low solubility was found in case of Ag substitution attempts, and the presence of Ag in high contents increased the electrical resistivity and thermal conductivity of the base material, which lowered its thermoelectric performance. Nevertheless, the material with low Ag concentration of 1 at.-% at the Mn sites showed a reduced thermal conductivity and enhanced *ZT* value, which might be an interesting topic for future works.

Overall, it is believed that the thermoelectric efficiency of HMS-based materials could be improved further by optimizing the amounts of substituents, the morphology, and the synthesis and processing methods.

Chapter 6

Preparation of pure Higher Manganese Silicides through wet ball milling and reactive sintering with enhanced thermoelectric properties[III]

Abstract

Different synthesis processes were employed attempting to synthesize doped and undoped HMS materials for thermoelectric purposes, e.g. mechanical alloying, mechanical milling and heat treating in conventional furnace, solid state reaction, chemical vapor transport, and ball milling and reactive spark plasma sintering. In order to avoid the agglomerations of the powders on the inside walls of the vials and around the balls, resulting in low yield and stoichiometric loss, either soft ball milling in combination with subsequent heat treatment or traditional solid state reaction was investigated on different compositions of HMS-base materials. The maximum *ZT* values ranging from 0.31 to 0.42 have been achieved for various compositions, which could possibly be improved by completely eliminating the side products. However, the problem of time consumption would probably confine these processes into laboratory scale rather than for industrial applications.

A simple and effective process was used to synthesize undoped Higher Manganese Silicides (HMS), involving ball milling under soft conditions to obtain homogeneous mixtures of constituting elements, and subsequent spark plasma sintering for a direct solid state reaction. For comparison purpose, the ball milling step was carried out under both dry and wet conditions using *n*-hexane as the liquid medium. Analysis of the granulometry demonstrated that the wet milling process in *n*-hexane results in finer particles, thus improving the reaction rate later on. According to XRD and scanning microscopy, materials

[III] Part of this chapter is reprinted from *Intermet*., *66*, D. Y. N. Truong, H. Kleinke, F. Gascoin, *Preparation of pure Higher Manganese Silicides through wet ball milling and reactive sintering with enhanced thermoelectric properties*, 127-132, Copyright (2015), with permission from Elsevier.

produced via wet milling and spark plasma sintering contained only HMS while dry milled samples contained MnSi impurities. The Seebeck coefficient of the wet milling sample was 20% higher, while its electrical resistivity was 23% lower than those of the dry milling one over the whole temperature range. Moreover, the thermal conductivity was reduced up to 30% when using *n*-hexane as milling media. The maximum thermoelectric figure of merit obtained was 0.55 at 850 K, a high value for undoped HMS.

Moreover, single crystals of HMS have been prepared using chemical vapor transport with very low yield, but their qualities were not good enough for the superstructure reflections to be resolved using single crystal XRD. Consequently, all the obtained crystals were identified as the simplest structural formula of Mn_4Si_7.

6.1 Introduction

The techniques utilized for synthesizing bulk HMS can mainly be divided into two categories: melting process and solid state reaction. In the first approach, the high melting points of manganese (1263ºC) and silicon (1414ºC) are one of the big obstacles, especially in large scale synthesis. Additionally, the compositional control is a challenge at elevated temperature due to the high vapor pressure of manganese. Moreover, HMS produced by melting method always contain secondary phases of manganese monosilicide MnSi and of elemental Si because HMS melt incongruently. The striations of the monosilicide phase MnSi were reported by many authors for the as-grown ingots obtained from Bridgman, Czocharalski, and other techniques using the solidification of a melt.[99,106,108–110,114] The precipitates are observed as parallel thin planes, which usually grow perpendicular to the *c*-axis of the HMS matrix. This metallic secondary phase is known to be detrimental to the thermoelectric performance as it generates electrical short-circuits in the matrix materials, which, consequently, degrades their thermopower and at the same time increases their thermal conductivity. Theoretically speaking, a high cooling rate is required to avoid the decomposition of the liquid phase into MnSi and Si, which is practically unachievable at the moment.

For industrial production, solid state techniques are often preferred due to lower energy consumption, and homogeneity of the product. The driving force for the diffusion process is provided by either mechanical or thermal energy. On one hand, the mechanical alloying usually requires hard conditions for the formation of HMS, including high ball-to-powder ratio (BPR),[132,133,139] high rotation speed,[136,139] and long milling duration.[103,116,117,136] The biggest problem encountered for applying hard ball milling conditions is the agglomeration of the powder around the balls and on the inside wall of the vials.[167,207] The agglomeration causes a loss of materials, but more importantly causes a departure from stoichiometry of the compounds. Aside from the low efficiency due to the material loss, the stoichiometric aspect is more essential for Higher Manganese Silicides due to the existence of various compounds with different transport properties in a very narrow compositional range (from 63 to 64 at.-% of silicon). Furthermore, a loss of silicon during the processing has been recognized by several groups,[132,133,139] which can be explained by its more adhesive characteristics than manganese, a softer element.

On the other hand, the typical solid state reaction usually requires several days or weeks with intermediate manual grindings to prepare HMS due to the slow diffusion rate of Si.[100,127,150,208] The ball-milling process is an alternative solution to achieve finer and more homogeneous mixtures, which helps to avoid the regrinding step during the heat treatment. The heat treating process can be done in conventional furnace,[100,116,127,150,208] or during the consolidation such as in hot press,[209] pulse discharge sintering, and spark plasma sintering apparatus.[111]

In this chapter, various synthesis methods were attempted with the aim to prepare pure HMS compounds, e.g. mechanical alloying, mechanical milling under soft conditions combining with subsequent heat treatments in conventional furnace, solid state reaction, chemical vapor transport, and ball milling and reactive spark plasma sintering. Amongst different methods, the thermoelectric performances of HMS material prepared by ball milling in *n*-hexane, followed by heat treatment using spark plasma sintering showed the best efficiency owing to its phase purity. The improvement of solid state reaction rate by using small particle sizes is illustrated here through a comparative study between the wet milled

and dry milled compounds, while the other preparation methods are also reported thoroughly including their achievements as well as the limitations.

6.2 Experimental section

All the samples were prepared from Mn powder, 99.95%, -325 mesh, and Si powder, crystalline, 99.9%, -100 mesh, all purchased from Alfa Aesar. Due to the employment of different synthesis methods, the section of results and discussion will be correspondingly divided, where the descriptions of the processes will be given at the beginning of each sub-section.

6.3 Results and discussions

6.3.1 Mechanical alloying

The $MnSi_{1.75}$ stoichiometry was first attempted to synthesize using ball milling at different speeds from 400 rpm to 700 rpm and various durations from 30 minutes to 180 minutes divided into rounds of 15 minutes in opposite directions. Both milling vials and balls were made of tungsten carbide with a ball diameter of 10 mm and a high BPR (weight) of approximately 16:1, i.e. 5 grams of powder and 10 balls. Generally, the formation of HMS phases was observed at high input energy, where the HMS content was increased with increasing the milling energy, i.e. higher speed or longer duration (Figure 6.1 (a)). Additionally, the formation of MnSi with increasing amounts was also revealed in all the case studies.

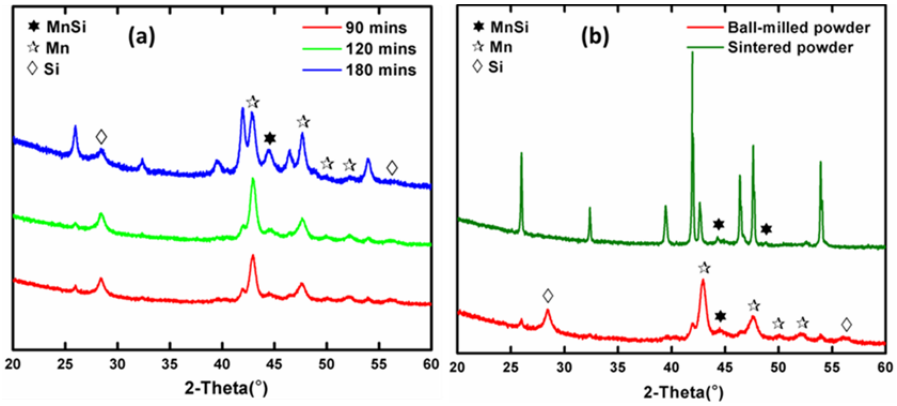

Figure 6.1 P-XRD patterns of (a) the elemental mixtures ball-milled at different durations with a rotation speed of 600 rpm, (b) the samples ball-milled at 600 rpm for 90 minutes before and after sintering; the unlabeled peaks represent the HMS phases.

Shin *et al.*[133] used hardened steel vials and steel balls with a diameter of 5 mm to synthesize $MnSi_{1.75-\delta}$ (δ = 0, 0.01, 0.02, 0.03) using mechanical alloying. The vials were loaded with a high weight BPR of 20:1, while a low rotation speed of 300 rpm or 400 rpm in combination with a prolonged duration up to 48 hours was employed for the milling process. Similarly, the formation of MnSi were indicated, which was explained by the decomposition of the synthesized HMS due to the excess collision energy. The authors suggested that a complete synthesis of HMS should come from a milling procedure with high rotation speed and short duration, which was determined to be 6 hours at 400 rpm in the report.

Sadia *et al.*[139] have employed zirconium oxide vials and balls with a small diameter of 1.5 mm, and a high volume BPR of 20:1. The rotation speed was varied from 400 rpm to 800 rpm, while the milling duration was increased from 1 hour up to 7 hours. The increasing MnSi content was indicated for the ball milling longer than 5 hours at 800 rpm, which was explained by the adhesion of silicon to the vial and the partial decomposition of HMS. However, the use of the same zirconia vials and balls and an identical BPR has led to the formation of HMS at only 400 rpm for 1 hour.[132] The optimal milling conditions using zirconia vials and balls are, therefore, still questionable, but the high adhesion of silicon on the inside walls and around the balls has impeded their usages for HMS materials.

Interestingly, single phase of $MnSi_{1.73}$ was formed after 12 milling hours at a large rotation speed up to 1750 rpm, but the materials made of the vials and balls were not clarified in the report.[136]

Here, the utilization of tungsten carbide vials and balls with higher hardness allowed shorter milling durations. The agglomeration of the powder on the vial walls was gradually noticed with increasing mechanical energy, and the adhesion around the balls appeared to be unavoidable for all the investigated cases (Table 6.1). When the powder mixtures were ball-milled at 700 rpm, the vials were highly heated and the powders became too adhesive to be removed after the experiments. Consequently, the longest time used at this speed was only 60 minutes.

Table 6.1 A summary of ball milling conditions and corresponding observations; A: The formation of HMS, B and C: The agglomeration of the powder around the inside walls of the milling vials and the milling balls, respectively.

Speed/Duration	30 minutes	60 minutes	90 minutes	120 minutes	180 minutes
400 rpm	C	C	C	C	C
500 rpm	C	C	C	A, B, C	A, B, C
600 rpm	C	A, B, C	A, B, C	A, B, C	A, B, C
700 rpm	A, B, C	A, B, C	-	-	-

The $MnSi_{1.75}$ material has been prepared by ball milling using tungsten carbide vials and balls with a low weight BPR of 5 was identified to be pure HMS using XRD after being milled at 650 rpm for 159 hours.[116,117] Employing the same ball milling system and BPR, the presence of MnSi phase was indicated until 16 hours at 500 rpm, which was decreasing for longer milling times and disappeared after 80 hours.[103] A complete synthesis of HMS was unachievable under the investigated milling conditions, but it is anticipated to occur earlier than in the previous reports due to the utilization of a higher BPR.

The material ball-milled at 600 rpm for 90 minutes was subjected to densification using SPS at 1000ºC for 1 hour under a pressure of 90 MPa. The graphite die containing sample was heated from 20ºC to 1000ºC for 30 minutes, and cooled down to 20ºC for one hour after being sintered. The pressure was gradually increased from 28 MPa to 90 MPa along with the heating procedure, and decreased to 28 MPa along with the cooling step. The sample after being sintered mainly consisted of HMS with a small amount of MnSi (Figure 6.1 (b)). The HMS peaks were sharpened due to significant grain growths and recrystallization during sintering. Surprisingly, no extra silicon was detected using XRD, indicating that silicon was in the amorphous phase or lost due to agglomeration during ball milling.

6.3.2 Mechanical milling and furnace heating

In order to avoid the agglomeration, the elemental mixture was blended under soft milling conditions, i.e. at 400 rpm for only 4 minutes divided into two rounds in opposite directions with a low weight BPR of 4:1, i.e. 10 grams of powder and 5 balls. The obtained mixture containing only the constitutional elements was underwent heat treatments in conventional furnace at 1000ºC for 72 hours before being densified with the same temperature and pressure profiles.

The materials after heat treatments mainly consisted of HMS with trace amounts of MnSi and Si (Figure 6.2 (a)). The phase compositions were maintained after the sintering, where the presence of Si peak indicated that the stoichiometry was possibly preserved with the soft milling conditions.

Different $MnSi_x$ compositions, where x = 1.70, 1.75, and 1.80, and the $Mn(Si_{0.99}Ge_{0.01})_{1.75}$ compound were also prepared using the same procedure, giving similar phase compositions after being heat treated in conventional furnace (Figure 6.2 (b)). The material with Si deficiency of $MnSi_{1.70}$ contained a higher amount of the MnSi phase than in the $MnSi_{1.75}$ sample, while excess Si content was observed in the powder diagram of $MnSi_{1.80}$. Surprisingly, the MnSi peak was hindered in the XRD pattern of the Ge-subsituted sample. As aforementioned in chapter 5, a small amount of Ge possibly promoted the

reaction between MnSi and Si to form HMS, which reduced the contents of these side products in the final materials.

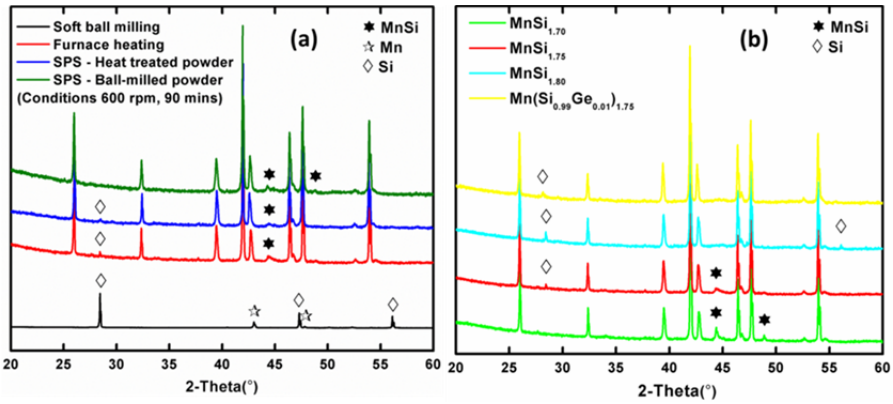

Figure 6.2 P-XRD patterns of (a) the $MnSi_{1.75}$ composition after ball milling under soft conditions, heat treating in conventional furnace, and sintering, (b) different $MnSi_x$ compositions with x = 1.70, 1.75, and 1.80 and the $Mn(Si_{0.99}Ge_{0.01})_{1.75}$ compound after heat treatments using conventional furnace.

All the materials were densified using spark plasma sintering applying the same parameters, i.e. at 1000ºC for 1 hour under a pressure of 90 MPa. The experimental densities determined via Archimedes' method are given in Table 6.2 in comparison with the theoretical values. The theoretical densities of $MnSi_{1.70}$ and $MnSi_{1.80}$ were calculated by use of the formula $1/d = \Sigma W_i/d_i$, where W_i and d_i are, respectively, the mass fraction and density of the $MnSi_{1.75}$ compound and the side products, including Si: 2.33 g/cm^3; MnSi: 5.83 g/cm^3 (all taken from the Inorganic Crystal Structure Database), for the corresponding equations considering a complete reaction.

$$15MnSi_{1.70} \rightarrow 14MnSi_{1.75} + MnSi$$

$$20MnSi_{1.80} \rightarrow 20MnSi_{1.75} + Si$$

The theoretical density of the $Mn(Si_{0.99}Ge_{0.01})_{1.75}$ material was estimated from that of the $MnSi_{1.75}$ under the assumption that a small amount of Ge substitution did not change the unit cell volume significantly. All the experimental densities were more than 95% of the theoretical ones, which were sufficient for the subsequent physical property measurements.

Table 6.2 Nominal compositions, theoretical and experimental densities of HMS-based materials.

Nominal compositions	Theoretical density (g/cm^3)	Experimental density (g/cm^3)	Percentage (%)
$MnSi_{1.70}$	5.18	5.07	98
$MnSi_{1.75}$	5.15	4.90	95
$MnSi_{1.80}$	5.07	4.92	97
$Mn(Si_{0.99}Ge_{0.01})_{1.75}$	5.19	5.01	96
$MnSi_{1.75}$ (Ball-milled powder)	5.15	4.88	95

The electrical resistivity of HMS-based materials steadily increased with heating up to certain temperature depending on the chemical compositions, where the bipolar diffusion occurred, and then flatted out or decreased above this temperature (Figure 6.3 (a)). The $MnSi_{1.70}$ and Ge-containing samples exhibited lower electrical resistivity, while slightly higher resistivity than that of the $MnSi_{1.75}$ composition was achieved in the $MnSi_{1.80}$ material. However, the Seebeck coefficient values were almost similar, where the difference to the $MnSi_{1.75}$ material was less than 10%, indicating comparable carrier concentrations in all the samples due to small compositional variations (Figure 6.3 (b)). Therefore, the discrepancy in the electrical resistivity came from the carrier mobility because of scattering with the side products. The presence of the metallic MnSi phase facilitated the charge transport, increasing the charge mobility in $MnSi_{1.70}$, while the excess insulating Si phase enhanced the scattering of charge carriers, reducing their mobility in $MnSi_{1.80}$. The introduction of a small amount of Ge decreased the formation of side products, which were the scattering centers in the HMS

matrix; thus, the carrier mobility was significantly improved, resulting in a reduction of approximately 30% for the electrical resistivity over the whole temperature. The $Mn(Si_{0.99}Ge_{0.01})_{1.75}$ material possessed the lowest resistivity, ranging from 1.8 mΩ·cm to 3.3 mΩ·cm for the entire temperature range of 300 K – 900 K. The $MnSi_{1.75}$ sample prepared by mechanical alloying showed nearly identical Seebeck coefficient to the material synthesized in the conventional furnace, but a reduced electrical resistivity of around 20% for the entire temperature range investigated even though these two materials had nearly the same relative density of 95-96%. This could be explained by either the increased amount of MnSi phase or the loss of excess Si in the ball-milled sample, which decreased resistivity.

The thermal conductivity of HMS-based materials decreased with increasing temperature, and then increased again at high temperature due to bipolar diffusion (Figure 6.3 (c)). The presence of high levels of MnSi or Si, having high thermal conductivity, caused increased thermal conduction in $MnSi_{1.70}$ and $MnSi_{1.80}$ compared to in $MnSi_{1.75}$. The difference was as large as 20% at 325 K, though the difference vanished at high temperature, where the thermally activated electrons had large contributions to the thermal conduction. The Ge substituted material showed the lowest thermal conductivity, varying from 2.6 $W \cdot m^{-1} \cdot K^{-1}$ to 2.9 $W \cdot m^{-1} \cdot K^{-1}$ for the whole temperature range because of the defects generated from the introduction of Ge which scatter phonons. The sample prepared by mechanical alloying displayed a higher thermal conductivity than the one synthesized by heat treatments in conventional furnace from 300 K up to approximately 725 K, where their thermal conduction values almost coincided, then changed the order above this temperature. From 775 K to 875 K, the ball milled material showed nearly identical thermal conductivity to the Ge-containing sample. The different amounts of side products could explain the difference at low to moderate temperature, while the enhanced defect scattering generated by ball milling might be the reason of the observed changes at high temperature.

The *ZT* of the $MnSi_x$ where x = 1.70, 1.75, and 1.80, all reached the maximum value at around 700 K, then decreased at high temperature (Figure 6.3 (d)). The differences in electrical resistivity were compensated in thermal conductivity, leading to comparable thermoelectric efficiency over the entire temperature range, where the highest *ZT* varied from

0.31 to 0.32 at above 700 K. The $Mn(Si_{0.99}Ge_{0.01})_{1.75}$ material exhibited the best performance from 300 K to 900 K thanks to its low electrical resistivity and thermal conductivity, obtaining the highest *ZT* of 0.42 at 850 K. The $MnSi_{1.75}$ compound alloyed by ball milling showed similar efficiency to the furnace heating sample from low temperature up to around 650 K. Above 700 K, the ball milled material had better performance, achieving 0.39 at 800 K, which was 20% higher than the corresponding value of the sample prepared in conventional furnace.

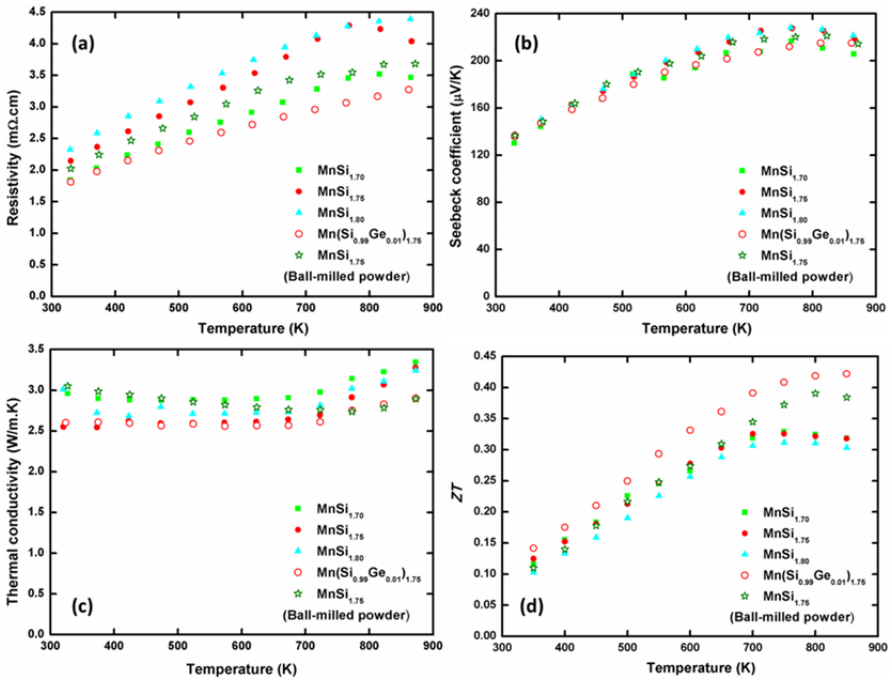

Figure 6.3 Temperature dependence of (a) electrical resistivity, (b) Seebeck coefficient, (c) thermal conductivity, (d) *ZT* of HMS-based materials.

All in all, the HMS material synthesized by mechanical alloying showed better thermoelectric performance than the ones prepared by mechanical mixing and subsequent heat treatment. However, the problem of agglomerations limited the utilization of ball milling for direct synthesis of pure HMS with a desired stoichiometry.

6.3.3 Mechanical milling and reactive spark plasma sintering

The stoichiometric amounts, corresponding to the $MnSi_{1.75}$ composition of the constituent elements, were homogeneously mixed via planetary ball milling using vials and balls made of tungsten carbide. The milling process was carried out with a low ball-to-powder weight ratio of approximately 4:1, a slow rotation speed of 450 rpm, and a short duration of 20 min divided into two rotating periods in reverse directions. The obtained powders were then directly loaded into graphite die for spark plasma sintering (SPS) at 1050ºC for 45 min using a maximum pressure of 28 MPa. For the wet milling, *n*-hexane was directly added into the vials up to just immersing the powder. The mixtures obtained from the wet milling process were, then, dried under the fume hood. All the sintered samples had densities higher than 95% of the theoretical density, which was satisfactory for subsequent physical property measurements considering the error range of the density determinations.

The use of a liquid medium during high energy ball milling was well known to prevent welding between particles during collisions, and decrease the final particle size, which was convenient for our purposes.[167,207] In this case, *n*-hexane was used as milling media due to its availability as well as low boiling point, which helped its removal after the ball milling process. From this point of view, alcohol could also be a good candidate for wet ball milling, which was used by Z. Wang *et al*.,[210] except for the possibility to produce oxides during the process. The ball milling step was carried out under mild conditions (low ball-to-powder weight ratio, slow rotation speed and short milling duration) to avoid the formation of HMS compounds. Therefore, the obtained mixtures consisted of elemental manganese and silicon only. On the contrary, M. Saleemi *et al*.[145] also used balls and vials made of tungsten carbide and obtained a mixture of HMS, MnSi, silicon, and manganese after milling for 8 h at 400 rpm with hexane as dispersion media.

The particle sizes were analyzed using a Malvern's Mastersizer 2000 equipment with deionized water used as the dispersant. The particle size distribution collected on these mixtures by the laser granulometer is presented in Figure 6.4 together with the SEM images for the powders obtained after the milling process. The distribution curve of this sample was

asymmetric with the peak situated at approximately 100 μm showing non-uniform size dispersion, which was in good agreement with the SEM image of the same powder. The calculated surface mean diameter D[3,2], mode value, and median diameter of particles d(0.5) in the dry milling powders were 20.77, 91.20, and 59.86 μm, respectively. The results showed that the particles were partly broken down by the ball milling under soft conditions. On the other hand, the wet-milled sample contained finer and more evenly distributed particles as seen in Figure 6.4 (b). For longer milling durations, Groβ *et al*.[122] obtained a mean grain diameter of 5 μm after 1 h with planetary steel ball mill, and M. Saleemi *et al*.[145] reached the sizes of 50-500 nm after 8 h with tungsten carbide vials and balls, both milled in hexane media. The distribution curve of the wet milling sample was divided into two peaks located at approximately 13 and 100 μm, while the D[3,2], mode values of two peaks, and d(0.5) in the wet milling powders were 10.64, 13.18, 138.04, and 68.25 μm, respectively.. It is remarkable that the sedimentation of the mixture happened in a short time, therefore, the measurements were repeated only twice which might bring extra errors to the measurements. It is difficult to propose any conclusions about the completion of the wet milling process due to the peaks at 100 μm that could be assigned to either single or multiple particles. The inhomogeneous morphology with agglomeration due to wet milling was also reported by other group.[145] However, it is clear that the smaller particle size was achieved by using wet milling as indicated by the presence of the peak at 13 μm.

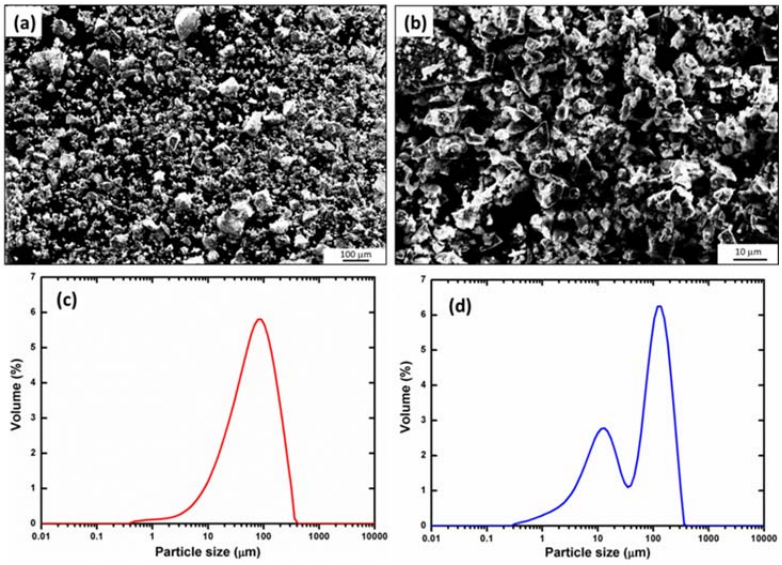

Figure 6.4 SEM images and particle size distribution curves of powders obtained after ball milling process, with (a) and (c): dry milling; (b) and (d): wet milling.

The XRD patterns of the ground powders after the sintering process, given in Figure 6.5, identified the major phase of all samples to be HMS. The materials prepared by dry milling contained impurities of MnSi and Si, while no extra peaks were observed in the one synthesized by wet milling within the detection limit of X-ray analysis. As mentioned in the introduction, various compounds with the Nowotny chimney-ladder structure exist under the HMS appellation. The two subsystems (Si ladder and Mn chimney) have a common tetragonal *a*-axis but different *c*-axis lengths. Consequently, the XRD patterns of these compounds are very similar in both peak positions and intensities. Therefore, a specific compound, defined by the *c*-axis ratio γ, is rarely identified, hence the generic name of HMS is usually used in most of the reports. A profile matching refinement of the XRD data of wet-milled HMS was performed using FullProf software with the pattern of Mn_4Si_7 compound, which was equivalent to the nominal compositions. However, the peak positions between the pattern and the experimental data were not well-fitted, indicating that a different compound might have been obtained. A Le Bail decomposition was carried out using the same software with the two sublattices of Mn and Si elements.[67,81] The following cell parameters were

obtained a_{Mn} = 5.5244 Å, c_{Mn} = 4.3661 Å, a_{Si} = 3.9062 Å, and c_{Si} = 2.5185 Å; therefore, the c_{Mn}/c_{Si} ratio was calculated to be 1.733, corresponding to the $Mn_{15}Si_{26}$ compound. Accordingly, the *a* and *c* parameter were approximately 5.533 Å and 65.4915 Å, which were comparable with a previous report.[114] The reference pattern of $Mn_{15}Si_{26}$, hence, is included in the same figure for comparison.

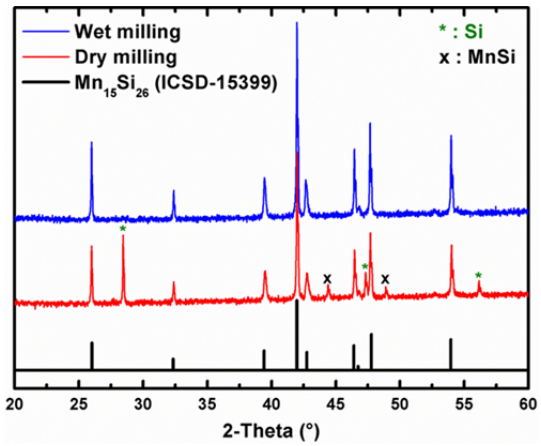

Figure 6.5 XRD patterns of the ground powders after the spark plasma sintering step of dry-milled and wet-milled HMS with the reference pattern of $Mn_{15}Si_{26}$ for comparison.

The fractured surfaces of the consolidated samples were observed by SEM, as presented in Figure 6.6, showing no significant size differences between the starting elements and the final products at these sintering conditions. It is noticeable that the sample prepared by wet milling had a smoother surface and contained less voids than that made by dry milling, this might be attributed to its higher density of 5.06 (more than 97% of theoretical density) than 4.92 (less than 95% of theoretical density). Thus, the smaller particles helped not only to improve the diffusion rate during solid state reaction but also the rearrangement during sintering process. In order to observe the presence and the distribution of the MnSi phase, these samples were chemically etched for 1 min at room temperature using hydrofluoric acid in an aqueous solution (HF (concentrated) : H_2O = 1:1 in volume ratio). A large amount of MnSi striations, which were arranged parallel to each other in a specific

grain, was found in the dry-milled sample; while they were not observed in the wet-milled one. The absence of MnSi secondary phase confirmed again a complete solid state reaction between Mn and Si within the detection limit of electron microscopic technique.

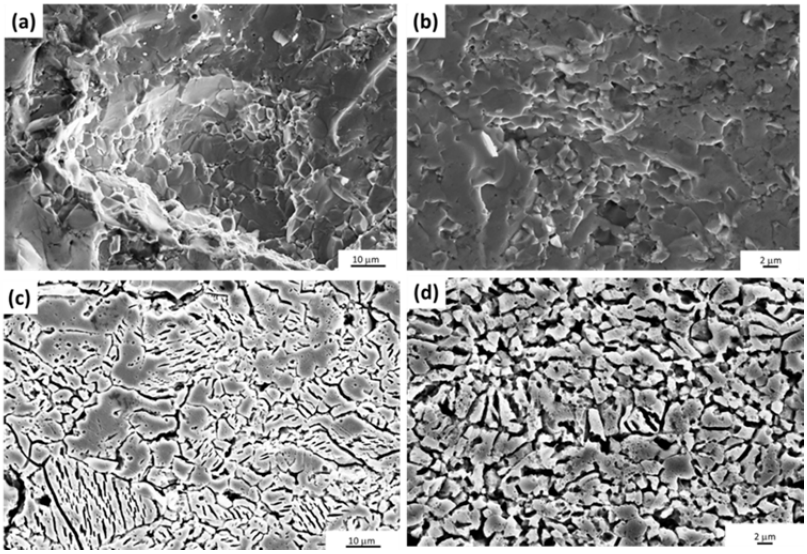

Figure 6.6 SEM images of (a) and (b): fractured surface, (c) and (d): polished and etched surface in consolidated samples after spark plasma sintering step with (a) and (c): dry milling, (b) and (d): wet milling.

The HMS sample synthesized by wet milling showed favorable electrical properties for thermoelectric materials. The temperature dependence of the Seebeck coefficients is given in Figure 6.7 (a), while the evolution of electrical resistivity with elevated temperatures is presented in Figure 6.7 (b). The transport data at 300 K are also shown in Table 6.3. The Seebeck coefficient steadily increased with temperature, then decreased above 800 K. The wet-milled material had superior Seebeck coefficient over the whole temperature range of measurement, reaching a value of 240 μV/K at approximately 800 K. For metals or degenerate semiconductors with parabolic band and energy-independent scattering approximation, the Seebeck coefficient, *S*, is given by

$$S = \frac{8\pi^2 k_B^2}{3eh^2} m^* T \left(\frac{\pi}{3n} \right)^{2/3}$$

where n is the carrier concentration, and m^* is the effective mass of the charge carriers.[6,7] According to the equation, the wet-milled HMS should have lower carrier concentration than the dry-milled one. However, the Hall measurements at 300 K showed the quasi constant values of carrier concentration for the two samples with the same nominal compositions, regardless of whether the reaction was complete or not (a 10% error is generally accepted for this measurement). Therefore, the enhancement of Seebeck coefficient for the microcrystalline wet-milled sample could possibly be also attributed to an energy filtering effect at the grain boundaries.[211] Another, more plausible, reason could be the absence of secondary phase (monosilicide MnSi) in the wet milled sample with low thermoelectric power, degrading the Seebeck coefficient of the material.

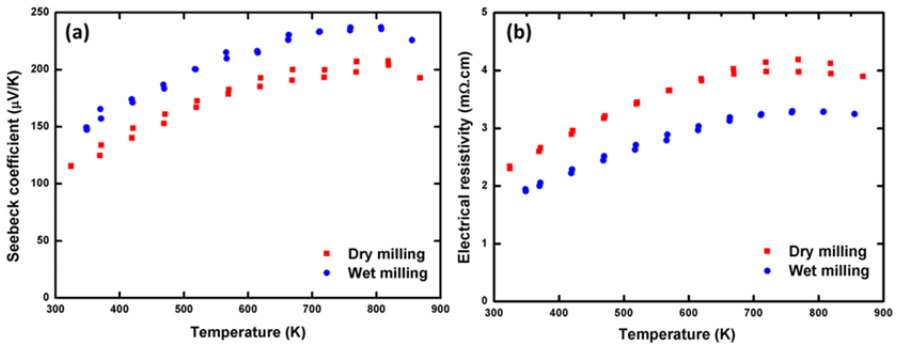

Figure 6.7 Temperature dependence of (a) Seebeck coefficient and (b) electrical resistivity of dry-milled and wet-milled HMS.

Table 6.3 Carrier concentration (n_p), mobility (μ_p), Seebeck coefficient (S), electrical resistivity (ρ) and thermal conductivity (κ) at 300 K of dry-milled and wet-milled HMS.

	n_p ($*10^{21}$ cm^{-3})	μ_p $cm^2 \cdot V^{-1} \cdot s^{-1}$	S ($\mu V/K$)	ρ ($m\Omega.cm$)	κ($W \cdot m^{-1} \cdot K^{-1}$)
Dry-milled HMS	1.45	1.98	108	2.18	4.17
Wet-milled HMS	1.54	2.38	137	1.71	2.99

The electrical resistivity increased with increasing temperature for both samples up to about 750 K, and decreases after this temperature. Combining this observation with the aforementioned evolution of Seebeck coefficient, it can be concluded that the bipolar transport effects were initiated in the temperature range of 700 K – 800 K. The resistivity values of the dry-milled sample were 30% higher than those of the wet-milled one for the whole range of measured temperature. The reduction of electrical resistivity in the wet-milled sample can be explained by the slight improvement of carrier mobility, which was approximately 20% at 300 K as shown in Table 6.3, due to the absence of secondary phases, and its higher density. The carrier concentration of the wet-milled HMS was slightly lower, while its carrier mobility was somehow higher than the reported data for the materials prepared by induction melting,[114] which were 2.09 × 10^{21} cm^{-3} and 1.64 $cm^2 \cdot V^{-1} \cdot s^{-1}$, respectively. This can be attributed to the presence of the metallic MnSi phase in the induction melted sample with high carrier contents and low mobility. Furthermore, Migas *et al.*[94] estimated the carrier concentration of $Mn_{15}Si_{26}$ by *ab initio* calculation to be 2.0 × 10^{21} cm^{-3}, which was slightly higher than our experimental value.

The total thermal conductivity of the wet-milled and dry-milled HMS is shown in Figure 6.8 (a) in comparison with the data from different references. The synthetic conditions of the reference materials are summarized in Figure 6.4. Overall, the wet-milled material had lower thermal conductivity than the dry-milled one with the discrepancy up to 30%. The difference originated from the lattice thermal conductivity (calculated by subtracting the electronic contribution from the total thermal conductivity using the Weidemann Franz law),

contributing to more than 70% of the total value for HMS materials, as illustrated in Figure 6.8 (b). Again, the presence of impurities MnSi and Si in the dry-milled sample with higher thermal conductivity than the HMS matrix can be used to explain for its high thermal conductivity. Another reason can be the small grain sizes of the wet-milled material, contributing to more grain boundaries to scatter phonons, decreasing its lattice thermal conductivity. The total thermal conductivity of the wet-milled HMS was comparable to that of the referenced materials, as shown in the same figure. It is noticeable that the synthetic method used in this report was much faster and more efficient than the ones in those references. Moreover, the materials in the mentioned reports still contained some secondary phases after long time and high energy processes, which was unfavorable for industrial applications.

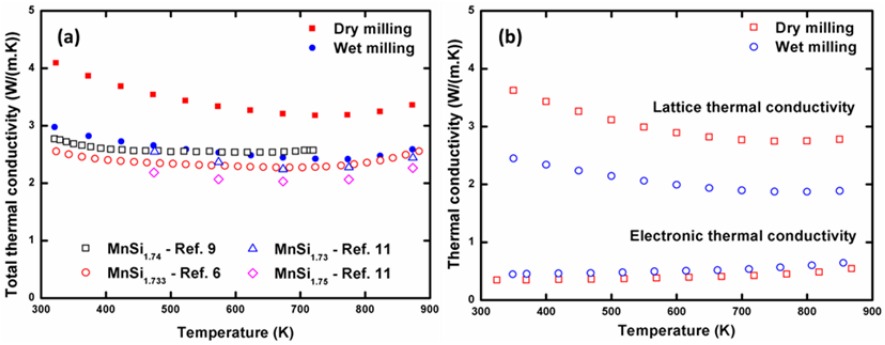

Figure 6.8 Temperature dependence of (a) total thermal conductivity and (b) lattice and electronic thermal conductivity of dry-milled and wet-milled HMS.

Table 6.4 Synthetic conditions, phase compositions, and average grain sizes of the HMS-based materials prepared by different research groups.

Ref.	Synthetic conditions	Phase compositions	Average grain sizes
This work	• Mn and Si powders are dry ball milled using tungsten carbide vials and balls with a ball-to-powder weight ratio	HMS + MnSi	100 μm

	of 4:1, at a rotation speed of 450 rpm for 20 min • Powders are sintered by SPS at 1050 _C for 45 min under a pressure of 28 MPa		
This work	• Same as above except that the ball milling is "wet" as it is performed in presence of hexane	HMS	2 distributions at 13 μm and 100 μm
114	• Powder mixture of $MnSi_{1.733}$ is melted in an induction furnace at 1350ºC for 5 min under argon atmosphere • As-melted ingot is ground in an agate mortar and pestle, and sieved into powders • Powders are hot-pressed at 900ºC for 60 mins in vacuum	$Mn_{15}Si_{26}$ + MnSi	5-50 μm
139	• Mn and Si powders are hand-milled in an agate mortar and pestle to size of under 90 μm • Powder mixture of $MnSi_{1.74}$ is sintered by SPS at 1000ºC for 60 mins under a pressure of 90 MPa	HMS + MnSi + Si	Not mentioned
103	• Powder mixtures of elements are ball-milled using tungsten carbide vials and balls with a ball-to-powder weight ratio of 5:1, at a rotation speed of 500 rpm for 3000 mins	Not mentioned	0.2-0.8 μm

	• Milled powders are sintered at 950ºC for 5 mins under a pressure of 108 MPa		

Figure 6.9 shows the figure of merit *ZT* of the HMS materials prepared by dry milling and wet milling in comparison with the same references used for the thermal conductivity. As a consequence of the thermoelectric properties, the wet-milled sample possessed a higher figure of merit than the dry-milled one over the whole temperature range. It should be precise that the comparisons between these two samples were rather irrelevant due to the compositional differences of the two materials (one was a phase mixture, while the others was a pure phase). Therefore, the thermoelectric performance is shown just to emphasize the efficiency of the wet milling method. Furthermore, from room to moderate temperature (around 550 K), the figure of merit of the sample prepared by hand milling and SPS was higher than that of our wet-milled sample.[139] However, its value decreased rapidly after 550 K and was overcome by our material at higher temperature. On the other hand, the figure of merit of the wet-milled material was superior to all other references with a slightly difference of 10% to the compound with the same stoichiometry synthesized by hard ball milling.[103] The maximum obtained value was 0.55 at 850 K, which is amongst the highest performance for undoped polycrystalline HMS.

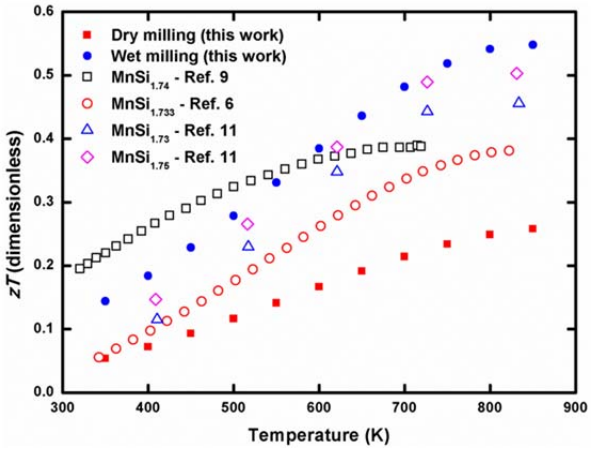

Figure 6.9 Temperature dependence of the thermoelectric figure of merit of dry-milled and wet-milled HMS in comparison with the references.[103,114,139]

6.3.4 Solid state reaction

The stoichiometric amounts, corresponding to the $Mn_{15}Si_{26}$ composition, of the component elements were weighed inside the glove box under argon atmosphere. The powder mixtures were manually mixed in agate mortar and pestle until achieving a fair homogeneity, then sealed in the silica tubes under vacuum. The tubes underwent heat treatments in conventional furnaces at 1000ºC for a total duration of 144 hours, where the tubes were opened every 48 hours for the powder to be re-ground and re-mixed before being put back. The powder diagram of the final product contained tiny peaks of MnSi phase, while Si peak could not be observed within the detection limit of P-XRD (Figure 6.10).

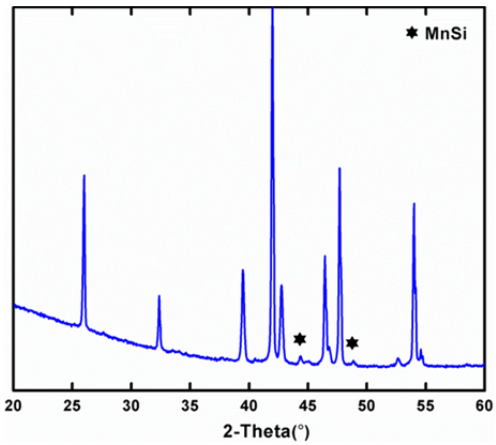

Figure 6.10 P-XRD pattern of $Mn_{15}Si_{26}$ being heat treated in the conventional furnace for 144 hours at 1000ºC.

The $Mn_{15}Si_{26}$ powder was subjected to hot pressing at 1000ºC with different pressure and dwelling time (Table 6.5). The pressing temperature was chosen to be close to the melting point of the compound to ensure that enough thermal energy would be provided for the particles to rearrange. The heating rate was 10ºC/min from room temperature to 1000ºC, while the cooling rate was 4ºC/min down to 400ºC, then the power was turned off and the system was naturally cooled down to room temperature. An increase of the pressure from 54 MPa to 77 MPa (HP03 and HP01, respectively) showed no significant effects on the density, and the sample pressed at high pressure were broken during processing. Different dwelling time at 54 MPa hardly changed the achieved density (HP02, HP03, and HP04), while the pucks obtained after a short duration of 30 minutes also exhibited large cracks on the surface and fell apart during polishing (HP02). Moreover, long pressing time was ineffective to the densification of $Mn_{15}Si_{26}$ material, which was also cost and time consuming (HP04). As a consequence, a pressure of 54 MPa with a dwelling time of 60 minutes at 1000ºC was considered to be the optimal conditions for the $Mn_{15}Si_{26}$ material. The same pressing parameters were applied for another sample, achieving good reproducibility within the experimental error of the density measurements (HP05).

Table 6.5 Hot pressing conditions of $Mn_{15}Si_{26}$ at 1000ºC with the theoretical density of 5.17 g/cm^3.

Sample	Pressure (MPa)	Dwelling time (minutes)	Density (g/cm^3)	Percentage (%)	
HP01	77	60	4.98	96	Sample broken
HP02	54	30	4.90	95	Sample broken
HP03	54	60	5.08	98	
HP04	54	120	4.96	96	
HP05	54	60	4.97	96	

The SEM image on the fracture surface displayed typical grain sizes of 10-30 μm (Figure 6.11 (a)), and the corresponding mapping on the same area showed the Si islands with the sizes ranging from several to tens of microns, which was not revealed in the XRD pattern. The overall compositions were 62 at.-% of Si and 38 at.-% of Mn, which were almost the same as the expected values of 63 at.-% and 37 at.-%, respectively. The EDS analysis performed on different spots in the HMS matrix showed a fairly consistent Mn and Si amounts considering a few at.-% of error (Figure 6.11 (b)).

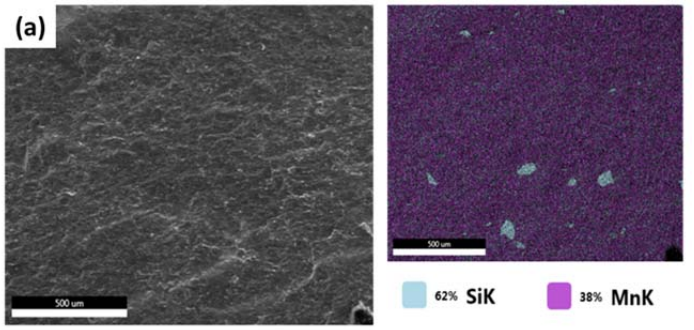

Spot #	Mn (at.-%)	Si (at.-%)
1	43	57
2	42	58
3	36	64
4	42	58
5	38	62

Figure 6.11 (a) SEM image of the fracture surface and the corresponding mapping; (b) EDS analysis on various spots for the $Mn_{15}Si_{26}$ material.

The thermoelectric properties of the $Mn_{15}Si_{26}$ material showed common behavior of a degenerate semiconductor. The electrical resistivity gradually increased from around 1.9 mΩ·cm at 325 K to approximately 3.5 mΩ·cm at about 775 K, then flatted out above this temperature (Figure 6.12 (a)). The Seebeck coefficient also increased from 115 μV/K to 220 μV/K in the same temperature range, and slightly decreased at the temperature more than 775 K (Figure 6.12 (b)). Moreover, the thermal conductivity reduced from around 3.5 $W \cdot m^{-1} \cdot K^{-1}$ to 2.9 $W \cdot m^{-1} \cdot K^{-1}$ in the temperature range of 325 K – 675 K, and slightly increased again to approximately 3.2 $W \cdot m^{-1} \cdot K^{-1}$ at 875 K (Figure 6.12 (c)). Therefore, the bipolar diffusion was anticipated to initiate at around 675 K – 775 K. As a result, the *ZT* attained the maximum value of 0.37 at around 775 K, which decreased at higher temperature (Figure 6.12 (d)). The HP03 and HP05 samples showed reproducible and repeatable thermoelectric performance.

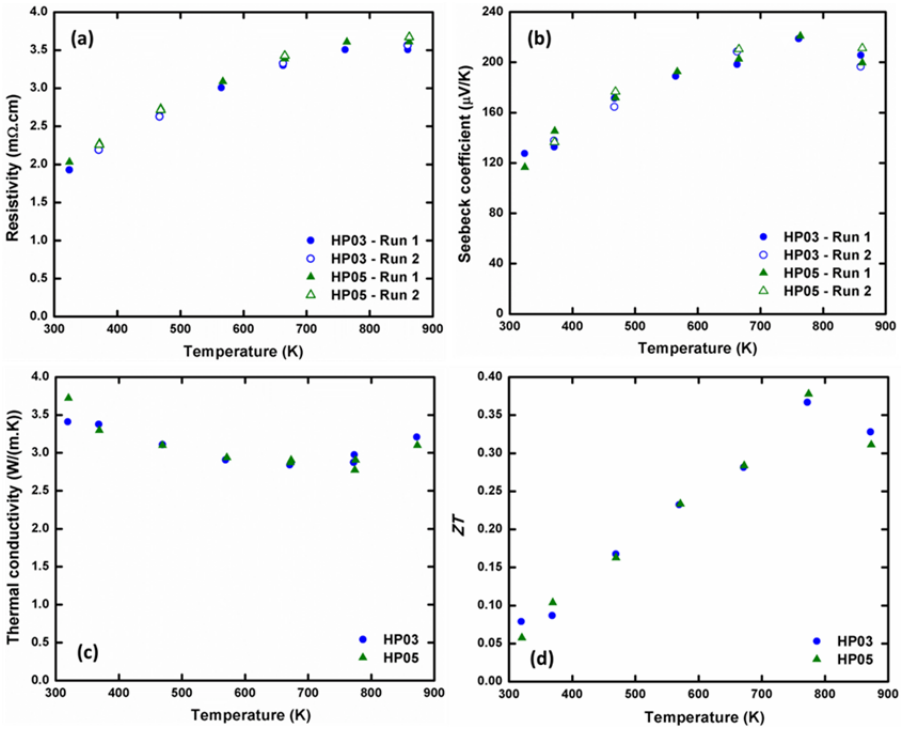

Figure 6.12 Temperature dependence of (a) electrical resistivity, (b) Seebeck coefficient, (c) thermal conductivity, and (d) *ZT* for the HP03 and HP05 samples.

Different HMS materials corresponding to the four most popular formulas were prepared and hot pressed with the same parameters. The compound with the lowest Si/Mn atomic ratio of 1.727 exhibited the highest electrical resistivity and Seebeck coefficient amongst all the structural formulas (Figure 6.13 (a) and (b), respectively). Moreover, the $MnSi_{1.75}$ composition exhibited the lowest resistivity, which might stem from different amounts of side products in these materials with diverse morphologies. Small differences were observed for the Seebeck coefficient, which could be predicted from very close atomic ratios between the formulas. As mentioned in Chapter 2, the filling of the valence band in HMS materials reduced with decreasing the Si/Mn atomic ratios, leading to increasing the carrier concentrations, which was not clearly reflected in the obtained Seebeck coefficient. In fact, there existed no evidence at the moment that different HMS compounds were formed when the corresponding stoichiometry was employed due to very similar P-XRD patterns

achieved. However, it was still believed that the behavior of electrical properties was resulted more from the carrier mobility than from the carrier concentration. The Si-richest compound of $MnSi_{1.75}$ showed the lowest resistivity, ranging from 1.6 mΩ·cm to 2.9 mΩ·cm over the whole temperature range.

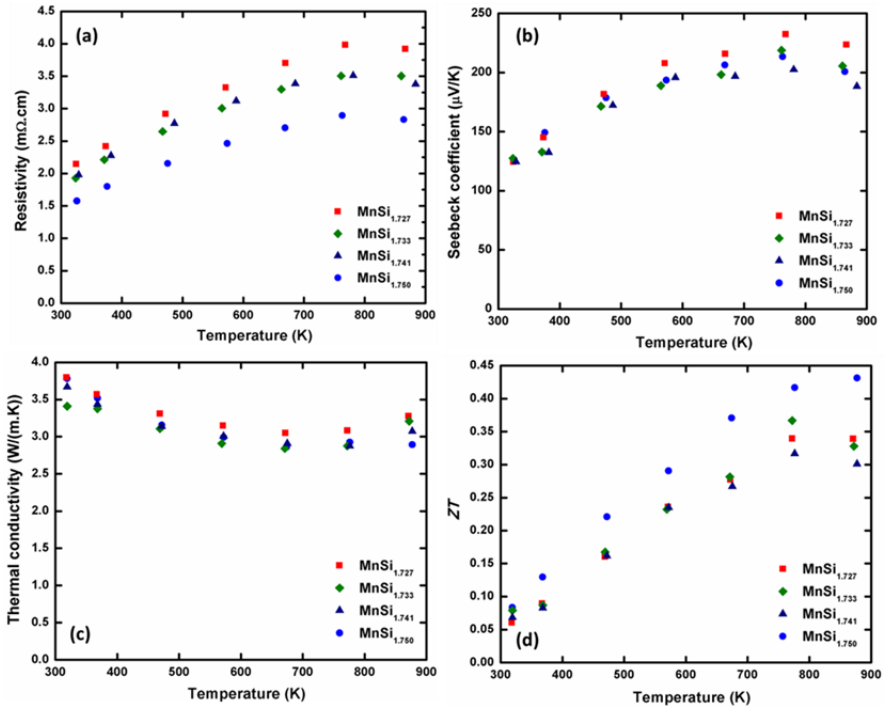

Figure 6.13 Temperature dependence of (a) electrical resistivity, (b) Seebeck coefficient, (c) thermal conductivity, and (d) *ZT* of different HMS structural formulas.

Elemental mapping in the $MnSi_{1.75}$ sample consisted of large agglomerations of Si with the size of around 50 μm (Figure 6.14). The non-uniform distribution of the Si clusters might not interfere with the charge transport in the matrix material on a large scale. The thermal conductivity of all the formulas fell within the experimental error because of no particular scattering centers for phonon created with slightly changing the atomic ratios (Figure 6.13 (c)). Subsequently, the $MnSi_{1.75}$ composition showed the best performance,

reaching a *ZT* of 0.43 at 875 K thanks to its low resistivity, while the other compounds achieved the maximum efficiency of around 0.31 – 0.37 at 775 K (Figure 6.13 (d)).

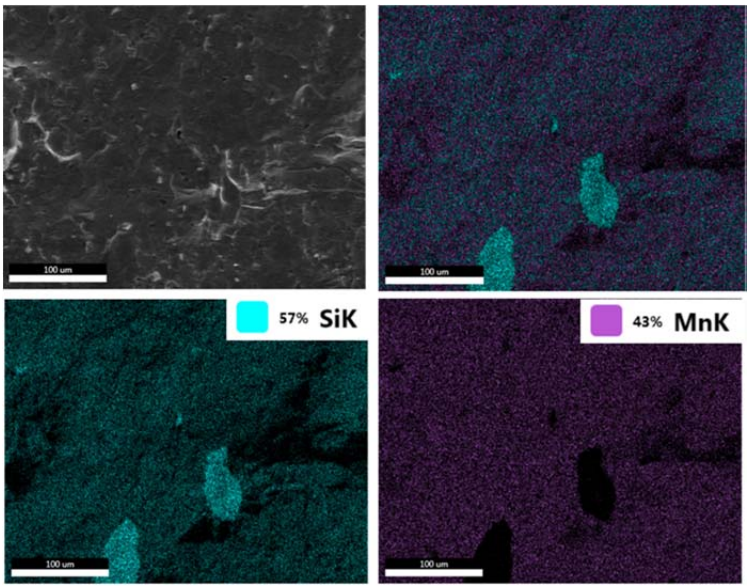

Figure 6.14 Elemental mapping of the $MnSi_{1.75}$ composition, where the expected contents are 64 at.-% of Si and 36 at.-% of Mn.

The solid state reaction for preparing HMS was a very costly and time consuming method, requiring 144 hours at 1000ºC with two intermediate grinding steps. The final product still contained trace amounts of MnSi. A temperature of 1000ºC under a pressure of 54 MPa for 60 minutes was indicated to be the optimal parameters for hot pressing, achieving a high density of more than 96% of the theoretical value, which was also reproducible. The thermoelectric performance of $Mn_{15}Si_{26}$ prepared by this method showed good reproducibility and repeatability, reaching 0.43 at 875 K.

6.3.5 Chemical vapor transport

The sealed tubes containing an amount of about 500 mg of the powder mixtures comprised of the constituent elements and the transport agents were placed inside the tube

furnace. The exact temperature gradient could not be controlled, but the temperature along the tube has been measured at different temperatures so that the temperature difference between the hot and cold sides could be estimated. Because of the uncontrollable temperature gradient, the generated crystals scattered over the whole tube length rather than collected at one side. The crystallization was observed close to the hot side with the usage of $MnCl_2$ as the transport agent, while crystal growth at the cold side was obtained via $CuCl_2$ (Figure 6.15 (a)). The chemical vapor transport using approximately 100 mg I_2 as the transport agent occurred at a slow rate compared to the utilization of chlorides (Figure 6.15 (b)), resulting in small crystals distributed near to the cold side.

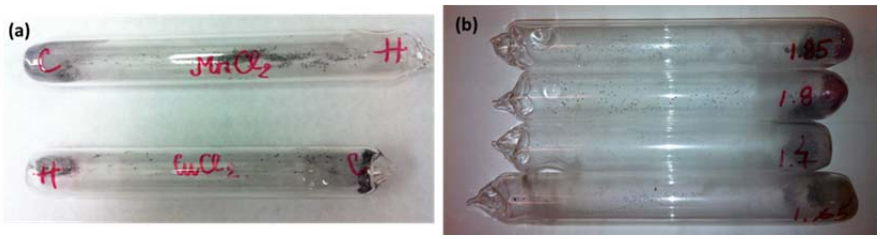

Figure 6.15 The silica tubes after being removed from the furnace (a) using the transport agents of $MnCl_2$ and $CuCl_2$ where the C and H letters imply cold side and hot side, respectively, and (b) transport agent I_2 for the $MnSi_x$ stoichiometry where x was indicated by the numbers written on the tubes.

Various attempts have been made on changing the staring compositions, the transport agents, the setting temperatures, as well as adding some dopants, e.g. Ge or Sn (Table 6.6). The single crystals being carefully selected were characterized using a Bruker single crystal diffractometer employing Mo Kα radiations. The crystals were mounted on a thin quartz tube for the ω-scan to collect the blocks of data.

Table 6.6 A summary of different transport conditions, where the temperature gradient was approximately 50ºC - 60ºC with a duration of 19 days.

Composition	Transport agent	Furnace temperature
$MnSi_x$ (x = 1.65, 1.70, 1.727, 1.741, 1.75, 1.80, 1.85)	I_2	900ºC
$MnSi_{1.75}$	$CuCl_2$	900ºC
$MnSi_{1.75}$	$MnCl_2$	900ºC
$Mn(Si_{1-y}X_y)_{1.75}$ (X = Ge, Sn; y = 0.01, 0.02)	I_2	900ºC
$MnSi_x$ (x = 1.65, 1.75, 1.85)	I_2	800ºC
$MnSi_{1.75}$	$MnCl_2$	800ºC

The collected data were subjected to refinements to achieve the unit cell. The reciprocal lattice was the same for all the cases, showing a tetragonal crystal system (Figure 6.16). Even though overnight scans have been performed on different crystals, the resolution was still too low for the superstructure reflections to be observed. This might be due to the bad qualities of the obtained crystals.

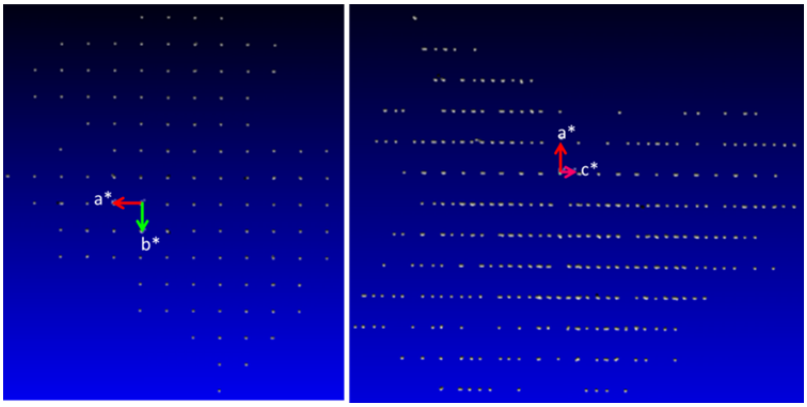

Figure 6.16 The reciprocal lattice obtained from single crystal XRD.

As a consequence, all the crystals were identified as Mn_4Si_7, which was different to the previous reports, and no cooperation of the dopants could be indicated (Table 6.7). The

residual factor R1 and the weighted residual factor wR2 were lower than the acceptable values of 5% and 10%, respectively, indicating good fits.

Table 6.7 Results of single crystal XRD.

Chemical formula	Mn_4Si_7
Formula weight ($g \cdot mol^{-1}$)	416.39
Measurement temperature (K)	296
Radiation type	Mo K_α
Crystal system, space group	Tetragonal, *P*-4*c*2
a, *b* (Å)	5.5257(4)
c (Å)	17.5097(15)
V ($Å^3$)	534.63(7)
Z	4
R1	0.018
wR2	0.047

Obviously, more precise characterizations need to be done before any conclusions on the crystal identifications could be drawn. The low yield of the method limited its expansion for producing on an industrial scale. However, if all the reaction parameters could be well controlled, chemical vapor transport would be very useful for investigations at a laboratory level, especially for obtaining unknown structural formulas in the HMS system.

6.4 Conclusions

Various methods for preparing HMS-based materials have been thoroughly investigated, including mechanical alloying, mechanical milling and furnace heating, ball milling and reactive spark plasma sintering; solid state reaction, and chemical vapor transport. The alloying process using ball milling of HMS suffered from the agglomerations on the inside walls of the vials and around the balls, especially for silicon, leading to low yield and possible loss of stoichiometry. Alternatively, a ball milling under soft conditions in combination with heat treatments in conventional furnace preserved the compositions of the powder mixtures, but took longer time and resulted in HMS materials containing side products, e.g. MnSi and Si. The $Mn(Si_{0.99}Ge_{0.01})_{1.75}$ compound with the maximum *ZT* of 0.42 at 850 K has been synthesized by this method.

Moreover, the traditional solid state reaction to synthesize the HMS-based materials was very time-consuming, taking 144 hours at 1000ºC with twice of intermediate grindings, and still consisting of the side products. The $Mn_{15}Si_{26}$ compound preparing via solid state reaction showed reproducible and repeatable physical properties, achieving a *ZT* of 0.43 at 875 K. Generally, it is believed that HMS-based materials with better efficiency could be obtained if the undesired side products can be eliminated.

Chemical vapor transport was employed to grow single crystals of HMS phases under different conditions using various transport agents. All the obtained crystals were identified as Mn_4Si_7, which was anticipated that the low resolution of single crystal XRD as well as the bad qualities of the samples led to hinder the superstructure reflections. The small yield of the method also limited its applications for industrial productions.

On the other hand, pure HMS without any secondary phase has been synthesized by a facile, effective, and scalable process. By simply adding *n*-hexane into the ball milling step, finer particle sizes were achieved, which helped to enhance the solid state reaction rate by the following spark plasma sintering step, leading to a complete reaction between manganese and silicon to form HMS. The wet milling material was determined to be free from secondary phases within the detection limit of our characterization methods. The sample prepared by

wet milling showed a better thermoelectric performance, with 20% higher Seebeck coefficients, 23% lower electrical resistivity, and 30% lower thermal conductivity than the one synthesized by dry milling for the whole temperature range. Based on these preliminary results, this method is very encouraging for applications in industry. Efforts are on the way to dope and composite HMS by the same process, as well as to investigate their structural evolutions at elevated temperature.

Chapter 7

Structural evolutions at elevated temperature studied by synchrotron radiations of HMS-based materials

Abstract

HMS-based materials including the ones with different Si/Mn atomic ratios and various dopants, e.g. Ge, Al, Cr, and Mo, have been prepared using ball milling in *n*-hexane, followed by reactive spark plasma sintering. The evolution of average structural formulas upon heating up from room temperature to high temperature was investigated using synchrotron radiation and Le Bail refinements, where the peaks in the powder diagram of the HMS superstructure were fitted to the corresponding ones for the Mn and Si sublattices, to extract the lattice parameters and calculate the Si/Mn atomic ratios.

The average structural formula for the undoped HMS materials at room temperature could be identified as $Mn_{15}Si_{26}$, where traces of MnSi and Si were found to affect the temperature dependence of the Si/Mn atomic ratio. The $Mn_{15}Si_{26}$ phase either decomposed into $Mn_{27}Si_{47}$ and MnSi, or reacted with MnSi or Si to yield $Mn_{11}Si_{19}$ or $Mn_{27}Si_{47}$, respectively, at high temperature, if a sufficient amount of the MnSi and Si existed in the starting materials.

The average structural formula at room temperature and its temperature dependence were strongly impacted by the nature of dopants. With Ge substitutions at the Si sites, the structural formula at room temperature was $Mn_{11}Si_{19}$, which decomposed into $Mn_{15}Si_{26}$ and MnSi above 773 K. However, the Al substitutions at the Si sites maintained the average structural formula of HMS materials at room temperature to be $Mn_{15}Si_{26}$, which converted into $Mn_{11}Si_{19}$, MnSi, and Si in the temperature range of 473 K – 673 K. Similarly, the $Mn_{15}Si_{26}$ formula could be assigned for the Cr-doped HMS materials at room temperature, which gradually transformed towards the $Mn_{27}Si_{47}$ and MnSi phases at the temperature more than 873 K. With Mo substitutions at the Mn sites, the $MoSi_2$ phase was observed in the

powder diagrams due to the low solubility of Mo in the HMS matrix. The large increase of the c_{Si} parameter led to a small decrease of the Si/Mn atomic ratio falling in between the $Mn_{11}Si_{19}$ and $Mn_{15}Si_{26}$ compositions at room temperature.

Furthermore, physical property measurements on the $MnSi_{1.75}$ compound revealed that a correlation between the thermoelectric properties and the average structural formula of bulk HMS-based materials could be expected.

7.1 Introduction

Various attempts have been carried out to identify the exact phases of HMS, mainly using either XRD,[68,98,212] Weissenberg photography,[106,110] transmission electron microscopy (TEM)[104] or selected area diffraction (SAD) with high-resolution transmission electron microscopy (HRTEM).[67,69,70,95,105,140,200,213–217]

Among different characterization methods, the TEM-related techniques were the most efficient and reliable ways to identify the actual structures of incommensurate Higher Manganese Silicide phases. However, the high cost and long painful specimen preparation and imaging durations limited their applications to mostly thin films,[214,215] precipitates,[215] single crystal,[140] or nanowires.[67,213,216–218] The Weissenberg photography was effectively used for HMS single crystals' local structure,[106,219] but the indexation was somewhat laborious, especially for the large unit cell crystals, such as $Mn_{15}Si_{26}$ or $Mn_{27}Si_{47}$.

On the other hand, physical properties of bulk materials depend more on their average structure than on the local structural orders. As aforementioned, various compounds of HMS possess the same tetragonal crystal structures with similar *a* parameter and different lengths of the *c* axis. Therefore, their XRD patterns are very close in both peak positions and intensities. Consequently, a specific compound was rarely identified; hence the generic name of HMS was usually used in most of the reports for indexing.

Miyazaki *et al*.[81,84] have described the crystal structure of HMS material by means of the (3 + 1)-dimensional superspace group approach. Consequently, all the HMS formulas can be treated as a single compound $MnSi_{\gamma}$, where the [Mn] and [Si] subsystems with the three-

dimensional space groups of $I4_1/amd$ and $P4/nnc$, respectively, were employed as initial structural models. Lately, this model has been used to extract the lattice parameters, a, c_{Mn}, c_{Si}, and γ, for the $(Mn_{1-x}Cr_x)Si_\gamma$ and $(Mn_{1-x}Cr_x)Si_\gamma$ solid solutions,[124,138] as well as for a $MnSi_\gamma$ incommensurate composite crystal at high temperature.[102] Here, the [Mn] and [Si] sublattices were applied to refine the sublattice parameters, from which γ can be calculated, allowing the average structural formulas for different HMS-based materials at room temperature and upon heating to be predicted.

7.2 Experimental section

The stoichiometric amounts of the constituent elements, all purchased from Alfa Aesar, as followed: Mn powder, 99.95%, -325 mesh; Si powder, crystalline, 99.9%, -100 mesh; Ge powder, 99.999%, -100 mesh, Al powder, 99.8%, -40 + 325 mesh; Cr powder, 99.99%, -100 + 325 mesh; Mo powder, 99.95%, APS 3–7 micron, were homogeneously mixed via planetary ball milling using vials and balls made of tungsten carbide in *n*-hexane media. The obtained powders (after being dried under the fume hood) were, then, directly loaded into graphite die for SPS at 1050°C in 45 minutes using a maximum pressure of 28 MPa.

The pucks produced from the SPS process were broken down and ground into fine powders for *in situ* P-XRD at the beamline ID22 of the European Synchrotron Radiation Facility (ESRF, Grenoble, France) using an incident wavelength of 0.400025(5) Å. The Le Bail refinement of the diffraction data were, then, performed using FullProf Suite 2.05. All the reference data were taken from Inorganic Crystal Structure Database (ICSD).

7.3 Results and discussions

7.3.1 Different Si/Mn atomic ratios

The combination of wet ball milling and spark plasma sintering was a simple, effective and scalable process to synthesize HMS-based materials for industrial applications, as previously demonstrated.[200]

The XRD patterns of all the $MnSi_x$ samples (x = 1.65, 1.70, 1.75, 1.80, and 1.85) after sintering, presented in Figure 7.1 (a), showed the main phase to be HMS, appeared as non-labeled peaks, with the presence of some side products, such as manganese monosilicide, MnSi, or unreacted elemental silicon, depending on the atomic ratios between silicon and manganese. As expected from the Mn-Si phase diagram,[218,219] the materials with deficient silicon amounts (x = 1.65, 1.70) contained HMS and MnSi, while the ones with excessive silicon contents (x = 1.80, 1.85) consisted of HMS and silicon. The material with a stoichiometry of $MnSi_{1.75}$ appeared as pure HMS within the detection limit of our conventional X-ray analysis instrument, which is a Phillips X-Pert Pro Panalytical diffractometer with a Cu $K_{\alpha1}/K_{\alpha2}$ radiation (λ = 1.540598 Å, 1.544426 Å), as described in an earlier publication.[220] However, tiny peaks of silicon were revealed in the pattern recorded by synchrotron radiation thanks to the high intensity and resolution of the X-ray source, as well as the fact that the background, which was usually present in lab-scale X-ray spectrum using Cu radiations for Mn-containing samples, was almost eliminated by selecting an appropriate wavelength (Figure 7.1 (b)). A similar observation has been reported by Girard *et al.*[140] for the undoped HMS sample of the $MnSi_{1.73}$ composition prepared by solid state reaction.

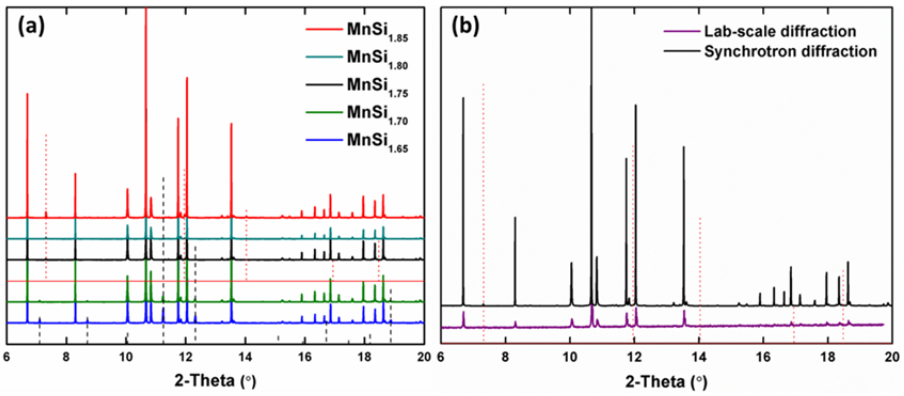

Figure 7.1 P-XRD patterns at room temperature of (a) $MnSi_x$ (x = 1.65, 1.70, 1.75, 1.80, and 1.85) materials, and (b) $MnSi_{1.75}$ by Cu radiation from a lab-scale diffractometer, and synchrotron radiation; the non-labelled peaks belong to HMS phases, the dotted line

represents the silicon phase (ICSD-29287), and the dashed line represents the MnSi phase (ICSD-643641).

Le Bail refinements were performed by fitting the corresponding peaks of Mn and Si sublattices to the whole XRD pattern, illustrated in Figure 7.2 (a) for the $MnSi_{1.75}$ composition, to obtain the lattice parameters and calculate the Si/Mn atomic ratio, from which the average structural formula can be predicted. Generally, the Mn and Si sublattices contributed to form the corresponding reflections in the diffraction patterns of HMS compounds, where the peak indices depended on the stacking multiplications of the superstructures, e.g. (0 1 15), (1 2 15), (1 1 30), or (0 3 15), and (1 1 26) for the reflections induced from the Mn and Si sublattices, respectively, in the $Mn_{15}Si_{26}$ compound (Figure 7.2 (b)). Through fitting the experimental diffraction patterns with the simulated sublattices of Mn and Si, the superstructure reflections of HMS-based materials were reversely decomposed into those of the sublattices to achieve the corresponding lattice parameters.[81]

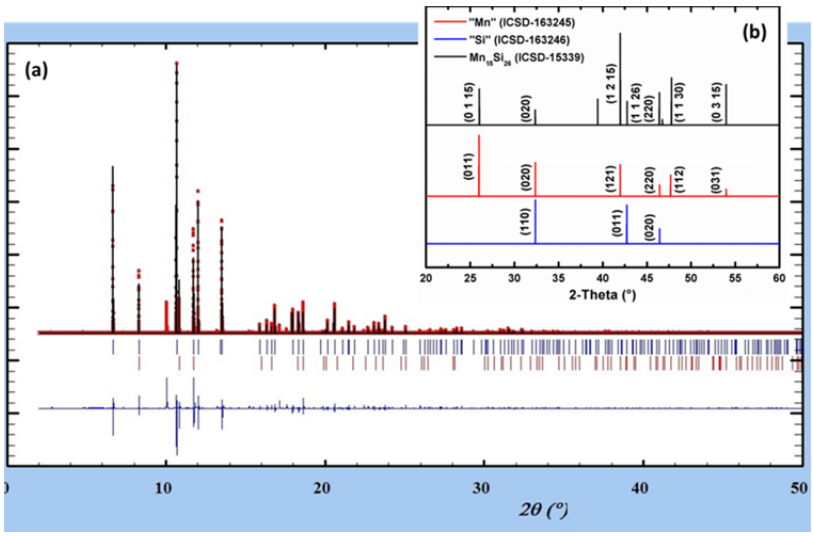

Figure 7.2 (a) Le Bail refinement of $MnSi_{1.75}$ composition at room temperature; (b) Illustration of Le Bail refinement through fitting the corresponding peaks of Mn and Si sublattices to the XRD pattern of the $Mn_{15}Si_{26}$ superstructure.

The results of the refinements for various $MnSi_x$ compositions are given in Table 7.1 in comparison to those of the $MnSi_{1.75}$ compound using Cu K_α radiation. The fitting of the diffraction pattern from a lab-scale diffractometer for the sample with the $MnSi_{1.75}$ stoichiometry resulted in slightly lower cell parameters with higher standard deviations due to broadening peaks and rough backgrounds. However, the c_{Mn}/c_{Si} ratio was nearly identical for the cell parameters refined from the patterns obtained from a conventional diffractometer and the synchrotron, proposing that a conventional X-ray source can still be a potential replacement for determining the average structure of polycrystalline HMS.

Table 7.1 Le Bail refined subcell parameters from XRD patterns at room temperature of the $MnSi_x$ (x = 1.65, 1.70, 1.75, 1.80, and 1.85) materials using synchrotron radiation and of the $MnSi_{1.75}$ composition using Cu K_α radiations.

Nominal compositions	a_{Mn} (Å)	c_{Mn} (Å)	a_{Si} (Å)	c_{Si} (Å)	$\gamma = c_{Mn}/c_{Si}$
$MnSi_{1.65}$	5.52567(1)	4.36723(1)	3.90745(2)	2.52087(2)	1.73243(1)
$MnSi_{1.70}$	5.52759(1)	4.36868(1)	3.90797(6)	2.51989(4)	1.73368(3)
$MnSi_{1.75}$	5.52730(1)	4.36843(1)	3.90853(1)	2.52161(1)	1.73240(1)
$MnSi_{1.80}$	5.52677(1)	4.36755(1)	3.90866(4)	2.51896(3)	1.73387(2)
$MnSi_{1.85}$	5.52832(1)	4.36855(1)	3.90975(3)	2.51893(3)	1.73429(2)
$MnSi_{1.75}$ (Cu K_α radiation)	5.52441(34)	4.36611(30)	3.90622(43)	2.51848(42)	1.73363(31)

The a_{Si} parameter at room temperature steadily increased with increasing the Si/Mn atomic ratios from 1.65 to 1.85, while the c_{Si} length varied in a more complex way, where the $MnSi_{1.75}$ material possessed the longest size of 2.5216 Å comparing to the materials containing deficient and excessive silicon amounts. This led to its lowest γ value of 1.7324 in

the series, while the other c_{Mn}/c_{Si} ratios showed very slightly differences probably falling into the error range of the refinement.

The refined parameters of the Mn and Si sublattices for the $MnSi_{1.75}$ compound exhibited a linear relationship with the temperature in the range from 300 K to 900 K (Figure 7.3). The a_{Mn}, c_{Mn}, and a_{Si} lengths gradually expanded around 0.6% for the whole temperature range, i.e. from 5.5273, 4.3684, and 3.9085 Å at 298 K to 5.5603, 4.3926, and 3.9317 Å at 873 K, respectively. On the other hand, the c_{Si} parameter was enlarged approximately 0.4% from 2.5216 Å at 298 K to 2.5328 Å at 873 K due to particular interactions between Si atoms along this direction. Typically, the residual standard errors of the linear fitting, i.e. the adjusted R-square values, were more than 98% for all the cases of a_{Mn}, c_{Mn}, a_{Si}, and c_{Si}.

Recently, Kikuchi *et al.*[102] have performed *in situ* high temperature P-XRD on the polycrystalline $MnSi_{\gamma}$ ($\gamma \sim 1.7$) samples prepared in an arc-melting furnace from 298 K to 1253 K. The extracted data from that publication were included in Figure 7.3 for a comparison. There, the refined a_{Mn} and c_{Mn} parameters increased also linearly with increasing the temperature, while an abrupt change of the c_{Si} size was indicated above 773 K, where the temperature coefficient was nearly tripled reaching 8.4×10^{-5} Å·K^{-1}. The refined parameters of the Mn sublattice were fairly comparable between the $MnSi_{1.75}$ composition and the reference $MnSi_{\gamma}$ material from 300 K to 900 K, where the temperature coefficients from the other group were 13% and 29% higher than our HMS material for a_{Mn} and c_{Mn}, respectively. However, the c_{Si} length of the reference sample was slightly lower than that of the $MnSi_{1.75}$ material over the whole temperature range, where the temperature dependences were 50% higher and 4.6 times larger below and above 773 K, correspondingly, in comparison to this work. The differences might stem from the stoichiometric compositions as well as the experimental conditions. It could be noticed that the X-ray measurements of Kikuchi *et al.*[102] were carried out using Cu K_{α} radiations, which could possibly introduce a larger background to the patterns of the samples containing Mn due to the fluorescence effect.

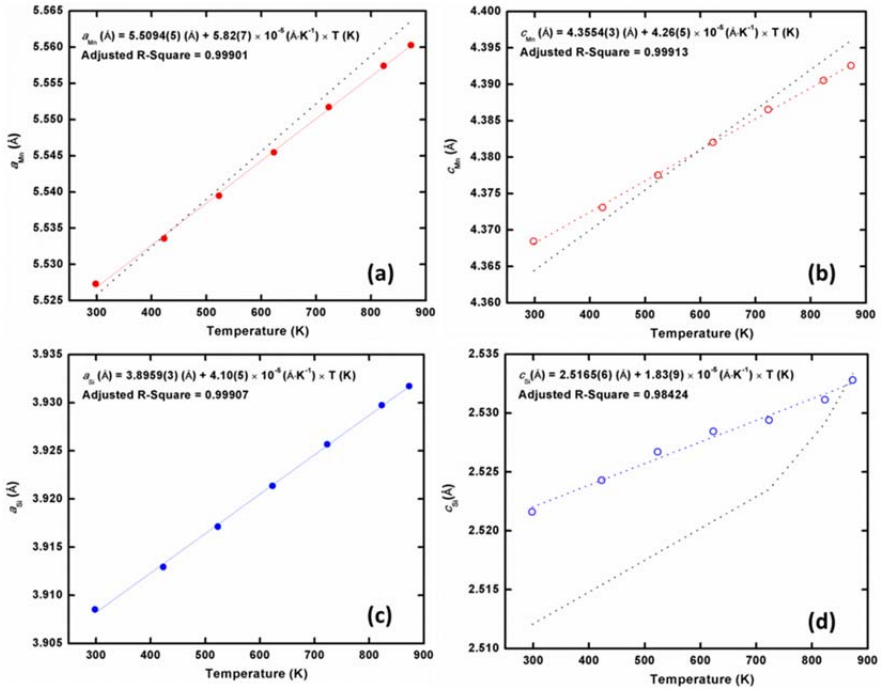

Figure 7.3 Temperature dependence of refined parameters of the Mn and Si sublattices, (a) a_{Mn}, (b) c_{Mn}, (c) a_{Si}, and (d) c_{Si}, for the $MnSi_{1.75}$ composition, where the dotted black lines represent the reference data.[102]

Consequently, the subcell volumes steadily developed from 300 K to 900 K, where the developments could be well-fitted to a linear behavior (Figure 7.4). Due to comparable a_{Mn} and c_{Mn} parameters, the volume of the Mn subcell, V_{Mn}, was very similar for the $MnSi_{1.75}$ and $MnSi_{\gamma}$ materials, where the temperature coefficient of the reference was around 18% higher than that of our sample. The temperature dependence of the sublattice parameters and volumes was then used to calculate the linear and volume thermal expansion coefficients of HMS-based materials.

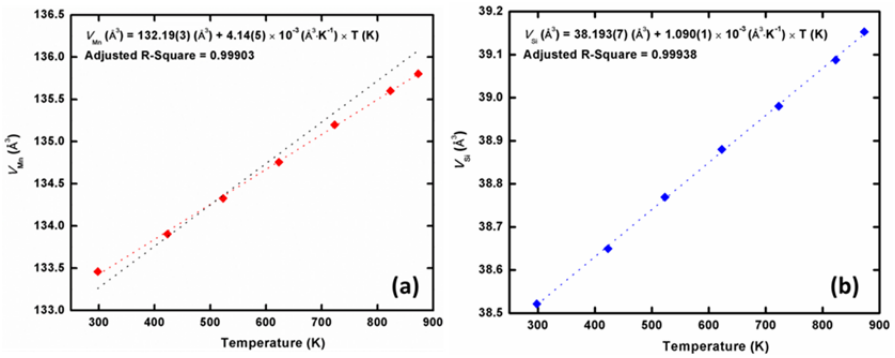

Figure 7.4 Temperature dependence of the unit cell volume of the (a) Mn and (b) Si sublattices for the $MnSi_{1.75}$ composition, where the dotted black lines represent the reference data.[102]

The linear and volume thermal expansion coefficient, α and β, respectively, at a given temperature, T, could be calculated from the temperature dependence of the refined lattice parameters, using the following formulas, where l is either the a_{Mn}, c_{Mn}, a_{Si}, or c_{Si} parameter, and V is the volume of the subcells of Mn or Si.

$$\alpha = \frac{1}{l_T} \times \frac{dl}{dT}$$

$$\beta = \frac{1}{V_T} \times \frac{dV}{dT}$$

The experimental thermal expansion coefficients at room temperature obtained from the $MnSi_{1.75}$ material prepared through soft ball milling in *n*-hexane and reactive spark plasma sintering are given in Table 7.2 comparing to the $MnSi_{\gamma}$ reference synthesized in an arc-melting furnace and the values estimated from an empirical approach for various HMS compounds. The linear thermal expansion coefficients along the a_{Mn} and a_{Si} axes were identical and slightly higher than those along the *c*-axis for both Mn and Si sublattices. Surprisingly, the expansion along the c_{Si} axis was the lowest one even though the interactions between Si pairs in this direction were weaker than those between the Mn atoms. The calculated values were quite close to the data achieved from Kikuchi *et al.*,[102] considering the

error ranges, where the thermal expansion coefficient along c_{Si} was also the minimum amongst all the linear expansion coefficients, which was 47% higher than this work. The α coefficients of the $MnSi_{1.75}$ composition were slightly higher than those approximately calculated from the cohesive energy of different HMS compounds from the report of Allam *et al.*[221]. Considering the fact that the linear thermal expansion coefficients attained the highest values in $Mn_{15}Si_{26}$, it could be anticipated that the average structural formula in the $MnSi_{1.75}$ composition was closer to this compound than the actual stoichiometry of Mn_4Si_7.

Table 7.2 Linear and volume thermal expansion coefficient for the $MnSi_{1.75}$ composition at room temperature in comparison to the references.[102,221]

	α (a_{Mn}) ($\times 10^{-6}$ K^{-1})	α (a_{Si}) ($\times 10^{-6}$ K^{-1})	α (c_{Mn}) ($\times 10^{-6}$ K^{-1})	α (c_{Si}) ($\times 10^{-6}$ K^{-1})	β (V_{Mn}) ($\times 10^{-6}$ K^{-1})	β (V_{Si}) ($\times 10^{-6}$ K^{-1})
This work	10.5(1)	10.5(1)	9.8(1)	7.3(4)	31.0(4)	28.30(3)
[102]	11.95(2)		12.60(2)	10.71(5)	36.64(2)	-
[221]	6.861 (Mn_4Si_7) 6.976 ($Mn_{11}Si_{19}$) 6.984 ($Mn_{15}Si_{26}$) 6.978 ($Mn_{27}Si_{47}$)		8.326 (Mn_4Si_7) 8.340 ($Mn_{11}Si_{19}$) 8.353 ($Mn_{15}Si_{26}$) 8.346 ($Mn_{27}Si_{47}$)		-	-

The temperature evolution of the XRD patterns for the $MnSi_{1.75}$ material from room temperature to 873 K is shown in Figure 7.5, where the focuses on the major peak positions of the side products, i.e. Si and MnSi, are given in Figure 7.5 (b1) and (b2), respectively. The expansion of the structure with increasing temperature resulted in a systematic shift of the peaks to the lower diffraction angles. No significant changes could be observed for the peak of Si side product, while a tiny peak of MnSi phase appeared at 873 K. This peak was hardly noticeable, which could be easily missed out if the background was rough, and its appearance indicated phase decomposition, possibly leading to the formation of a different average

structural formula for HMS. Kikuchi *et al.*[102] have also noticed a similar peak shift and the presence of the MnSi phase above 773 K, where the discrepancy of temperature to this work might come from the particular stoichiometry of the sample as well as the heating profile. However, Allam *et al.*[98] reported a stable quantity of MnSi and Si from room temperature up to 1093 K and 1133 K in the $Mn_{38}Si_{62}$ and $Mn_{34}Si_{66}$ samples, respectively. Perhaps the intensity of the peak corresponding to the MnSi and Si phase when it just appeared was too small to be distinguished from the present amount of the MnSi side product and the unreacted elemental Si in these samples.

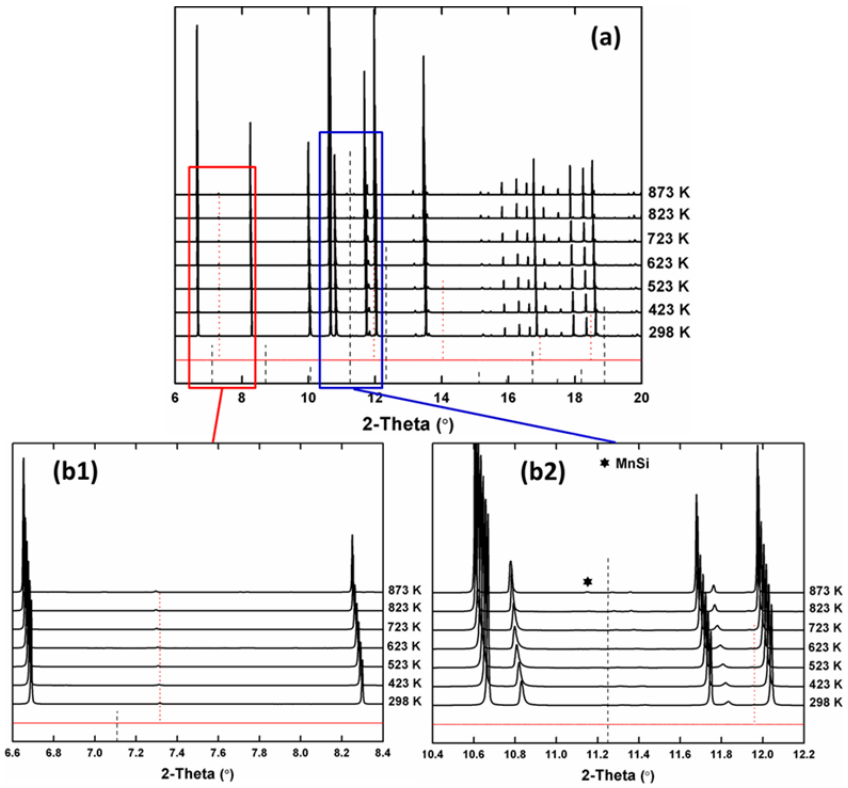

Figure 7.5 (a) XRD patterns for the $MnSi_{1.75}$ composition upon heating up from room temperature to 873 K; (b1 and b2) Partial XRD patterns showing the most intense peaks of Si and MnSi, respectively; the dotted line represents the silicon phase (ICSD-29287), and the dashed line represents the MnSi phase (ICSD-643641).

The temperature dependence of the Si/Mn atomic ratio, equaling γ, is presented in Figure 7.6 for the $MnSi_{1.75}$ sample, where different structural formulas of HMS phases were also shown for illustrations, in comparison to the polycrystalline $MnSi_{\gamma}$ material of Kikuchi *et al.*[102]. The γ value was fairly constant from room temperature up to 523 K, slightly increased at higher temperature reaching the maximum of approximately 1.7346 at 823 K, then decreased again above that. The γ value at room temperature of the $MnSi_{1.75}$ composition was between that of the $Mn_{26}Si_{45}$ and $Mn_{15}Si_{26}$ compounds, crossing the later formula line at around 623 K to get close to the $Mn_{19}Si_{33}$ composition at higher temperature. Considering that the $Mn_{26}Si_{45}$ and $Mn_{19}Si_{33}$ compositions have never been identified in bulk HMS materials, the decomposition into MnSi and $Mn_{27}Si_{47}$ for the $MnSi_{1.75}$ sample could be expressed in the reaction equation:

$$20\ Mn_{15}Si_{26} \rightarrow 3\ MnSi + 11\ Mn_{27}Si_{47}$$

Nevertheless, it should be mentioned that there might be a mixture of different HMS phases in the $MnSi_{1.75}$ materials, e.g. $Mn_{15}Si_{26}$ and $Mn_{26}Si_{45}$, due to the deviation of the γ values from a precise composition, e.g. $Mn_{15}Si_{26}$. Consequently, the use of average structural formulas for the HMS-based materials will possibly be useful for the explanations of the physical properties on a macroscopic scale.

Kikuchi *et al.*[102] also indicated a constant γ value from room temperature up to 773 K, which was higher than the atomic ratio in this work due to the lower c_{Si} length obtained from their sample. This ratio gradually decreased in a linear behavior above 773 K, where the bipolar diffusion was usually initiated in HMS materials. Interestingly, similar observations could be achieved in our $MnSi_{1.75}$ sample, signified from the maximum Seebeck coefficient at slightly below 800 K, superposed in the same figure.

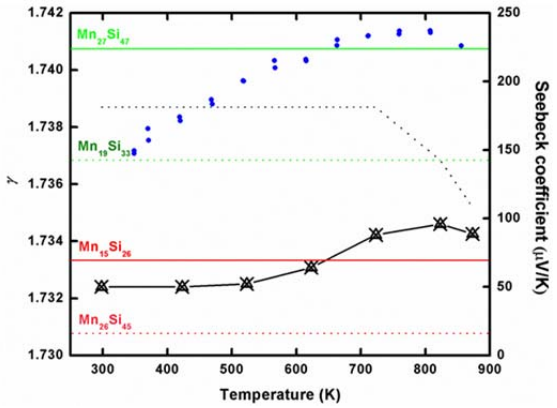

Figure 7.6 Temperature dependence of γ and the Seebeck coefficient (solid circles) for the $MnSi_{1.75}$ composition, where the dotted black line represents the reference data,[102] the horizontal lines represents different structure formulas of HMS with the known (solid lines) and unknown (dotted lines) crystallographic data.

The refined room temperature Si/Mn atomic ratios of the $MnSi_x$ series (x = 1.65, 1.70, 1.75, 1.80, 1.85) are reported in Figure 7.7. At room temperature, the average structural formula of all the compositions could be identified as $Mn_{15}Si_{26}$ containing different side products. Allam *et al*.[98], however, identified the HMS phase stable at room temperature to be $Mn_{27}Si_{47}$ by comparing the angular difference between the peak at 2θ = 43º and its previous one to that of the reference HMS phases, which was in agreement with a later work of Kikuchi *et al*.[102]. The samples used in these investigations have been annealed or remelted several times to reach the equilibrium state, while the materials in this work were synthesized under non-equilibrium conditions. Several maximum and minimum of γ could be recognized over the studied temperature range, which might correspond to several phase transitions. However, the presence of the side products in the starting materials made it hard to propose a transition equation for these compounds. An interesting observation is that these transformations might be irreversible, because the refined γ values for the cooling down process, which was getting closer to the $Mn_{27}Si_{47}$ formula, differed from the ones obtained by heating up with the exception of $MnSi_{1.80}$ composition. These differences might come from

the presence of side products, which would possibly affect the repeatability of the thermoelectric properties of these materials.

The $MnSi_{1.65}$ composition has shown a small decrease from 1.73248 at 323 K to 1.73201 at 423 K in the γ ratio, which might be attributed to the experimental error. The γ value continuously increased up to its maximum value between 823 K and 923 K, and then gradually decreased above this temperature, approaching the $Mn_{11}Si_{19}$ compound at 1223 K – 1272 K. The transition was, therefore, suggested to be

$$8\ Mn_{15}Si_{26} + MnSi \rightarrow 11\ Mn_{11}Si_{19}$$

at higher than 923 K. An identical transformation has been recognized at 1153 K for the $Mn_{38}Si_{62}$ or $MnSi_{1.63}$ sample, which had very similar starting composition.[98]

The $MnSi_{1.85}$ composition, which was the richest in Si content in this experiment, followed a different pathway while heating up to 1223 K. A small decrease from 1.7343 at room temperature to 1.7335 at 473 K could also be observed, which was followed by an increase to a local maximum of 1.7360 at 673 K, then reduced again above this temperature. The variation in γ continued with a local minimum at 973 K and another maximum at 1073 K, after which the ratio gradually decreased crossing the $Mn_{15}Si_{26}$ line at 1173 K. Under the consideration of the experimental errors, the transition below 673 K could be assigned to

$$9\ Mn_{15}Si_{26} + Si \rightarrow 5\ Mn_{27}Si_{47}$$

and vice versa above this temperature. Surprisingly, Allam *et al*.[98] also revealed an identical transformation at 1133 K in the $Mn_{34}Si_{66}$ sample with a starting Si/Mn atomic ratio of 1.94, from which the initial increase of γ in this work could be attributed to the annealing step.

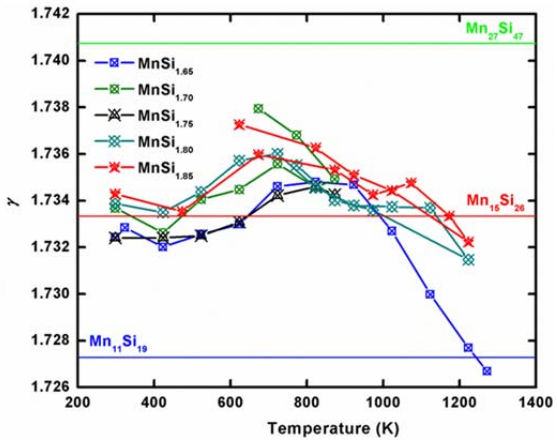

Figure 7.7 Temperature dependence of γ of the $MnSi_x$ (x = 1.65, 1.70, 1.75, 1.80, and 1.85) materials, where the horizontal lines represents different formulas of bulk HMS.

To conclude, the average structural formula at room temperature for the undoped HMS materials prepared under non-equilibrium conditions was $Mn_{15}Si_{26}$, while that for the equilibrium samples was close to $Mn_{27}Si_{47}$. The presence of the side products i.e. MnSi and Si affected the temperature revolution of the γ ratio. The $Mn_{15}Si_{26}$ phase was decomposed to form MnSi and $Mn_{27}Si_{47}$ at high temperature, or it could combine with MnSi or Si side products to transfer into $Mn_{11}Si_{19}$ or $Mn_{27}Si_{47}$, respectively, if theses phases presented in the starting materials with a sufficient content.

7.3.2 Ge substitutions

The HMS-based materials containing 1.1 at.-% and 2.3 at.-% of Ge substituted at the Si sites were also subjected to XRD at high temperature. No additional peaks could be recognized even though the Ge content in the $MnSi_{1.71}Ge_{0.04}$ sample, i.e. 2.3 at.-% at the Si sites (Figure 7.8), has been beyond the reported solubility of Ge in HMS, i.e. 1.6 at.-% at the Si sites.[99] The refined parameters of the Mn and Si subcells increased with increasing the Ge concentration (Table 7.3) due to the larger size of Ge atoms than that of Si atoms, i.e. 1.25 Å and 1.11 Å, respectively. For example, the c_{Si} parameter changed from 2.5216 Å to 2.5290 Å, then to 2.5325 Å in the samples consisting of 0.0 at.-%, 1.1 at.-%, and 2.3 at.-% of Ge at the

Si sites, respectively, implying that the Ge atoms entered into the HMS structure to enlarge the matrix. However, the Si sublattices were expanded more than the Mn sublattices due to the presence of Ge atoms at the Si positions weakening the interactions between Si atoms, which led to decreasing the γ ratio from 1.7324 to 1.7282, then 1.7264 with introducing Ge into the Si sites.

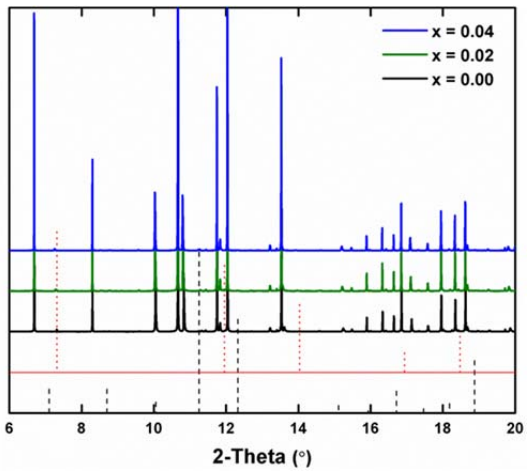

Figure 7.8 XRD patterns of the $MnSi_{1.75-x}Ge_x$ materials at room temperature; the dotted line represents the silicon phase (ICSD-29287), and the dashed line represents the MnSi phase (ICSD-643641).

The diffraction patterns of the Ge-substituted materials heated up from room temperature to 973 K are presented in Figure 7.9. The $MnSi_{1-y}Ge_y$ phase appeared at 923 K in the $MnSi_{1.73}Ge_{0.02}$ material, while it occurred at the lower temperature of 873 K for the $MnSi_{1.71}Ge_{0.04}$ sample. This could be assigned to the transition into another average structural formula in these compositions, where a high content of Ge substitution possibly promoted the transition to happen at a lower temperature.

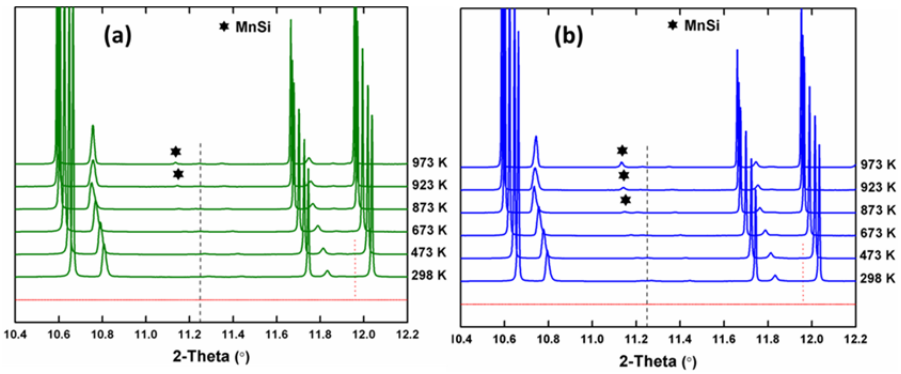

Figure 7.9 Temperature dependence of XRD patterns of the (a) $MnSi_{1.73}Ge_{0.02}$ and (b) $MnSi_{1.71}Ge_{0.04}$ materials; the dotted line represents the silicon phase (ICSD-29287), and the dashed line represents the MnSi phase (ICSD-643641).

All the sublattice parameters in the Ge containing materials also increased linearly with the temperature except for the c_{Si} axis. On the other hand, the c_{Si} parameter exhibited a linear relationship with temperature from room temperature up to around 873 K, beyond which it gradually decreased (Figure 7.10 (a)). This behavior was observed in all the Ge substituted materials at the same temperature regardless of the Ge concentration. Therefore, the formation of the MnSi phase in the $MnSi_{1.73}Ge_{0.02}$ sample possibly occurred at the same temperature with the $MnSi_{1.71}Ge_{0.04}$ one, where the MnSi content was below the detection limit of XRD even though a brilliant synchrotron radiation was used. The linear fitting of the sublattice parameters and volumes was employed to calculate the linear and volume thermal expansion coefficients of the doped HMS materials (

Table 7.4). While the expansion along the a_{Mn}, c_{Mn}, and a_{Si} axes was rather constant with the introduction of Ge, the expansion coefficient along the c_{Si} axis gradually increased with increasing the Ge amount, which again indicated that the interactions between Si atoms was disturbed with the presence of Ge atoms at the same positions. The average structural formulas in the Ge substituted materials could be attributed to the $Mn_{11}Si_{19}$ compound, which was almost stable up to 773 K, where an abrupt increase of the γ ratio towards the $Mn_{15}Si_{26}$ composition was recognized in the sample containing 1.1 at.-% and 2.3 at.-% of Ge. The

sudden variations at this temperature could be assigned to the decomposition to form the $MnSi_{1-y}Ge_y$ phase observed earlier, as expressed in the equation:

$$11\ Mn_{11}(Si_{1-y}Ge_y)_{19} \rightarrow MnSi_{1-z}Ge_z + 8\ Mn_{15}(Si_{1-t}Ge_t)_{26},$$

where y is either 0.011 or 0.023, and 209 y = z + 208 t, assuming that all the Ge only entered the HMS matrix without interfering with the unreacted elemental Si.

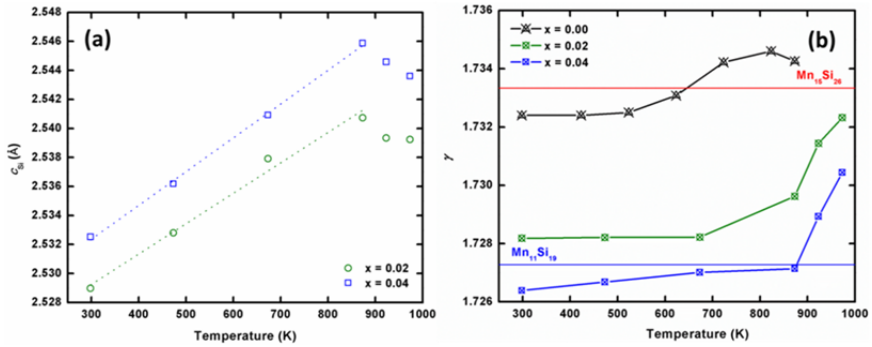

Figure 7.10 Temperature dependence of (a) c_{Si} and (b) γ for the $MnSi_{1.75-x}Ge_x$ materials.

In conclusion, the average structural formula was modified to $Mn_{11}(Si_{1-y}Ge_y)_{19}$ with the introduction of Ge at the Si sites, which was transferred to $Mn_{15}(Si_{1-z}Ge_z)_{26}$ above 773 K, as deduced from the higher thermal expansion along the c_{Si} axis. The phase transformation induced the formation of the $MnSi_{1-y}Ge_y$ phase, which was enhanced with increasing the Ge content.

7.3.3 Al substitutions

The XRD patterns of the Al substituted materials given in Figure 7.11 showed no additional peaks up to 2.3 at.-% of the substituents at the Si sites. Surprisingly, the tiny peak of extra silicon could not be observed in any Al containing samples (Figure 7.11 (b)). Luo *et al.*[129] reported a solubility limit of 0.15 at.-% of Al at the Si sites, and mentioned that no significant impurities could be detected using XRD even in the sample having 0.9 at.-% of Al at the Si sites, which was six times higher than the solubility. Moreover, no impurity phases

could be observed in the powder diagrams of the $Mn(Al_xSi_{1-x})_{1.80}$ sample ($x \leq 0.006$) synthesized by solid state reaction, ball milling, and spark plasma sintering.[150] However, the presence of some Al-rich phases shown in the SEM image of the x = 0.006 material suggested a solubility less than 0.6 at.-% of Al at the Si sites. Here, the Al contents have far exceeded the reported solubility limit, which might somehow affect the morphology of HMS-based materials, explaining the disappearance of the Si peak.

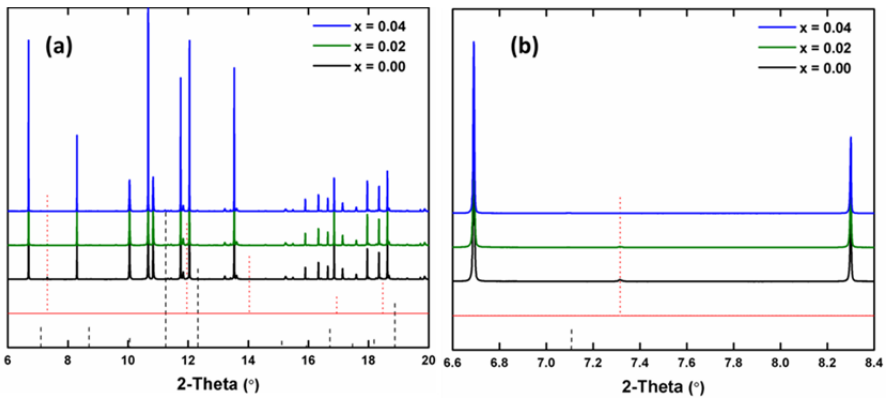

Figure 7.11 XRD patterns of the $MnSi_{1.75-x}Al_x$ materials; the dotted line represents the silicon phase (ICSD-29287), and the dashed line represents the MnSi phase (ICSD-643641).

The refined sublattice parameters of the Al substituted materials were close to those of the non-doped $MnSi_{1.75}$ sample due to very similar sizes of Al and Si atoms (Table 7.3), i.e. 1.18 Å and 1.11 Å, respectively, which was in agreement with the other reports.[150,222]

The peaks of the side products appeared in the XRD patterns of the HMS-based materials containing 1.1 at.-% of Al at the Si sites (Figure 7.12) at high temperature. The Si peak became detectable at 923 K (Figure 7.12 (a)), while that of the MnSi phase could be recognized as low as 873 K (Figure 7.12 (b)). This might either indicate two phase transitions at 873 K and 923 K releasing MnSi and Si, respectively, or imply that the presence of Si peak was actually overlooked at less than 923 K due to its low intensity.

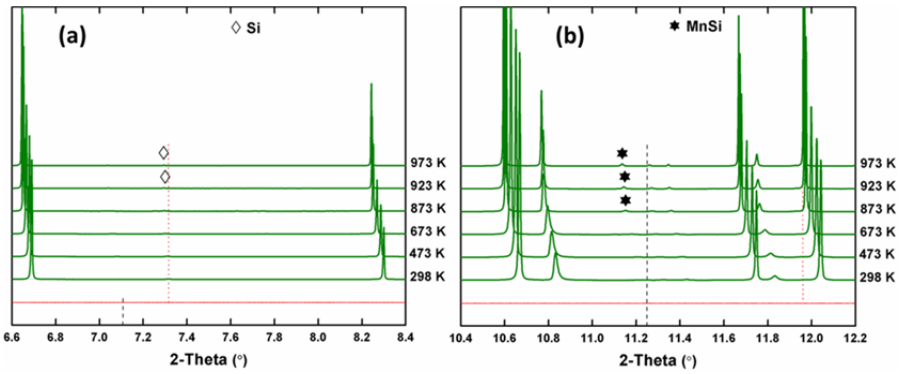

Figure 7.12 The formation of (a) Si and (b) MnSi for the $MnSi_{1.73}Al_{0.02}$ material upon heating; the dotted line represents the silicon phase (ICSD-29287), and the dashed line represents the MnSi phase (ICSD-643641).

However, the MnSi peak appeared in the powder diagram of the $MnSi_{1.71}Al_{0.04}$ sample with 2.3 at.-% of Al at the Si sites since 673 K, which slightly increased in intensity above this temperature, without any clear evidence of the Si peak (Figure 7.13). Obviously, the high content of Al accelerated the decomposition of HMS material forming the MnSi phase to transfer to another structural formula as with the Ge substitution. Elemental Si, therefore, might have been present at lower temperatures, but was unrecognizable due to its low content.

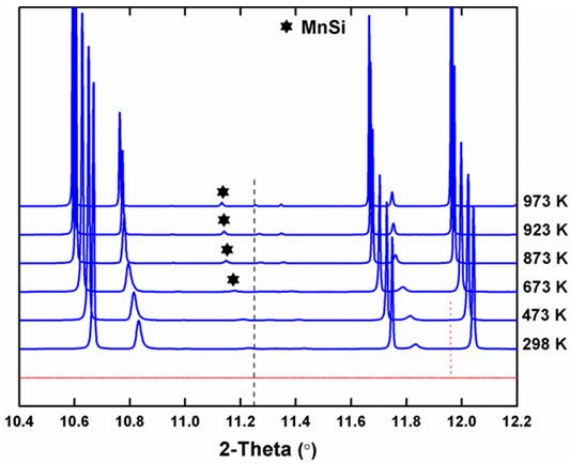

Figure 7.13 The formation of the MnSi phase for the $MnSi_{1.71}Al_{0.04}$ material upon heating; the dotted line represents the silicon phase (ICSD-29287), and the dashed line represents the MnSi phase (ICSD-643641).

Interestingly, the refined a_{Si} parameter of the Al-doped HMS materials showed an abrupt change above 473 K, where the length was suddenly reduced from around 3.915 Å at 473 K to approximately 3.896 Å at 673 K regardless of the Al content (Figure 7.14 (a)), while the a_{Si} size still exhibited a steady increase with increasing temperature up to 473 K as well as above 673 K. Surprisingly, the c_{Si} parameter still gradually increased at elevating temperature for the whole temperature range, even though the interactions between Si atoms along this direction was always considered to be loose, usually resulting in larger modifications for the c_{Si} axis with chemical substitutions or thermal treatments than for the other axes. Consequently, the Al substitutions seemed to create more variations along the a_{Si} axis than along the c_{Si} one, possibly related to the similar sizes between Al and Si atoms.

The linear fitting below 473 K for the a_{Si} and V_{Si} parameter was applied to calculate the linear and volume thermal expansion coefficient at room temperature of the Al substituted materials (

Table 7.4). The introduction of Al at the Si sites insignificantly affected the expansion of the Mn sublattices, which was similar to the Ge substituted compounds. On the other hand,

the linear thermal expansion coefficient along the c_{Si} axis was nearly doubled from 7.3×10^{-6} K^{-1} for the Al free sample to 13.5×10^{-6} K^{-1} and 14×10^{-6} K^{-1} for the materials with 1.1 at.-% and 2.3 at.-% of Al at the Si sites, respectively. However, the expansion coefficient of the a_{Si} axis was very close to that of the $MnSi_{1.75}$ composition, probably due to the linearity from room temperature to 473 K based on only two temperatures, leading to significant errors for the analysis.

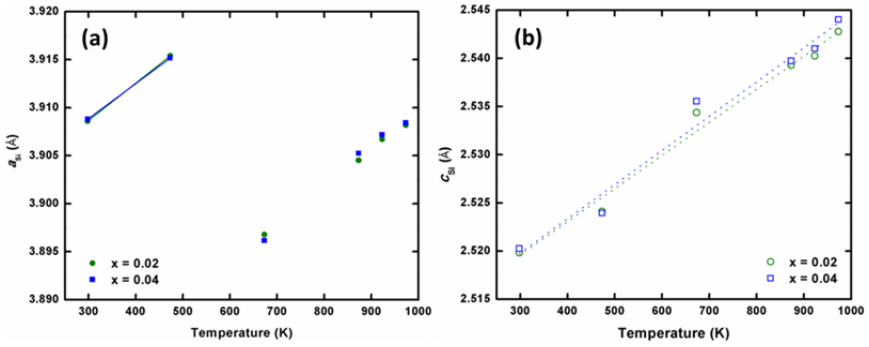

Figure 7.14 Temperature dependence of the (a) a_{Si} and (b) c_{Si} parameters for the $MnSi_{1.75-x}Al_x$ materials.

The γ values of the materials containing 1.1 at.-% and 2.3 at.-% of Al at the Si sites were nearly identical to those of $Mn_{15}Si_{26}$ from room temperature to 473 K (Figure 7.15). A sudden decrease to near 1.730 was observed at 673 K, corresponding to the abrupt change in the a_{Si} axis, the huge increase in the linear thermal expansion coefficient along the c_{Si} direction, and the appearance of the MnSi and Si phases in the powder diagram. Above 673 K, the average structural formulas of Al containing samples slightly varied around the $Mn_{11}Si_{19}$ composition. Due to the decomposition into the $Mn_{11}Si_{19}$ and MnSi phases reducing the total Si content present in the silcides, the formation of Si phase was required to balance the equation of disproportionation:

$$Mn_{15}(Si_{1-y}Al_y)_{26} \rightarrow Mn_{11}(Si_{1-z}Al_z)_{19} + 4\ Mn(Si_{1-t}Al_t) + 3\ Si,$$

where y is either 0.011 or 0.023, and 26 y = 19 z + 4 t, assuming that all the Al only entered the HMS matrix without interfering with the unreacted elemental Si. The samples with 1.1 at.-% and 2.3 at.-% of Al at the Si sites showed the decompositions at the same temperature from 473 K to 673 K, even though the Si content was insufficient to be detected in this temperature range for the material containing the low Al concentration.

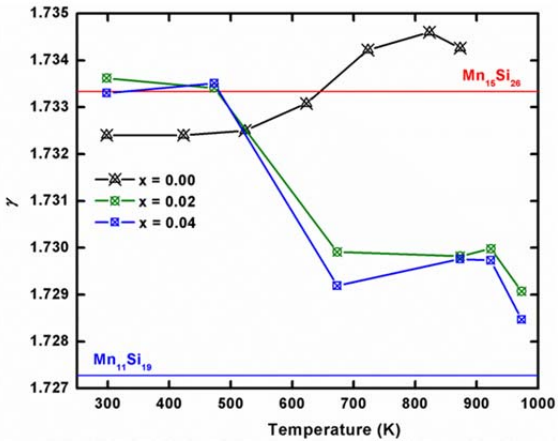

Figure 7.15 Temperature dependence of γ for the $MnSi_{1.75-x}Al_x$ materials.

Generally, the average structural formulas of the Al containing materials intercepted with the $Mn_{15}Si_{26}$ composition at room temperature, decomposing into the $Mn_{11}Si_{19}$, MnSi, and Si phases between 473 K and 673 K. An abrupt change could be identified for the a_{Si} axis in the same temperature range, while no particular modifications along the c_{Si} axis was observed, which possibly originated from the similar sizes of the Al and Si atoms. Furthermore, the presence of the MnSi and Si phases might be hindered at low temperature for the sample with 1.1 at.-% of Al at the Si sites due to their low contents.

7.3.4 Cr substitutions

Again, no peaks of the side products could be identified for the diffraction patterns of the $Mn_{1-x}Cr_xSi_{1.75}$ materials due to the low concentration of the substituent with only 2 at.-% and 4 at.-% of Cr at the Mn sites (Figure 7.16). Kikuchi *et al.*[138] have reported a solubility

limit up to 20 at.-% of Cr at the Mn sites according to Vegard's rule, which was more than five times of the Cr contents chosen in this study. The atomic radius of chromium is slightly larger than that of manganese, 1.66 Å and 1.61 Å, respectively, resulting in a small enlargement of the Mn sublattice with the substitution of Cr at the Mn sites (Table 7.3). However, the c_{Si} axis length gradually decreased from 2.5216 Å to 2.5202 Å, then 2.5194 Å for the samples with 0 at.-%, 2 at.-%, and 4 at.-% of Cr at the Mn sites, respectively, leading to a steady increase of γ from 1.7324 to 1.7340 and 1.7351, correspondingly. These observations were in complete agreement with the other report.[138] Moreover, the substitution using a smaller element than manganese, i.e. iron with an atomic radius of 1.56 Å, actually led to an opposite trend, i.e. reducing the sizes of the Mn sublattice, while slightly increasing the c_{Si} parameter.[124]

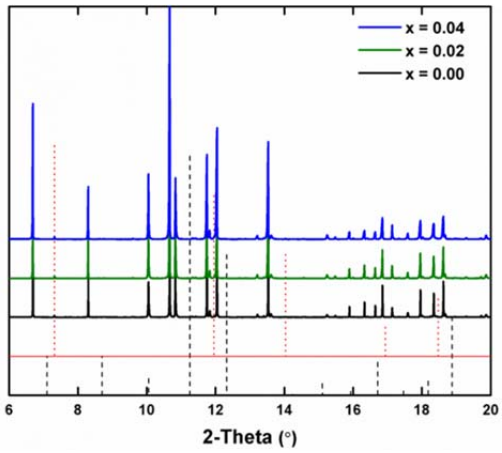

Figure 7.16 XRD patterns at room temperature for the $Mn_{1-x}Cr_xSi_{1.75}$ materials; the dotted line represents the silicon phase (ICSD-29287), and the dashed line represents the MnSi phase (ICSD-643641).

The phase transition in the Cr-doped materials could be identified above 873 K where the MnSi peak appeared at around 923 K in the samples containing 2 at.-% and 4 at.-% of Cr at the Mn sites (Figure 7.17).

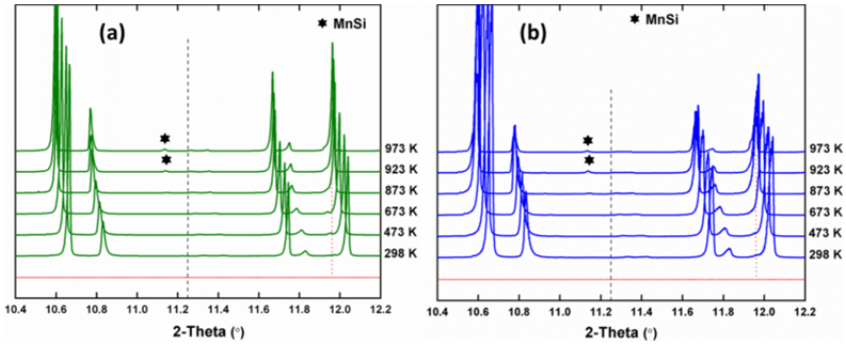

Figure 7.17 The formation of the MnSi phase for the (a) $Mn_{0.98}Cr_{0.02}Si_{1.75}$ and (b) $Mn_{0.96}Cr_{0.04}Si_{1.75}$ materials upon heating; the dotted line represents the silicon phase (ICSD-29287), and the dashed line represents the MnSi phase (ICSD-643641).

The temperature revolution of the c_{Si} parameter followed a linear relationship up to 873 K, above which the phase transition was anticipated to occur regardless of the Cr concentration (Figure 7.18 (a)). The γ ratios of the Cr-doped materials were in the proximity of the $Mn_{15}Si_{26}$ compound, which increased towards the $Mn_{27}Si_{47}$ formula with increasing the temperature (Figure 7.18 (b)). However, the transition above 873 K was unapparent as in the compounds substituted at the Si sites, where the transition equation could be written as

$$20\ (Mn_{1-y}Cr_y)_{15}Si_{26} \rightarrow 11\ (Mn_{1-z}Cr_z)_{27}Si_{47} + 3\ (Mn_{1-t}Cr_t)Si$$

with y is either 0.02 or 0.04, 100 y = 99 z + t, assuming that all the Cr only entered the HMS matrix without interfering with the unreacted elemental Si.

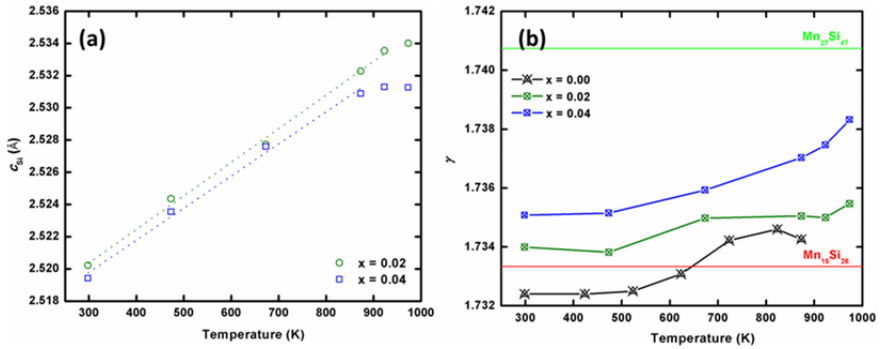

Figure 7.18 Temperature dependence of the (a) c_{Si} and (b) γ parameters for the $Mn_{1-x}Cr_xSi_{1.75}$ materials.

To summarize, the average structural formulas of the Cr-doped HMS materials were close to the $Mn_{15}Si_{26}$ compound at room temperature, which transferred gradually towards the $Mn_{27}Si_{47}$ formula upon heating. The phase transition occurring above 873 K was revealed from the appearance of the MnSi phase as well as the deviation of the c_{Si} length from a linear behavior, which was not very obvious in the variations of the γ ratios. The Cr substitution enlarged the Mn sublattice due to the larger size of the Cr atom compared to the Mn atom, but steadily reduced the c_{Si} parameter within the studied compositional range.

7.3.5 Mo substitutions

The extra peaks assigned to the disilicide phase $MoSi_2$ was observed in the powder diagrams with the substitution of Mo at the Mn sites where the intensities were increased with increasing the Mo content owning to the low solubility of Mo in the HMS matrix (Figure 7.19). Even though the atomic radius of Mo, i.e. 1.90 Å, is much bigger than that of Mn, i.e. 1.61 Å, the introduction of Mo into the HMS material showed insignificant effects on the a_{Mn}, c_{Mn}, and a_{Si} parameters at its concentration of 2 at.-% at the Mn sites, while an amount of 4 at.-% of Mo at the Mn sites enlarged the Mn and Si sublattices in all directions (Table 7.3). This might stem from the low solubility of Mo in the HMS matrix due to the size differences, which was enhanced with increasing the Mo amount. The appearance of the $MoSi_2$ phase have been previously recognized for the HMS-based materials prepared by ball

milling without adding *n*-hexane and spark plasma sintering, but a slight increase of all the refined parameters was observed, which possibly related to the presence of side products as well as the high background of the diffraction patterns, inducing additional errors to the analysis.[222] On the other hand, the c_{Si} axis was gradually expanded with increasing the amount of Mo substitution from 2.5216 Å to 2.5228 Å, then 2.5233 Å for the materials without Mo and with 2 at.-% and 4 at.-% of Mo at the Mn sites, respectively (Table 7.3). As a result, the γ ratio showed a small reduction from 1.7324 in the $MnSi_{1.75}$ compound to around 1.7316 in the Mo-substituted materials, which was between the $Mn_{15}Si_{26}$ and $Mn_{11}Si_{19}$ formula, closer to the one with higher Si/Mn atomic ratios. Similar refinements performed on the HMS-based materials containing the side products of MnSi and Si led to a slightly lower γ value of 1.7284 with 2 at.-% of Mo at the Mn sites explained by different experimental and analysis conditions.[222]

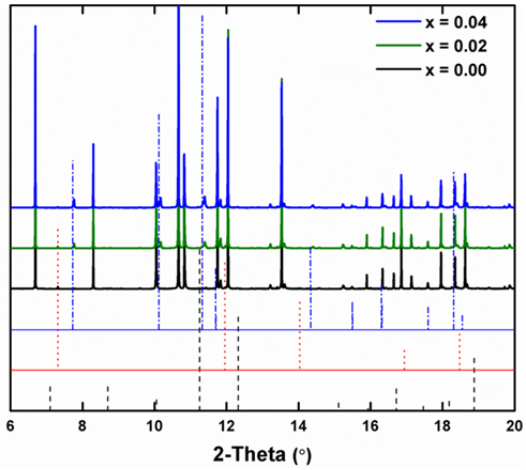

Figure 7.19 XRD patterns at room temperature for the $Mn_{1-x}Mo_xSi_{1.75}$ materials; the dotted line represents the silicon phase (ICSD-29287), the dashed line represents the MnSi phase (ICSD-643641), and the dashed dotted line represents the $MoSi_2$ phase (ICSD-96023).

Table 7.3 Le Bail refined subcell parameters from XRD patterns at room temperature of HMS-based materials doped with Ge, Si, Cr, and Mo using synchrotron radiation.

Nominal compositions	a_{Mn} (Å)	c_{Mn} (Å)	a_{Si} (Å)	c_{Si} (Å)	$\gamma = c_{Mn}/c_{Si}$
$MnSi_{1.75}$	5.52730(1)	4.36843(1)	3.90853(1)	2.52161(1)	1.73240(1)
$MnSi_{1.73}Ge_{0.02}$	5.52868(1)	4.37054(1)	3.90961(5)	2.52898(4)	1.72818(3)
$MnSi_{1.71}Ge_{0.04}$	5.52955(1)	4.37211(1)	3.91020(2)	2.53252(3)	1.72639(2)
$MnSi_{1.73}Al_{0.02}$	5.52743(1)	4.36842(1)	3.90858(4)	2.51982(3)	1.73362(2)
$MnSi_{1.71}Al_{0.04}$	5.52731(1)	4.36833(1)	3.90879(3)	2.52024(3)	1.73330(2)
$Mn_{0.98}Cr_{0.02}Si_{1.75}$	5.52914(1)	4.37007(1)	3.91076(2)	2.52022(2)	1.73400(1)
$Mn_{0.96}Cr_{0.04}Si_{1.75}$	5.53024(2)	4.37137(3)	3.91064(2)	2.51941(2)	1.73508(2)
$Mn_{0.98}Mo_{0.02}Si_{1.75}$	5.52700(1)	4.36836(1)	3.90837(1)	2.52277(2)	1.73157(1)
$Mn_{0.96}Mo_{0.04}Si_{1.75}$	5.52826(2)	4.36938(2)	3.90928(2)	2.52330(2)	1.73161(2)

Table 7.4 Linear and volume thermal expansion coefficient for the HMS-based materials doped with Ge, Si, Cr, and Mo at room temperature; all the temperatures mentioned in the parentheses are in Kelvin.

α, β ($\times 10^{-6}$ K^{-1})	α (a_{Mn})	α (a_{Si})	α (c_{Mn})	α (c_{Si})	β (V_{Mn})	β (V_{Si})
$MnSi_{1.75}$	10.5(1)	10.5(1)	9.8(1)	7.3(4)	31.0(4)	28.30(3)
$MnSi_{1.73}Ge_{0.02}$	10.2(1)	10.2(2)	9.66(9)	8.3(8) (<873.15)	30.316(5)	28.5(8) (<873.15)
$MnSi_{1.71}Ge_{0.04}$	10.6(2)	10.5(2)	10.06(9)	9.2(2) (<873.15)	31.4(4)	30.0(5) (<873.15)
$MnSi_{1.73}Al_{0.02}$	10.31(9)	9.9525(1) (<473.15)	9.64(7)	13.5(8)	30.5(3)	34.0346(7) (<473.15 K)
$MnSi_{1.71}Al_{0.04}$	10.6(1)	9.31234(7) (<473.15)	9.91(9)	14(1)	31.3(4)	27.0089(4) (<473.15)
$Mn_{0.98}Cr_{0.02}Si_{1.75}$	10.09(9)	9.8(2)	9.43(7)	8.3(3) (<923.15)	29.8(2)	28.0(5) (<923.15)
$Mn_{0.96}Cr_{0.04}Si_{1.75}$	10.5(1)	10.2(1)	9.79(9)	7.9(4) (<923.15)	31.0(3)	28.8(5) (<923.15)

7.4 Conclusions

In this report, HMS-based materials with different Si/Mn atomic ratios and various dopants e.g. Ge, Al, Cr, or Mo have been synthesized by a simple and effective method utilizing wet ball milling in *n*-hexane and subsequent spark plasma sintering. The obtained powders were subjected to XRD upon heating up from room temperature to high temperature using synchrotron radiation. Moreover, Le Bail refinement was employed to fit the peaks in the powder diagram of the HMS superstructure to the corresponding ones for the Mn and Si sublattices, resulting in the lattice parameters and the Si/Mn atomic ratios, from which the average structural formulas could be predicted.

For the undoped HMS-based materials at room temperature prepared under non-equilibrium conditions, the average structural formula of the powder could be identified as (mostly) $Mn_{15}Si_{26}$, where the presence of the side products i.e. MnSi and Si was found to affect the temperature dependence of the γ ratio. Upon heating up to high temperature, the $Mn_{15}Si_{26}$ phase either decomposed into MnSi and $Mn_{27}Si_{47}$ or reacted with MnSi or Si to yield $Mn_{11}Si_{19}$ or $Mn_{27}Si_{47}$, respectively, if theses phases were present in the starting materials with a sufficient amount.

The nature of dopants was found to significantly influence the average structural formula as well as the temperature revolution of the Si/Mn atomic ratio. With Ge substitutions at the Si sites, the structural formula at room temperature was modified to $Mn_{11}Si_{19}$, transformed into $Mn_{15}Si_{26}$ and MnSi above 773 K. The thermal expansion along the c_{Si} axis was enhanced due to the presence of Ge at the Si sites weakening the interactions between the Si atoms.

On the other hand, the Al substitutions at the Si sites retained the average structural formula of HMS-based materials at room temperature to be $Mn_{15}Si_{26}$, which decomposed into $Mn_{11}Si_{19}$, MnSi, and Si in the temperature range of 473 K – 673 K. Interestingly, an abrupt change could be identified for the a_{Si} axis in the same temperature range, but no special changes could be observed for the c_{Si} axis, which possibly stemmed from the similar sizes between Al and Si atoms.

Similarly, the $Mn_{15}Si_{26}$ formula could be assigned for the Cr-doped HMS materials at room temperature, which gradually transferred towards the $Mn_{27}Si_{47}$ and MnSi phases at temperatures above 873 K. Apparently, the c_{Si} length deviated from a linear behavior above the transition temperature. The Cr substitution enlarged the Mn sublattice due to the large atomic radius of Cr atom in comparison with that of Mn atom, but the c_{Si} parameter steadily decreased within the experimentally compositional range.

For the Mo substitutions at the Mn sites, the $MoSi_2$ phase was observed in the powder diagrams due to the low solubility of Mo in the HMS matrix. The big Mo atoms expanded

the Mn and Si sublattices, where the large increase of the c_{Si} parameter led to slightly decreasing the γ ratio falling in between the $Mn_{11}Si_{19}$ and $Mn_{15}Si_{26}$ compositions.

Physical property measurements on the $MnSi_{1.75}$ compound revealed that the observed significant change in the γ ratio corresponded to the initiation of the bipolar diffusion due to the excitation of electrons into the Si-Si antibonding orbitals.[102] Therefore, it could be anticipated that the temperature evolution of the γ values for the HMS-based materials with different Si/Mn atomic ratios and various dopants should relate to the temperature dependence of their thermoelectric properties.

Chapter 8

Conclusions

The HMS compounds consisting of different structural formulas are the only binary phases among the manganese silicides that are promising for thermoelectric materials. All the HMS phases crystallize in the tetragonal Nowotny chimney ladder structure consisting of the Mn atoms arranged as chimneys in which the Si atoms are spiraling as ladders. These compounds follow the 14 valence electron rule, i.e. the material Mn_4Si_7 behaves as intrinsic semiconductors and the others are heavily doped *p*-type semiconductors. Several challenges still remain for the HMS system, including improving the thermoelectric performance of polycrystalline samples, completely eliminating the MnSi side product during synthesis, and establishing the stability range of various HMS phases in different temperature and compositional ranges.

In order to enhance the thermoelectric figure of merit through reducing the lattice thermal conductivity, the composites with the nano-inclusions, i.e. C_{60} and MWCNTs and the substitutions with Mo, W, or Ag at the Mn sites, and Ge or Al at the Si sites have been investigated. It was found out that an even distribution of MWCNTs within the HMS-based matrix helped to considerably decrease the thermal diffusivity of the composites, but insignificantly affected the electrical properties. Consequently, a promising improvement up to 20% with 1.0 wt-% MWCNTs for the figure of merit, which reached 0.4 at 850 K, has been achieved. Moreover, a similar *ZT* value has been obtained at 815 K for the HMS-based material containing 2 at.-% Mo at the Mn sites. The Mo, W, and Al substitutions reduced the electrical resistivity and the lattice thermal conductivity of the base material for both single and double-substituted materials. Furthermore, the material with 1 at.-% Ag at the Mn sites also showed a reduced thermal conductivity and enhanced *ZT* value, achieving 0.37 at 850 K.

Various methods for preparing HMS-based materials containing no side products have been thoroughly investigated, including mechanical alloying, mechanical milling and furnace heating, ball milling and reactive spark plasma sintering; solid state reaction, and

chemical vapor transport. Several materials with the maximum figure of merit ranging from 0.31 to 0.43 have been synthesized, but the MnSi side products and unreacted Si could not be excluded in all the cases. Additionally, chemical vapor transport for growing single crystals of the HMS phases resulted in low yield and bad crystal qualities, where all the crystals were identified as having the simple formulae Mn_4Si_7. On the other hand, pure HMS without any side products has been synthesized by ball milling in *n*-hexane and reactive spark plasma sintering for a direct solid state reaction and densification. The obtained fine particle sizes from the ball milling step promoted the subsequent reaction to totally occur, leading to a single phase material within the detection limit of our characterization methods. As a consequence, a better thermoelectric performance, with 20% higher Seebeck coefficient values, 23% lower electrical resistivity, and 30% lower thermal conductivity than the one synthesized by ball milling without *n*-hexane for the whole temperature range, attaining a maximum *ZT* of 0.55 at 850 K, which is amongst the highest for undoped HMS-based materials. Based on these preliminary results, this method has very high potential for applications in industry due to its simplicity and effectiveness.

Subsequently, HMS-based materials with different Si/Mn atomic ratios and various dopants e.g. Ge, Al, Cr, or Mo have been synthesized for the studies of structural evolutions upon heating up from room temperature to high temperature using XRD at the synchrotron. The refined lattice parameters of the Mn and Si sublattices were used to calculate the Si/Mn atomic ratios and predict the formulas. The formulae at room temperature and its temperature dependence were found to be significantly affected by the compositions of the starting materials as well as the nature of dopants. Physical property measurements on the $MnSi_{1.75}$ compound revealed that the temperature evolution of the γ values, where γ is the Si/Mn atomic ratio in the HMS phase, for the HMS-based materials should somehow relate to the temperature dependence of their thermoelectric properties due to the modifications of the electronic structure in these materials. Efforts are on the ways to reveal these possible correlations.

For future research, we suggest to study different nano-inclusions, such as HMS-based nanostructures or Ag nanoparticles, for the materials prepared by ball milling in *n*-

hexane and reactive spark plasma sintering, aiming to reduce the lattice thermal conductivity, which is the main contribution to the thermal conduction in the HMS system, and enhance the power factor. The substitutions at the Mn sites have been widely investigated with a variety of substituents, which mainly came from the transition metals, while those at the Si sites have been confined to mostly Al and Ge. The attempts using different main group elements, e.g. Mg, might be worth to try for the Mn sites, and the substitutions at the Si sites could be experimentally extended to include other elements, such as Bi, Sb, Te. Moreover, the temperature evolutions of various HMS-based materials need to be confirmed via the sophistical characterization methods, e.g. TEM for the establishments of the stability ranges, leading to set up specific controllable conditions to separately synthesize different HMS phases. Finally, single crystal growth, using chemical vapor transport or flux method to achieve high quality single crystals, as well as the optimization of synthesis techniques from the melt to completely eliminate the side products are also exciting opportunities for future research.

Bibliography

(1) Velmre, E. *Proc. Est. Acad. Sci.* **2007**, *13*, 276–282.

(2) Kauffman, G. *Chem. Educ.* **1999**, *4*, 36–37.

(3) Tritt, T. M.; Subramanian, M. A. *MRS Bull.* **2006**, *31*, 188–198.

(4) Pollock, D. D. In *CRC Handbook of Thermoelectrics*; Rowe, D. M., Ed.; CRC Press, New York, **1995**,7–17.

(5) Goldsmid, H. J. In *CRC Handbook of Thermoelectrics*; Rowe, D. M., Ed.; CRC Press, New York, **1995,** 19–25.

(6) Snyder, G. J.; Toberer, E. S. *Nat. Mater.* **2008**, *7*, 105–114.

(7) Cutler, M.; Leavy, J. F.; Fitzpatrick, R. L. *Phys. Rev.* **1964**, *133*, A1143.

(8) Mott, N. F.; Jones, H. *The theory of the properties of metals and alloys*; Courier Corporation, **1958**.

(9) Mahan, G. D.; Sofo, J. O. *Proc. Natl. Acad. Sci.* **1996**, *93*, 7436–7439.

(10) Heremans, J. P.; Wiendlocha, B.; Chamoire, A. M. *Energy Environ. Sci.* **2012**, *5*, 5510–5530.

(11) Kumar, G. S.; Prasad, G.; Pohl, R. O. *J. Mater. Sci.* **1993**, *28*, 4261–4272.

(12) Slack, G. In *CRC Handbook of Thermoelectrics*; Rowe, D. M., Ed.; CRC Press, New York, **1995**, 407–440.

(13) Liu, H.; Shi, X.; Xu, F.; Zhang, L.; Zhang, W.; Chen, L.; Li, Q.; Uher, C.; Day, T.; Snyder, G. J. *Nat. Mater.* **2012**, *11*, 422–425.

(14) Oudah, M.; Kleinke, K. M.; Kleinke, H. *Inorg. Chem.* **2014**, *54*, 845–849.

(15) Goldsmid, H. J.; Douglas, R. W. *Br. J. Appl. Phys.* **1954**, *5*, 386.

(16) Scherrer, S.; Scherrer, H. In *CRC Handbook of Thermoelectrics*; Rowe, D. M., Ed.; CRC Press, New York, **1995**, 211–237.

(17) Stordeur, M. In *CRC Handbook of Thermoelectrics*; Rowe, D. M., Ed.; CRC Press, New York, **1995**, 239–255.

(18) Xie, W.; Wang, S.; Zhu, S.; He, J.; Tang, X.; Zhang, Q.; Tritt, T. M. *J. Mater. Sci.* **2013**, *48*, 2745–2760.

(19) Wu, F.; Song, H.; Gao, F.; Shi, W.; Jia, J.; Hu, X. *J. Electron. Mater.* **2013**, *42*, 1140–1145.

(20) Du, B.; Li, H.; Xu, J.; Tang, X.; Uher, C. *Chem. Mater.* **2010**, *22*, 5521–5527.

(21) Hsu, K. F.; Loo, S.; Guo, F.; Chen, W.; Dyck, J. S.; Uher, C.; Hogan, T.; Polychroniadis, E. K.; Kanatzidis, M. G. *Science* **2004**, *303*, 818–821.

(22) Androulakis, J.; Hsu, K. F.; Pcionek, R.; Kong, H.; Uher, C.; D'Angelo, J. J.; Downey, A.; Hogan, T.; Kanatzidis, M. G. *Adv. Mater.* **2006**, *18*, 1170–1173.

(23) Poudeu, P. F. P.; D'Angelo, J.; Downey, A. D.; Short, J. L.; Hogan, T. P.; Kanatzidis, M. G. *Angew. Chemie* **2006**, *118*, 3919–3923.

(24) Fleurial, J. P.; Caillat, T.; Borshchevsky, A. In *Thermoelectrics, 1997. Proceedings ICT'97. XVI International Conference on*; IEEE, **1997**, 1–11.

(25) Shi, X.; Yang, J.; Salvador, J. R.; Chi, M.; Cho, J. Y.; Wang, H.; Bai, S.; Yang, J.; Zhang, W.; Chen, L. *J. Am. Chem. Soc.* **2011**, *133*, 7837–7846.

(26) Caillat, T.; Fleurial, J.-P.; Borshchevsky, A. *J. Phys. Chem. Solids* **1997**, *58*, 1119–1125.

(27) Guo, Q.; Chan, M.; Kuropatwa, B. A.; Kleinke, H. *Chem. Mater.* **2013**, *25*, 4097–4104.

(28) Guo, Q.; Assoud, A.; Kleinke, H. *Adv. Energy Mater.* **2014**, *4*, 1400348.

(29) Vining, C. B.; Fleurial, J.-P. In *Proc. X International Conf. on Thermoelectrics.–Arlington, USA*; **1991**, 1–14.

(30) LaLonde, A. D.; Pei, Y.; Snyder, G. J. *Energy Environ. Sci.* **2011**, *4*, 2090–2096.

(31) Pei, Y.; LaLonde, A. D.; Iwanaga, S.; Snyder, G. J. *Energy Environ. Sci.* **2011**, *4*, 2085–2089.

(32) Davidow, J.; Gelbstein, Y. *J. Electron. Mater.* **2013**, *42*, 1542–1549.

(33) Levin, E. M.; Bud'ko, S. L.; Schmidt-Rohr, K. *Adv. Funct. Mater.* **2012**, *22*, 2766–2774.

(34) Brown, S. R.; Kauzlarich, S. M.; Gascoin, F.; Snyder, G. J. *Chem. Mater.* **2006**, *18*, 1873–1877.

(35) Liu, H.; Yuan, X.; Lu, P.; Shi, X.; Xu, F.; He, Y.; Tang, Y.; Bai, S.; Zhang, W.; Chen, L. *Adv. Mater.* **2013**, *25*, 6607–6612.

(36) Xu, H.; Kleinke, K. M.; Holgate, T.; Zhang, H.; Su, Z.; Tritt, T. M.; Kleinke, H. *J. Appl. Phys.* **2009**, *105*, 53703.

(37) May, A. F.; Flage-Larsen, E.; Snyder, G. J. *Phys. Rev. B* **2010**, *81*, 125205.

(38) Rhyee, J.-S.; Lee, K. H.; Lee, S. M.; Cho, E.; Kim, S. Il; Lee, E.; Kwon, Y. S.; Shim, J. H.; Kotliar, G. *Nature* **2009**, *459*, 965–968.

(39) Saramat, A.; Svensson, G.; Palmqvist, A. E. C.; Stiewe, C.; Mueller, E.; Platzek, D.; Williams, S. G. K.; Rowe, D. M.; Bryan, J. D.; Stucky, G. D. *J. Appl. Phys.* **2006**, *99*, 23708.

(40) Sakurada, S.; Shutoh, N. *Appl. Phys. Lett.* **2005**, *86*, 82105.

(41) Sui, J.; Li, J.; He, J.; Pei, Y.-L.; Berardan, D.; Wu, H.; Dragoe, N.; Cai, W.; Zhao, L.-D. *Energy Environ. Sci.* **2013**, *6*, 2916–2920.

(42) Lu, X.; Morelli, D. T. *Phys. Chem. Chem. Phys.* **2013**, *15*, 5762–5766.

(43) Khan, A. U.; Vlachos, N.; Kyratsi, T. *Scr. Mater.* **2013**, *69*, 606–609.

(44) Yoshikura, M.; Itoh, T. *J. Japan Soc. Powder Powder Metall.* **2010**, *57*, 242–246.

(45) Sakamaki, Y.; Kuwabara, K.; Jiajun, G.; Inui, H.; Yamaguchi, M.; Yamamoto, A.; Obara, H. In *Materials Science Forum*; Trans Tech Publ, **2003**, *426*, 1777–1782.

(46) Arita, Y.; Mitsuda, S.; Nishi, Y.; Matsui, T.; Nagasaki, T. *J. Nucl. Mater.* **2001**, *294*, 202–205.

(47) Zevalkink, A.; Toberer, E. S.; Zeier, W. G.; Flage-Larsen, E.; Snyder, G. J. *Energy Environ. Sci.* **2011**, *4*, 510–518.

(48) Zhao, L.-D.; He, J.; Wu, C.-I.; Hogan, T. P.; Zhou, X.; Uher, C.; Dravid, V. P.; Kanatzidis, M. G. *J. Am. Chem. Soc* **2012**, *134*, 7902–7912.

(49) Zhao, L.-D.; Lo, S.-H.; Zhang, Y.; Sun, H.; Tan, G.; Uher, C.; Wolverton, C.; Dravid, V. P.; Kanatzidis, M. G. *Nature* **2014**, *508*, 373–377.

(50) Li, D.; Qin, X. Y.; Zou, T. H.; Zhang, J.; Ren, B. J.; Song, C. J.; Liu, Y. F.; Wang, L.; Xin, H. X.; Li, J. C. *J. Alloys Compd.* **2014**, *635*, 87-91.

(51) Biswas, K.; He, J.; Blum, I. D.; Wu, C.-I.; Hogan, T. P.; Seidman, D. N.; Dravid, V. P.; Kanatzidis, M. G. *Nature* **2012**, *489*, 414–418.

(52) Gokhale, A. B.; Abbaschian, R. *Bull. Alloy Phase Diagrams* **1990**, *11*, 468–480.

(53) Massalski, T. B.; Okamoto, H.; Subramanian, P. R.; Kacprzak, L.; Scott, W. W. *Binary alloy phase diagrams*; American Society for Metals Metals Park, OH, **1986**, *1*.

(54) Jørgensen, J.-E.; Rasmussen, S. E. *Powder Diffr.* **1991**, *6*, 194–195.

(55) Al-Sharif, A. I.; Abu-Jafar, M.; Qteish, A. *J. Phys. Condens. Matter* **2001**, *13*, 2807.

(56) Pfleiderer, C.; Reznik, D.; Pintschovius, L.; Löhneysen, H. v; Garst, M.; Rosch, A. *Nature* **2004**, *427*, 227–231.

(57) Jonietz, F.; Mühlbauer, S.; Pfleiderer, C.; Neubauer, A.; Münzer, W.; Bauer, A.; Adams, T.; Georgii, R.; Böni, P.; Duine, R. A. *Science* **2010**, *330*, 1648–1651.

(58) Bloch, D.; Voiron, J.; Jaccarino, V.; Wernick, J. H. *Phys. Lett. A* **1975**, *51*, 259–261.

(59) Hortamani, M. Theory of adsorption, diffusion and spinpolarization of Mn on Si (001) and Si (111) substrates, Freie Universitat Berlin, **2006**.

(60) Hortamani, M.; Kratzer, P.; Scheffler, M. *Phys. Rev. B* **2007**, *76*, 235426.

(61) Geisler, B.; Kratzer, P.; Suzuki, T.; Lutz, T.; Costantini, G.; Kern, K. *Phys. Rev. B* **2012**, *86*, 115428.

(62) Shinoda, D. *Phys. status solidi* **1972**, *11*, 129–135.

(63) Sakurai, J.; Yamamoto, Y.; Komura, Y. *J. Phys. Soc. Japan* **1988**, *57*, 24.

(64) Bienert, W. B.; Gillen, F. M. Process of making mnsi thermoelectric element and product of said process. U. S. Patent No. 3407037, **1968**.

(65) Kanibolotskii, D. S.; Lesnyak, V. V. *Russ. Metall.* **2006**, *2006*, 199–205.

(66) Eremenko, V. N.; Lukashenko, G. M.; Sidorko, V. R. *Sov. Powder Metall. Met. Ceram.* **1965**, *3*, 393–395.

(67) Higgins, J. M.; Schmitt, A. L.; Guzei, I. A.; Jin, S. *J. Am. Chem. Soc.* **2008**, *130*, 16086–16094.

(68) Pokhrel, A.; Degregorio, Z. P.; Higgins, J. M.; Girard, S. N.; Jin, S. *Chem. Mater.* **2013**, *25*, 632–638.

(69) De Ridder, R.; Amelinckx, S. *Mater. Res. Bull.* **1971**, *6*, 1223–1234.

(70) Ye, H. Q.; Amelinckx, S. *J. Solid State Chem.* **1986**, *61*, 8–39.

(71) Gottlieb, U.; Sulpice, A.; Lambert-Andron, B.; Laborde, O. *J. Alloys Compd.* **2003**, *361*, 13–18.

(72) Kajitani, T.; Yubuta, K.; Shishido, T.; Okada, S. *J. Electron. Mater.* **2010**, *39*, 1482–1487.

(73) Schwomma, O.; Preisinger, A.; Nowotny, H.; Wittmann, A. *Monatsh. Chem.* **1964**, *95*, 1527–1537.

(74) Knott, H. W.; Mueller, M. H.; Heaton, L. *Acta Crystallogr.* **1967**, *23*, 549–555.

(75) Flieher, G.; Völlenkle, H.; Nowotny, H. *Monatsh. Chem.* **1967**, *98*, 2173–2179.

(76) Zwilling, G.; Nowotny, H. *Monatsh. Chem.* **1973**, *104*, 668–675.

(77) Okada, S.; Shishido, T.; Ishizawa, Y.; Ogawa, M.; Kudou, K.; Fukuda, T.; Lundström, T. *J. Alloys Compd.* **2001**, *317*, 315–319.

(78) Okada, S.; Shishido, T.; Ogawa, M.; Matsukawa, F.; Ishizawa, Y.; Nakajima, K.; Fukuda, T.; Lundström, T. *J. Cryst. Growth* **2001**, *229*, 532–536.

(79) Miyazaki, Y.; Kikuchi, Y. *Thermoelectr. Nanomater. Mater. Des. Appl.* **2013**, *182*, 141.

(80) Karpinskii, O. G.; Evseev, B. A. In *Chemical Bonds in Solids*; Springer, **1995**, 3–7.

(81) Miyazaki, Y.; Igarashi, D.; Hayashi, K.; Kajitani, T.; Yubuta, K. *Phys. Rev. B* **2008**, *78*, 214104.

(82) Nowotny, H. In *The Chemistry of Extended Defects in Non-Metallic Solids*; Eyring, L., O'Keeffe, M., Eds.; North Holland, Amsterdam, **1970**, 223.

(83) Jeitschko, W. *Acta Crystallogr. B* **1977**, *33*, 2347–2348.

(84) Miyazaki, Y. In *Neutron Diffraction*; Khidirov, I., Ed.; INTECH Open Access Publisher, **2012**, 231–242.

(85) Fredrickson, D. C.; Lee, S.; Hoffmann, R. *Inorg. Chem.* **2004**, *43*,, 6159–6167.

(86) Imai, Y.; Watanabe, A. *Intermet.* **2005**, *13*,, 233–241.

(87) Allam, A.; Boulet, P.; Record, M.-C. *J. Alloys Compd.* **2014**, *584*, 279–288.

(88) Bost, M.; Mahan, J. E. *J. Electron. Mater.* **1987**, *16*, 389–395.

(89) Kawasumi, I.; Sakata, M.; Nishida, I.; Masumoto, K. *J. Mater. Sci.* **1981**, *16*, 355–366.

(90) Nishida, I. *J. Mater. Sci.* **1972**, *7*, 435–440.

(91) Lange, H.; Henrion, W.; Fenske, F.; Zettler, T.; Schumann, J.; Teichert, S. *Phys. status solidi* **1996**, *194*, 231–240.

(92) Rebien, M.; Henrion, W.; Angermann, H.; Teichert, S. *Appl. Phys. Lett.* **2002**, *81*, 649–651.

(93) Krontiras, C.; Promoni, K.; Roilos, M. *J. Phys. D. Appl. Phys.* **1988**, *21*, 509.

(94) Migas, D. B.; Shaposhnikov, V. L.; Filonov, A. B.; Borisenko, V. E.; Dorozhkin, N. N. *Phys. Rev. B* **2008**, *77*, 75205.

(95) Zhou, A. J.; Zhao, X. B.; Zhu, T. J.; Dasgupta, T.; Stiewe, C.; Hassdorf, R.; Müller, E. *Intermet.* **2010**, *18*, 2051–2056.

(96) Zhou, A. J.; Zhao, X. B.; Zhu, T. J.; Müller, E.; Stiewe, C.; Hassdorf, R. In *Proc 6th European Conference on Thermoelectrics*; **2008**.

(97) Zhou, A.; Zhu, T.; Zhao, X.; Mueller, E. *J. Mater. Res.* **2011**, *26*, 1900–1906.

(98) Allam, A.; Nunes, C. A.; Zalesak, J.; Record, M.-C. *J. Alloys Compd.* **2012**, *512*, 278–281.

(99) Zhou, A. J.; Zhu, T. J.; Zhao, X. B.; Yang, S. H.; Dasgupta, T.; Stiewe, C.; Hassdorf, R.; Mueller, E. *J. Electron. Mater.* **2010**, *39*, 2002–2007.

(100) Chen, X.; Girard, S. N.; Meng, F.; Lara-Curzio, E.; Jin, S.; Goodenough, J. B.; Zhou, J.; Shi, L. *Adv. Energy Mater.* **2014**, *4*, 1400452.

(101) Allam, A.; Boulet, P.; Nunes, C. A.; Record, M.-C. *Metall. Mater. Trans. A* **2013**, *44*, 1645–1650.

(102) Kikuchi, Y.; Nakajo, T.; Hayashi, K.; Miyazaki, Y. *J. Alloys Compd.* **2014**, *616*, 263–267.

(103) Zamanipour, Z.; Shi, X.; Mozafari, M.; Krasinski, J. S.; Tayebi, L.; Vashaee, D. *Ceram. Int.* **2013**, *39*, 2353–2358.

(104) Aoyama, I.; Kaibe, H.; Sano, S.; Solomkin, F. Y.; Eremin, I. S.; Fedorov, M. I.; Samunin, A. Y.; Vedernikov, M. V; Yamamura, Y.; Tsuji, T. In *Thermoelectrics, 2002. Proceedings ICT'02. Twenty-First International Conference on*; IEEE, **2002**, 90–93.

(105) Suvorova, E. I.; Klechkovskaya, V. V. *Crystallogr. Reports* **2013**, *58*, 854–861.

(106) Kojima, T.; Nishida, I.; Sakata, T. *J. Cryst. Growth* **1979**, *47*, 589–592.

(107) Levinson, L. M. *J. Solid State Chem.* **1973**, *6*, 126–135.

(108) Aoyama, I.; Fedorov, M. I.; Zaitsev, V. K.; Solomkin, F. Y.; Eremin, I. S.; Samunin, A. Y.; Mukoujima, M.; Sano, S.; Tsuji, T. *Jpn. J. Appl. Phys.* **2005**, *44*, 8562.

(109) Ivanova, L. D.; Baikov, A. A. *J. Thermoelectr.* **2009**, *3*, 60–66.

(110) Kawasumi, I.; Sakata, M.; Nishida, I.; Masumoto, K. *J. Cryst. Growth* **1980**, *49*, 651–658.

(111) Liu, G.; Lu, Q.; Zhang, X.; Zhang, J.; Shi, Y. *J. Electron. Mater.* **2012**, *41*, 1450–1455.

(112) Aoyama, I.; Kaibe, H.; Rauscher, L.; Kanda, T.; Mukoujima, M.; Sano, S.; Tsuji, T. *Jpn. J. Appl. Phys.* **2005**, *44*, 4275.

(113) Zaitsev, V. K. In *CRC Handbook of Thermoelectrics*; Rowe, D. M., Ed.; CRC Press, New York, **1995**, 299.

(114) Zhou, A. J.; Zhao, X. B.; Zhu, T. J.; Yang, S. H.; Dasgupta, T.; Stiewe, C.; Hassdorf, R.; Müller, E. *Mater. Chem. Phys.* **2010**, *124*, 1001–1005.

(115) Zhou, A. J.; Zhao, X. B.; Zhu, T. J.; Cao, Y. Q.; Stiewe, C.; Hassdorf, R.; Müller, E. *J. Electron. Mater.* **2009**, *38*, 1072–1077.

(116) Shi, X.; Zamanipour, Z.; Dehkordi, A. M.; Ede, K. F.; Krasinski, J. S.; Vashaee, D. In *Green Technologies Conference, 2012 IEEE*; IEEE, **2012**, 1–3.

(117) Shi, X.; Zamanipour, Z.; Ede, K. F.; Krasinski, J. S.; Vashaee, D. In *Green Technologies Conference, 2012 IEEE*; IEEE, **2012**, 1–3.

(118) Luo, W.; Li, H.; Yan, Y.; Lin, Z.; Tang, X.; Zhang, Q.; Uher, C. *Intermet.* **2011**, *19*, 404–408.

(119) Yamada, T.; Miyazaki, Y.; Yamane, H. *Thin Solid Films* **2011**, *519*, 8524–8527.

(120) Sadia, Y.; Gelbstein, Y. *J. Electron. Mater.* **2012**, *41*, 1504–1508.

(121) Famengo, A.; Battiston, S.; Saleemi, M.; Boldrini, S.; Fiameni, S.; Agresti, F.; Toprak, M. S.; Barison, S.; Fabrizio, M. *J. Electron. Mater.* **2013**, *42*, 2020–2024.

(122) Groβ, E.; Riffel, M.; Stöhrer, U. *J. Mater. Res.* **1995**, *10*, 34–40.

(123) Umemoto, M.; Liu, Z. G.; Omatsuzawa, R.; Tsuchiya, K. *J. Metastable Nanocrystalline Mater.* **2000**, *8*, 918–923.

(124) Miyazaki, Y.; Saito, Y.; Hayashi, K.; Yubuta, K.; Kajitani, T. *Jpn. J. Appl. Phys.* **2011**, *50*, 5804.

(125) He, Y. J.; Hou, Q. R.; Wang, Z. M.; Chen, Y. B. In *Materials for Renewable Energy & Environment (ICMREE), 2011 International Conference on*; IEEE, **2011**, *2*, 1343–1345.

(126) Sadia, Y.; Elegrably, M.; Ben-Nun, O.; Marciano, Y.; Gelbstein, Y. *J. Nanomater.* **2013**, *2013*, 4.

(127) Shin, D.-K.; Ur, S.-C.; Jang, K.-W.; Kim, I.-H. *J. Electron. Mater.* **2014**, *43*, 2104–2108.

(128) Shin, D.-K.; You, S.-W.; Kim, I.-H. *J. Korean Phys. Soc.* **2014**, *65*, 1499–1502.

(129) Luo, W.; Li, H.; Fu, F.; Hao, W.; Tang, X. *J. Electron. Mater.* **2011**, *40*, 1233–1237.

(130) An, T.-H.; Choi, S.-M.; Seo, W.-S.; Park, C.; Kim, I.-H.; Kim, S.-U. *J. Electron. Mater.* **2013**, *42*, 2269–2273.

(131) Shi, X.; Shi, X.; Li, Y.; He, Y.; Chen, L.; Li, Q. *J. Appl. Phys.* **2014**, *116*, 245104.

(132) Itoh, T.; Yamada, M. *J. Electron. Mater.* **2009**, *38*, 925–929.

(133) Shin, D.-K.; Jang, K.-W.; Ur, S.-C.; Kim, I.-H. *J. Electron. Mater.* **2013**, *42*, 1756–1761.

(134) An, T.-H.; Choi, S.-M.; Seo, W.-S.; Park, C.; Kim, I.-H.; Kim, S.-U. *Jpn. J. Appl. Phys.* **2013**, *52*, 10MC11.

(135) Sadia, Y.; Madar, N.; Kaler, I.; Gelbstein, Y. *J. Electron. Mater.* **2014**, *44*, 1637–1643.

(136) Lee, Y.-G.; Choi, M.-K.; Kim, I.-H.; Ur, S.-C. *J. Ceram. Process. Res.* **2012**, *13*, 816–819.

(137) Lin, L. W.-H. L. H.; Xin-Feng, Z.-B. T. *Acta Phys. Sin.* **2010**, *12*, 68.

(138) Kikuchi, Y.; Miyazaki, Y.; Saito, Y.; Hayashi, K.; Yubuta, K.; Kajitani, T. *Jpn. J. Appl. Phys.* **2012**, *51*, 85801.

(139) Sadia, Y.; Dinnerman, L.; Gelbstein, Y. *J. Electron. Mater.* **2013**, *42*, 1926–1931.

(140) Girard, S. N.; Chen, X.; Meng, F.; Pokhrel, A.; Zhou, J.; Shi, L.; Jin, S. *Chem. Mater.* **2014**, *26*, 5097–5104.

(141) Ivanova, L. D. *Inorg. Mater.* **2011**, *47*, 965–970.

(142) Zhou, A. J.; Zhu, T. J.; Ni, H. L.; Zhang, Q.; Zhao, X. B. *J. Alloys Compd.* **2008**, *455*, 255–258.

(143) Ponnambalam, V.; Morelli, D. T. *J. Electron. Mater.* **2012**, *41*, 1389–1394.

(144) Norouzzadeh, P.; Zamanipour, Z.; Krasinski, J. S.; Vashaee, D. *J. Appl. Phys.* **2012**, *112*, 124308.

(145) Saleemi, M.; Famengo, a.; Fiameni, S.; Boldrini, S.; Battiston, S.; Johnsson, M.; Muhammed, M.; Toprak, M. S. *J. Alloys Compd.* **2015**, *619*, 31–37.

(146) Itoh, T.; Ono, N. In *MRS Proceedings*; Cambridge Univ Press, **2013**, *1490*, 127–132.

(147) Ponnambalam, V.; Morelli, D. T.; Bhattacharya, S.; Tritt, T. M. *J. Alloys Compd.* **2013**, *580*, 598–603.

(148) Okamoto, N. L.; Koyama, T.; Kishida, K.; Tanaka, K.; Inui, H. *Acta Mater.* **2009**, *57*, 5036–5045.

(149) Stohrer, U. *Meas. Sci. Technol.* **1994**, *5*, 440.

(150) Chen, X.; Weathers, A.; Salta, D.; Zhang, L.; Zhou, J.; Goodenough, J. B.; Shi, L. *J. Appl. Phys.* **2013**, *114*, 173705.

(151) Bernard-Granger, G.; Soulier, M.; Ihou-Mouko, H.; Navone, C.; Boidot, M.; Leforestier, J.; Simon, J. *J. Alloys Compd.* **2015**, *618*, 403–412.

(152) Barczak, S. A.; Downie, R. A.; Popuri, S. R.; Decourt, R.; Pollet, M.; Bos, J. W. G. *J. Solid State Chem.* **2015**, *227*, 55–59.

(153) Miyazaki, Y.; Saito, Y.; Hayashi, K.; Yubuta, K.; Kajitani, T. In *Advances in Science and Technology*; Trans. Tech. Publ., **2011**, *74*, 22–25.

(154) Solomkin, F. Y.; Zaitsev, V. K.; Kartenko, N. F.; Kolosova, A. S.; Samunin, A. Y.; Isachenko, G. N. *Tech. Phys.* **2008**, *53*, 1636–1637.

(155) Udono, H.; Nakamori, K.; Takahashi, Y.; Ujiie, Y.; Ohsugi, I. J.; Iida, T. *J. Electron. Mater.* **2011**, *40*, 1165–1170.

(156) Okada, S.; Kudou, K.; Shishido, T. *Pacific Sci. Rev.* **2009**, *11*, 22.

(157) Solomkin, F. Y.; Zaitsev, V. K.; Kartenko, N. F.; Kolosova, A. S.; Samunin, A. Y.; Isachenko, G. N. *Tech. Phys.* **2008**, *53*, 800–801.

(158) Kojima, T.; Nishida, I. *Jpn. J. Appl. Phys.* **1975**, *14*, 141.

(159) Shi, X.; Zamanipour, Z.; Krasinski, J. S.; Tree, A.; Vashaee, D. *J. Electron. Mater.* **2012**, *41*, 2331–2337.

(160) Solomkin, F. Y. *Tech. Phys.* **2000**, *45*, 1094–1095.

(161) Petrova, L. I.; Dudkin, L. D.; Khlomov, V. S.; Fedorov, M. I.; Zaitsev, V. K.; Solomkin, F. Y. *Tech. Phys.* **2000**, *45*, 641–643.

(162) Petrova, L. I.; Dudkin, L. D.; Fedorov, M. I.; Solomkin, F. Y.; Zaitsev, V. K.; Eremin, I. S. *Tech. Phys.* **2002**, *47*, 550–554.

(163) Kaibe, H.; Aoyama, I.; Sano, S. In *Presentation at XIII Int. Forum on Thermoelectricity*; **2009**.

(164) Kajitani, T.; Ueno, T.; Miyazaki, Y.; Hayashi, K.; Fujiwara, T.; Ihara, R.; Nakamura, T.; Takakura, M. *J. Electron. Mater.* **2014**, *43*, 1993–1999.

(165) Schubert, U.; Hüsing, N. In *Synthesis of inorganic materials*; John Wiley & Sons, **2012**, *5*.

(166) Pettit, F. S.; Randklev, E. H.; Felten, E. J. *J. Am. Ceram. Soc.* **1966**, *49*, 199–203.

(167) Suryanarayana, C. *Prog. Mater. Sci.* **2001**, *46*, 1–184.

(168) Benjamin, J. S. *Metall. Trans.* **1970**, *1*, 2943–2951.

(169) Schmidt, P.; Schmidt, M.; Binnewies, M.; Glaum, R. In *Advanced Topics on Crystal Growth*; INTECH Open Access Publisher, **2013**, 227–305.

(170) Binnewies, M.; Glaum, R.; Schmidt, M.; Schmidt, P. *Zeitschrift für Anorg. und Allg. Chemie* **2013**, *639*, 219–229.

(171) Guillon, O.; Gonzalez-Julian, J.; Dargatz, B.; Kessel, T.; Schierning, G.; Räthel, J.; Herrmann, M. *Adv. Eng. Mater.* **2014**, *16*, 830–849.

(172) Suárez, M.; Fernández, A.; Kessel, H. U.; Hennicke, J.; Menéndez, J. L.; Kirchner, R.; Torrecillas, R.; Kessel, T. In *Sintering Applications*; INTECH Open Access Publisher, **2013**, 319–342.

(173) Ladd, M. F. C.; Palmer, R. A. In *Structure determination by X-ray crystallography: analysis by x-rays and neutrons*; New York : Springer, **2013**, 111–159.

(174) Will, G. In *Powder diffraction: The Rietveld method and the two stage method to determine and refine crystal structures from powder diffraction data*; Springer Science & Business Media, **2006**, 1–39.

(175) Pecharsky, V. K.; Zavalij, P. Y. *Fundamentals of powder diffraction and structural characterization of materials*; Springer, **2009**, *69*.

(176) Zhou, W.; Apkarian, R.; Wang, Z. L.; Joy, D. In *Scanning Microscopy for Nanotechnology*; Zhou, W., Wang, Z. L., Eds.; Springer, **2007**, 1–40.

(177) Tritt, T. M.; Weston, D. In *Thermal conductivity: theory, properties, and applications*; Tritt, T. M., Ed.; Springer Science & Business Media, **2004**, 197.

(178) Chu, F. I.; Taylor, R. E.; Donaldson, A. B. *J. Appl. Phys.* **1980**, *51*, 336–341.

(179) Standard, A. *ASTM, West Conshohocken, PA* **2001**, 458–469.

(180) Parker, W. J.; Jenkins, R. J.; Butler, C. P.; Abbott, G. L. *J. Appl. Phys.* **1961**, *32*, 1679–1684.

(181) Cowan, R. D. *J. Appl. Phys.* **1963**, *34*, 926–927.

(182) Cape, J.; Lehman, G. W. *J. Appl. Phys.* **1963**, *34*, 1909–1913.

(183) Clark III, L. M.; Taylor, R. E. *J. Appl. Phys.* **1975**, *46*, 714–719.

(184) Min, S.; Blumm, J.; Lindemann, A. *Thermochim. Acta* **2007**, *455*, 46–49.

(185) Beer, A. C. *Solid. State. Electron.* **1966**, *9*, 339–351.

(186) Taylor, J. R. *An Introduction to Error Analysis: The Study of Uncertainties in Physical Measurements*; **1982**.

(187) Young, H. D. *Statistical treatment of experimental data*; McGraw-Hill New York, **1962**.

(188) Yang, R.; Chen, G.; Dresselhaus, M. S. *Phys. Rev. B* **2005**, *72*, 125418.

(189) Corral, E. L.; Wang, H.; Garay, J.; Munir, Z.; Barrera, E. V. *J. Eur. Ceram. Soc.* **2011**, *31*, 391–400.

(190) Dou, Y. C.; Qin, X. Y.; Li, D.; Li, L. L.; Zou, T. H.; Wang, Q. Q. *J. Appl. Phys.* **2013**, *114*, 44906.

(191) Dong, J.; Liu, W.; Li, H.; Su, X.; Tang, X.; Uher, C. *J. Mater. Chem. A* **2013**, *1*, 12503–12511.

(192) Yadav, B. C.; Kumar, R. *Int. J. Nanotechnol. Appl.* **2008**, *2*, 15–24.

(193) De Volder, M. F. L.; Tawfick, S. H.; Baughman, R. H.; Hart, A. J. *Science* **2013**, *339*, 535–539.

(194) Savary, E.; Gascoin, F.; Marinel, S. *Dalton Trans.* **2010**, *39*, 11074–11080.

(195) Ioannou, M.; Chrissafis, K.; Pavlidou, E.; Gascoin, F.; Kyratsi, T. *J. Solid State Chem.* **2013**, *197*, 172–180.

(196) Savary, E.; Gascoin, F.; Marinel, S.; Heuguet, R. *Powder Technol.* **2012**, *228*, 295–300.

(197) Hou, Q. R.; Zhao, W.; Zhang, H. Y.; Chen, Y. B.; He, Y. J. *Phys. status solidi* **2006**, *203*, 2468–2477.

(198) Ponnambalam, V.; Morelli, D. T.; Bhattacharya, S.; Tritt, T. M. *J. Alloys Compd.* **2013**, *580*, 598–603.

(199) Zhou, A. J.; Zhu, T. J.; Ni, H. L.; Zhang, Q.; Zhao, X. B. *J. Alloys Compd.* **2008**, *455*, 255–258.

(200) Truong, D. Y. N.; Kleinke, H.; Gascoin, F. *Dalton Trans.* **2014**, *43*, 15092–15097.

(201) Shenashen, M. A.; El-Safty, S. A.; Elshehy, E. A. *Part. Part. Syst. Charact.* **2014**, *31*, 293–316.

(202) Zhou, X.; Wang, G.; Zhang, L.; Chi, H.; Su, X.; Sakamoto, J.; Uher, C. *J. Mater. Chem.* **2012**, *22*, 2958–2964.

(203) Zhang, Q.; Ai, X.; Wang, L.; Chang, Y.; Luo, W.; Jiang, W.; Chen, L. *Adv. Funct. Mater.* **2015**, *25*, 966–976.

(204) Wang, W.; Sun, S.; Gu, S.; Shen, H.; Zhang, Q.; Zhu, J.; Wang, L.; Jiang, W. *RSC Adv.* **2014**, *4*, 26810–26816.

(205) Rodriguez-Carvajal, J. In *satellite meeting on powder diffraction of the XV congress of the IUCr*; Toulouse, France, **1990**, *127*.

(206) Vining, C. B. In *CRC Handbook of Thermoelectrics*; Rowe, D. M., Ed.; CRC Press, New York, **1995**, 277.

(207) Gilman, P. S.; Benjamin, J. S. *Annu. Rev. Mater. Sci.* **1983**, *13*, 279–300.

(208) Chen, X.; Weathers, A.; Moore, A.; Zhou, J.; Shi, L. *J. Electron. Mater.* **2012**, *41*, 1564–1572.

(209) Kaga, H.; Kinemuchi, Y.; Watari, K.; Tanaka, S.; Makiya, A.; Kato, Z.; Uematsu, K. *J. Mater. Res.* **2007**, *22*, 2917–2923.

(210) Wang, Z.; Wu, Y.; He, Y. *Int. J. Mod. Phys. B* **2004**, *18*, 87–93.

(211) Narducci, D.; Selezneva, E.; Cerofolini, G.; Frabboni, S.; Ottaviani, G. *J. Solid State Chem.* **2012**, *193*, 19–25.

(212) Li, W.; Ishikawa, D.; Hu, J.; Tatsuoka, H. *J. Electron. Mater.* **2014**, *43*, 1487–1491.

(213) Kang, S.; Brewer, G.; Sapkota, K. R.; Pegg, I. L.; Philip, J. *IEEE Trans. Nanotechnol.* **2012**, *11*, 437.

(214) Naito, M.; Nakanishi, R.; Machida, N.; Shigematsu, T.; Ishimaru, M.; Valdez, J. A.; Sickafus, K. E. *Nucl. Instruments Methods Phys. Res. Sect. B Beam Interact. with Mater. Atoms* **2012**, *272*, 446–449.

(215) Gao, Y.; Shao, G. S.; Li, Q.; Xu, Y. M.; Wong, S. P.; Zhou, M. Y.; Lourenco, M. A.; Homewood, K. P. *Jpn. J. Appl. Phys.* **2007**, *46*, 5777.

(216) Zou, Z.-Q.; Li, W.-C.; Liang, J.-M.; Wang, D. *Acta Mater.* **2011**, *59*, 7473–7479.

(217) Liu, H.; She, G.; Huang, X.; Qi, X.; Mu, L.; Meng, X.; Shi, W. *J. Phys. Chem. C* **2013**, *117*, 2377–2381.

(218) Okamoto, H. *J. Phase Equilibria* **1991**, *12*, 505–507.

(219) Chakraborti, N.; Lukas, H. L. *Calphad* **1989**, *13*, 293–300.

(220) Truong, D. Y. N.; Kleinke, H.; Gascoin, F. *Intermet.* **2015**, *66*, 127–132.

(221) Allam, A.; Boulet, P.; Record, M.-C. *Phys. Procedia* **2014**, *55*, 24–29.

(222) Truong, D. Y. N.; Berthebaud, D.; Gascoin, F.; Kleinke, H. *J. Electron. Mater.* **2015**, *44*, 3603–3611.